(4)

AFGL-TR-87-0246

BOUNDARY LAYER PARAMETERIZATION FOR A GLOBAL SPECTRAL MODEL

L. Mahrt
H.-L. Pan
P. Ruscher
C.-T. Chu

Oregon State University
Department of Atmospheric Sciences
Corvallis, Oregon 97331

Final Report
17 August 1984 - 16 July 1987

17 August 1987

AIR FORCE GEOPHYSICS LABORATORY
AIR FORCE SYSTEMS COMMAND
UNITED STATES AIR FORCE
HANSCOM AIR FORCE BASE, MASSACHUSETTS 01731

This technical report has been reviewed and is approved for publication.

Kenneth E. Mitchell
KENNETH E. MITCHELL
Contract Manager

Donald A. Chisholm
DONALD A. CHISHOLM, Chief
Atmospheric Prediction Branch

FOR THE COMMANDER

Robert A. McClatchey
ROBERT A. McCLATCHEY, Director
Atmospheric Sciences Division

This document has been reviewed by the ESD Public Affairs Office (PA) and is releasable to the National Technical Information Service (NTIS).

Qualified requestors may obtain additional copies from the Defense Technical Information Center. All others should apply to the National Technical Information Service.

If your address has changed, or if you wish to be removed from the mailing list, or if the addressee is no longer employed by your organization, please notify AFGL/DAA, Hanscom AFB, MA 01731-5000. This will assist us in maintaining a current mailing list.

Do not return copies of this report unless contractual obligations or notices on a specific document requires that it be returned.

REPORT DOCUMENTATION PAGE

1a. REPORT SECURITY CLASSIFICATION: Unclassified	1b. RESTRICTIVE MARKINGS:
2a. SECURITY CLASSIFICATION AUTHORITY:	3. DISTRIBUTION/AVAILABILITY OF REPORT: Approved for public release; distribution unlimited
2b. DECLASSIFICATION/DOWNGRADING SCHEDULE:	
4. PERFORMING ORGANIZATION REPORT NUMBER(S):	5. MONITORING ORGANIZATION REPORT NUMBER(S): AFGL-TR-87-0246
6a. NAME OF PERFORMING ORGANIZATION: Oregon State University Dept. Atmospheric Sciences; 6b. OFFICE SYMBOL (If applicable): AtS OSU	7a. NAME OF MONITORING ORGANIZATION: Air Force Geophysics Laboratory
6c. ADDRESS (City, State and ZIP Code): Corvallis, Oregon 97331	7b. ADDRESS (City, State and ZIP Code): Hanscom AFB Massachusetts 01731 Monitor/Kenneth Mitchell/LYP
8a. NAME OF FUNDING/SPONSORING ORGANIZATION; 8b. OFFICE SYMBOL (If applicable):	9. PROCUREMENT INSTRUMENT IDENTIFICATION NUMBER: F19628-84-K-0044
8c. ADDRESS (City, State and ZIP Code):	10. SOURCE OF FUNDING NOS.

PROGRAM ELEMENT NO.	PROJECT NO.	TASK NO.	WORK UNIT NO.
61102F	2310	G7	AI

11. TITLE (Include Security Classification): Boundary Layer Parameterization for a Global Spectral Model

12. PERSONAL AUTHOR(S): Mahrt, Larry J.; Pan, Hua-Lu; Ruscher, Paul H.; Chu, C.-T.

13a. TYPE OF REPORT	13b. TIME COVERED	14. DATE OF REPORT (Yr., Mo., Day)	15. PAGE COUNT
Final	FROM 17 Aug84 TO 16Jul87	1987 August 17	188

16. SUPPLEMENTARY NOTATION:

17. COSATI CODES			18. SUBJECT TERMS (Continue on reverse if necessary and identify by block number)
FIELD	GROUP	SUB. GR.	Atmospheric boundary layer, surface energy balance, soil model, stable layer parameterization, surface fluxes.
04	02		

19. ABSTRACT (Continue on reverse if necessary and identify by block number)

This report describes work conducted under contract number F19628-84-K-0044 from the Air Force Geophysics Laboratory. Much of the work has concentrated on interactions between the soil model and the model of the atmospheric boundary layer and the behavior of the boundary-layer package within the Air Force Global Spectral Model. Such studies have underscored the importance of the formulation of surface properties and transport within the underlying soil.

Work during the contract period also focussed on elimination of several inadequacies of boundary-layer modelling. The inclusion of the statistical impact of subgrid variations of surface properties leads to a surface exchange coefficient which varies more smoothly with stability and does not decrease as rapidly with very stable conditions. Such modifications reduce the nocturnal cooling which is usually overestimated in boundary-layer models. Other improvements of the boundary-layer model in stable conditions have resulted from increasing the critical Richardson number in the boundary-layer depth formulation and adopting the Kondo formulation for the eddy diffusivity.

The development of a formulation for boundary-layer cumulus has allowed inclusion of cloud-induced drying. Although this formulation leads to significant improvement of the boundary-layer predictions in cloudy situations, the general problem is far from solved.

20. DISTRIBUTION/AVAILABILITY OF ABSTRACT	21. ABSTRACT SECURITY CLASSIFICATION
UNCLASSIFIED/UNLIMITED ☐ SAME AS RPT. ☒ DTIC USERS ☐	Unclassified

22a. NAME OF RESPONSIBLE INDIVIDUAL	22b. TELEPHONE NUMBER (Include Area Code)	22c. OFFICE SYMBOL
Kenneth E. Mitchell	(617)377-2954	AFGL/LYP

ACKNOWLEDGEMENTS

This work was primarily carried out by the two principal scientists, Larry Mahrt and Hua-Lu Pan. Paul Ruscher studied the improvement of the parameterization of the stable boundary layer and included the work in his Ph.D. dissertation. The shallow convection parameterization was investigated by Cheng-Tsong Chu and resulted in a Masters thesis. Kyozo Ueyoshi provided help in the formulation of the grid-box averaging effects. Wayne Gibson provided the bulk of the programming support. James Deardorff of the Department of Atmospheric Sciences and Stuart Childs of the Department of Soil Science made helpful comments on several of the manuscripts. Naomi Weidner and Michael Ek are acknowledged for their assistance in putting this report into final form.

This research was sponsored by the Air Force Geophysics Laboratory, Hanscom Air Force Base, Massachusetts, under contract No. F19628-84-K-0044.

TABLE OF CONTENTS

TABLE OF CONTENTS (continued)

I. INTRODUCTION

The development of numerical models is guided by two conflicting goals. The first goal is to include the most realistic physics for the level of complexity allowed by computer requirements and other practical considerations. The second goal is to construct a model in which the different physical elements of the model are operationally compatible and lead to reasonable results. In an attempt to achieve the second goal, it is sometimes necessary to compromise part of the first goal.

The construction of the boundary-layer package at Oregon State University for the Air Force Global Spectral Model of the Air Force Geophysics Laboratory has been primarily occupied with development of improved physical and dynamical modelling (first goal) with only recent effort directed towards overall model compatibility and performance (second goal). The previous contract period (Mahrt *et al.*, 1984) was devoted almost entirely to formulation of individual components of the model with an emphasis on physical consistency. [Note: all citations in Chapter 1 appear in the reference list following Chapter 2.] This led to a rather original but simple treatment of the vegetative canopy (Mahrt *et al.*, 1984). An original two-layer model of soil hydrology was developed (Mahrt and Pan, 1984) which contained physics comparable to the existing models with many levels whereas previous two-layer models were purely empirical. This development required careful partitioning of the two layers to control truncation errors with respect to natural time scales and required reconsideration of the soil surface boundary conditions.

A model of the atmospheric boundary layer was developed (Troen and Mahrt, 1986) which was sufficiently simple yet allowed growth of the boundary layer due to both surface heating and wind shear. The boundary-layer depth formulation seems to be rather robust and has been recently tested and adopted by the Canadian Atmospheric and Environmental Service (AES) and the Dutch Royal Meteorological Institute (KNMI).

Work under the present contract has concentrated on improvement of specific aspects of the model such as the implied grid-area averaging of the surface fluxes, modeling transport induced by boundary-layer clouds, the

special circumstances of transport in the very stable boundary layer, fluxes over snow covered surfaces and soil heat transport. The present effort has also devoted considerable work to the interaction of the boundary-layer model and the soil hydrology model.

The basic equations for the boundary-layer package are summarized in Chapter II while the basic model development is motivated in Troen and Mahrt (1986). Detailed examination of the interaction between the different submodels of the boundary-layer package has concentrated on coupling between boundary-layer development and heat and moisture transport in the soil model. Boundary-layer development responding to heat transport from the surface has received considerable attention in the literature. However the large impact of surface evaporation and soil moisture transport on boundary-layer development has unjustifiably received less attention. The importance of coupling between soil moisture transport and evolution of the atmospheric boundary layer in our model is illustrated in Chapter III. In fact the basic nature of the diurnal variation of the boundary layer changes completely between changes of the three main stages of soil drying. The timing of the onset of various stages of drying depends on soil type as well as the potential evaporation imposed by the atmospheric boundary layer.

The boundary-layer package, mainly without the improvements of Chapters IV-VI, has been studied in global numerical runs within the Air Force Global Spectral Model. These numerical experiments are reported elsewhere (Yang *et al.*, 1988). Improved formulation of the surface exchange coefficient is developed in Chapter IV of this report. The modified exchange coefficient includes the statistical influence of subgrid scale variations of surface properties. The associated modifications leads to an exchange coefficient which varies more smoothly with stability at the transition between unstable and stable conditions and decreases more slowly with increasing stability in the stable case. Implementation of the modified exchange coefficient into the one-dimensional boundary-layer package led to improved performance especially with very stable conditions. However the improvements were modest.

Improved physical formulation of the nocturnal boundary layer is motivated, implemented and tested in Chapter V of this report. A common

deficiency of boundary-layer models is strong overestimation of surface cooling with very stable conditions. *Ad hoc* corrections are often made which avoid the real problem; namely, that standard boundary-layer formulations erroneously "kill" the turbulent mixing too fast in very stable conditions This inadequacy is corrected here by using a larger critical Richardson number, using Kondo's formulation for the eddy diffusivity and applying the improved surface exchange coefficient discussed in Chapter IV.

The work summarized in Chapter VI develops a formulation for transport by shallow boundary-layer cumulus. This transport exerts a major drying effect on the boundary layer. Failure to include the influence of cumulus-induced drying in boundary-layer models will lead to unrealistic moisture buildup. Comparisons are made between the formulation developed in Chapter VI and the state of the art model of the European Centre for Medium-Range Weather Forecasts (ECMWF) using actual data. These comparisons suggest that the present development can lead to improved modelled transport within boundary layers containing shallow cumulus. However the problem involves interaction between the cloud-induced mixing and other aspects of the boundary-layer model, and, the problem may vary considerably between different types of boundary-layer clouds. The present formulation requires more work and any existing evaluation of the model must be considered tentative.

II. THE SOIL AND BOUNDARY LAYER MODEL

1. Introduction

In the present contract, a complicated set of equations are utilized to model the atmosphere, the soil, and the vegetated surface. While the individual model components have been examined previously (Troen and Mahrt, 1986; Mahrt and Pan, 1984), the study of the interaction among the components is an important goal in the present contract. In addition, parameterizations of shallow cloud convection and snow-cover are constructed based on the existing model equations. We first present the entire set of equations and then present results of the current contract.

The equation set will be presented in Section 2 and a brief description of the computational procedure in Section 3. More detailed explanation of the equations can be found in the individual chapters of a previous report (Mahrt et al., 1984). The equations for the atmospheric boundary layer are given first because the effect of the turbulent mixing is the goal of the entire effort of the contract. In order to close the system and calculate the forcing of the atmospheric variables due to turbulent mixing, boundary conditions near the earth's surface must be provided. To obtain these conditions, an atmospheric surface layer parameterization will be used. The exchange of sensible and latent heat flux between the surface layer and the underlying surface can only be obtained with a knowledge of the soil and ocean surface conditions. Equations for the atmospheric surface layer, the soil hydrology, and the soil thermodynamics used in the model are presented following the boundary layer equations. The surface energy balance is used to incorporate radiative heating effects into both the boundary layer and the soil layer and is presented last. From the computational point of view, the order is actually reversed as we must prescribe the external driving force first. This will become evident in Section 3.

2. The Model Equations

This Section is divided into four subsections, each describing individual aspects of the planetary boundary layer (PBL) model and soil model. Turbulent mixing within the PBL is described in §2a, the surface layer model of the atmosphere is given in §2b, the soil model is found in §2c, and the surface energy balance calculation is discussed in §2d.

a. Boundary layer model

The PBL model is as discussed by Troen and Mahrt (1986). The model forecasts the tendencies due to turbulent mixing of the potential temperature (θ), specific humidity (q), and horizontal components of the wind. The set of prognostic equations is

$$\frac{\partial \mathbf{V}}{\partial t} = \frac{\partial}{\partial z}\left(K_m \frac{\partial \mathbf{V}}{\partial z}\right) \qquad (1)$$

$$\frac{\partial \theta}{\partial t} = \frac{\partial}{\partial z}\left(K_h \left(\frac{\partial \theta}{\partial z} - \gamma_\theta\right)\right) \qquad (2)$$

$$\frac{\partial q}{\partial t} = \frac{\partial}{\partial z}\left(K_h \left(\frac{\partial q}{\partial z} - \gamma_q\right)\right) \qquad (3)$$

Here, only the vertical diffusion terms due to boundary layer turbulent mixing are kept in the equation to simplify the presentation. Details of the complete equations may be found in Troen and Mahrt (1986).

The counter-gradient correction (γ) is included in both (2) and (3) following Troen and Mahrt (1986), and is parameterized as follows:

$$\gamma_\theta = \begin{cases} 0 & , \text{ stable} \\ C\dfrac{\overline{(w'\theta')_o}}{w_s h} & , \text{ unstable} \end{cases} \qquad (4)$$

$$\gamma_q = \begin{cases} 0 & , \text{ stable} \\ C\dfrac{\overline{(w'q')_o}}{w_s h} & , \text{ unstable} \end{cases} \qquad (5)$$

The counter-gradient corrections are evaluated in terms of the surface fluxes of potential temperature and specific humidity, the boundary-layer depth (h), the velocity scale (w_s) of the boundary layer defined as

$$w_s = u_* \, \phi_m^{-1}\left(\frac{z_s}{L}\right) \qquad (6)$$

and a constant C, set to 6.5, as in Troen and Mahrt (1986). In (6), u* is the surface friction velocity and L is the Monin-Obukhov length. ϕ_m is a profile function which is specified in (12) below.

The coefficient of diffusivity for momentum (K_m) is

$$K_m = w_s \, h \, k \, \frac{z}{h}\left(1 - \frac{z}{h}\right)^p \qquad (7)$$

The eddy diffusivity for heat is related to the eddy diffusivity for momentum in terms of the turbulent Prandtl number

$$K_h = K_m P_r^{-1} \qquad (8)$$

where

$$P_r = \left[\frac{\phi_h\left(\frac{z}{L}\right)}{\phi_m\left(\frac{z}{L}\right)} + Ck\frac{z}{h} \right]_{z=z_s} \qquad (9)$$

In other terms, the Prandtl number is assumed to be a constant and is determined as the value at the top of the surface layer (z_s) using surface layer similarity theory. As shown in Eq. 9, the counter-gradient term is also absorbed in the Prandtl number. The profile functions (ϕ_m, ϕ_h) have their normal definition and will be defined formally below. The resulting prediction equation for potential temperature and specific humidity will therefore not explicitly contain the counter-gradient term and is actually identical in form to Eq. 1 (Troen and Mahrt, 1986).

The boundary layer height is diagnosed as

$$h = \frac{Ri_{cr}\,\theta_{ov}|\mathbf{V}(h)|^2}{g\left(\theta_v(h) - \theta_o^*\right)} \qquad (10)$$

where Ri_{cr} is the critical Richardson number, θ_{ov} is a reference virtual

potential temperature, g is the gravitational acceleration, and $\theta_v(h)$ is the virtual potential temperature at level h. This approach to diagnosing the PBL height also requires the specification of a low level potential temperature (θ_{ov}^*). We define θ_{ov}^* in the following way:

$$\theta_{ov}^* = \begin{cases} \theta_{ov} & \text{, stable} \\ \theta_{ov} + C\,\dfrac{\overline{(w'\theta_v')}_o}{w_s} & \text{, unstable} \end{cases} \qquad (11)$$

When the boundary layer is unstable, the surface virtual potential temperature in (11) is enhanced by an amount that is proportional to the surface sensible heat flux. The constant of proportionality is C and is chosen as 6.5 as in Eqs. 4, 5, and 9.

The nondimensional profile functions for shear and thermal gradient are defined as follows:

$$\phi_m = \begin{cases} 1 + 4.7\,\dfrac{z}{L} & \text{, stable} \\ \left(1 - 7\,\dfrac{z}{L}\right)^{-1/3} & \text{, unstable} \end{cases} \qquad (12)$$

and

$$\phi_h = \begin{cases} .74 + 4.7\,\dfrac{z}{L} & \text{, stable} \\ .74\left(1 - 9\,\dfrac{z}{L}\right)^{-1/2} & \text{, unstable} \end{cases} \qquad (13)$$

These forms are taken from Businger *et al.* (1971) and are functions of the height coordinate (z) and the Monin-Obukhov length scale (L).

The following variables are calculated in the surface layer and will be described in the next section:

$$u_*,\ \overline{(w'\theta')}_o,\ \overline{(w'q')}_o,\ L$$

These are, respectively, the friction velocity, the surface flux of potential temperature, the surface flux of specific humidity, and the Monin-Obukhov length scale.

b. Surface layer model

The lowest model layer is parameterized as a constant flux surface layer. The surface fluxes are parameterized following Louis (1979), as follows:

$$u_*^2 = k^2\,|V_o|^2\,F\left(\frac{z}{z_o},\ Ri_B\right) \Big/ \left(\ln\frac{z}{z_o}\right)^2 \qquad (14)$$

$$\overline{(w'\theta')}_o = C_h\left(|V_o|, \frac{z}{z_o}, Ri_B\right)(\theta_s - \theta_o) \qquad (15)$$

$$\overline{(w'q')}_o = C_h\left(|V_o|, \frac{z}{z_o}, Ri_B\right)(q_s - q_o) \qquad (16)$$

In Eq. 14, u_* is the friction velocity, k is von Kármán's constant, the surface wind speed ($|V_o|$) is evaluated at the lowest model level and the roughness length (z_o) depends on the type of surface. The function (F) and the bulk Richardson number for the surface layer (Ri_B) are described below. In Eqs. 15 and 16, the exchange coefficient (C_h) is a function of the surface wind speed ($|V_o|$), the height of the first model level (z), the surface roughness length (z_o), and the bulk-Richardson number. The surface air potential temperature (θ_o) and specific humidity (q_o) are taken at the first model level while the surface potential temperature (θ_s) and specific humidity (q_s) are obtained from the surface energy balance. The surface potential temperature is related to the surface temperature, T_s, by $\theta_s = T_s(P_s/p_0)^{R/C_p}$, where p_0 is taken to be 1000 hPa.

The surface exchange coefficient is

$$C_h = k^2 |V_o| F\left(\frac{z}{z_o}, Ri_B\right) / \left(R\left(\ln\left(\frac{z}{z_o}\right)\right)^2\right) \qquad (17)$$

where

$$F\left(\frac{z}{z_o}, Ri_B\right) = \begin{cases} (1 + b' Ri_B)^{-2} & \text{,stable} \\ 1 - \dfrac{b\, Ri_B}{1+c|Ri_B|^{1/2}} & \text{,unstable} \end{cases} \qquad (18)$$

The constants b and b' are specified as 9.4 and 4.7 respectively while the coefficient c is defined as:

$$c = C^* k^2 b \left(\frac{z}{z_o}\right)^{1/2} / \left(\ln\left(\frac{z}{z_o}\right)\right)^2 \qquad (19)$$

where C* is 7.4 (Louis, 1979).

The exchange coefficient C_h is defined in the same manner as in Louis (1979) so that the wind speed factor is absorbed in it. The bulk Richardson number for the surface layer is defined as:

$$Ri_B = \frac{g\, z\, (\theta_{ov} - \theta_{sv})}{\theta_{sv} |\mathbf{V}_o|^2} \qquad (20)$$

where the subscript v indicates virtual potential temperature. The bulk-Richardson number is a function of the height (z), the difference between the virtual potential temperature of air at the first model level (θ_{ov}) and the surface virtual potential temperature (θ_{sv}) corresponding to the surface temperature from the surface energy balance, and the air speed at the first model level ($|\mathbf{V}_o|$).

The length scale for the surface layer is the Monin-Obuhkov length,

$$L = - \frac{\theta_{sv} u_*^3}{g k \overline{(w'\theta_v')}_o} \qquad (21)$$

The Monin-Obukhov length scale (L) is defined using surface variables: surface virtual potential temperature (θ_{sv}), friction velocity (u_*), and the virtual heat flux at the surface. The eddy diffusivities are

$$K_m = u_* k z \phi_m^{-1}(\frac{z}{L}) \qquad (22)$$

$$K_h = u_* k z \phi_h^{-1}(\frac{z}{L}) \qquad (23)$$

and are functions of the friction velocity (u_*), height (z) and the Monin-Obukhov length scale (L). The dimensionless functions (ϕ_m and ϕ_h) were defined in Eqs. 12 and 13.

The only variables needed to close the surface layer model are T_s and q_s – these are available from the the surface energy balance calculation (§2d) and soil model (§2c), respectively.

c. Soil model

The soil model has been described previously by Mahrt and Pan (1984). The soil hydrology is modeled with a prognostic equation for θ, here the volumetric water content:

$$\frac{\partial \theta}{\partial t} = \frac{\partial}{\partial z}\left(D(\theta) \frac{\partial \theta}{\partial z} \right) + \frac{\partial K(\theta)}{\partial z} \qquad (24)$$

The coefficient of diffusivity (D) and hydraulic conductivity (K) are functions of the volumetric water content (Mahrt and Pan, 1984). Through the extremes of wet and dry soil conditions, the coefficients D and K can vary by several orders of magnitude and therefore can not be treated as constant. Since the soil model is a multi-layer model, a layer integrated form is needed:

$$\Delta z_i \frac{\partial \theta}{\partial t} = D(\theta) \frac{\partial \theta}{\partial z}\Big|_{z_{i+1}} + K(\theta)\Big|_{z_{i+1}} - D(\theta) \frac{\partial \theta}{\partial z}\Big|_{z_i} + K(\theta)\Big|_{z_i} \qquad (25)$$

Eq. 25 is valid for a layer $[z_i, z_{i+1}] = \Delta z_i$. At the surface of the soil, the evaporation is called the direct evaporation. For direct evaporation (E_{dir}) at the air-soil interface ($z = 0$), we have

$$E_{dir} = \left[-D(\theta) \left(\frac{\partial \theta}{\partial z} \right)_0 - K(\theta_0) \right] (1-\sigma_f) + I(1-\sigma_f) \qquad (26)$$

where I is the infiltration rate and σ_f is the plant shading factor. The evaporation can proceed at a potential rate when the soil is wet (demand control stage). When the soil dries out, the evaporation (E) can only proceed at the rate the soil can diffuse water from the lower layer (flux control stage) in which case

$$E < E_p$$

where E_p is the potential evaporation rate. The model also incorporates transpiration (E_t) in the following manner:

$$E_t = E_p \, \sigma_f \, k_v \sum_{i=1}^{2} [\Delta z_i \, g(\theta_i)] \left(1 - \left(\frac{C^*}{S} \right)^n \right) \Big/ \sum_{i=1}^{2} [\Delta z_i] \qquad (27)$$

where k_v is the plant resistance factor and n is taken to be 0.5 (Pan and Mahrt, 1987). The transpiration rate function $g(\theta_i)$ is defined as:

$$g(\theta) = \begin{cases} 1 & , \quad \theta > \theta_{ref} \\ \dfrac{\theta - \theta_{wilt}}{\theta_{ref} - \theta_{wilt}} & , \quad \theta_{ref} \geq \theta > \theta_{wilt} \\ 0 & , \quad \theta_{wilt} \geq \theta \end{cases} \qquad (28)$$

The transpiration limits θ_{ref} and θ_{wilt} refer, respectively, to an upper reference value and the plant wilting factor (Mahrt and Pan, 1984). The canopy evaporation of free water (E_c) is formulated as

$$E_c = E_p \, \sigma_f \left(\frac{C^*}{S} \right)^n \qquad (29)$$

where S, the saturation water content for a canopy surface, is a constant chosen to be 2 mm. The canopy water content (C*) changes as

$$\frac{dC^*}{dt} = \sigma_f \text{Precip} - E_c \qquad (30)$$

Precipitation increases the canopy water content first while evaporation decreases C^*.

Total evaporation is obtained by adding the direct soil evaporation, the transpiration and the canopy evaporation,

$$E = E_{dir} + E_t + E_c \qquad (31)$$

The total evaporation cannot exceed the potential evaporation (E_p, defined in Eq. 39). After obtaining the evaporation, the "surface specific humidity" q_s is calculated from

$$q_s = q_o + \frac{E}{\rho_o C_h} \qquad (32)$$

This quantity is that specific humidity at the surface which allows the bulk aerodynamic relationship to predict E given by (31) and is used to transmit information on the evaporation. Over water, q_s is the saturated surface specific humidity.

Soil thermodynamics are treated with a prognostic equation for soil temperature (T):

$$C(\theta)\frac{\partial T}{\partial t} = \frac{\partial}{\partial z}\left(K_T(\theta)\frac{\partial T}{\partial z}\right) \qquad (33)$$

The heat capacity (C) and the thermal diffusivity (K_T) of the soil are both functions of the soil water content (θ). While the heat capacity (C) is linearly related to θ, the coefficient of thermal diffusivity (K_T) is a highly

nonlinear function of θ and increases by several orders of magnitude from dry to wet soil conditions. The layer-integrated from of (33) is

$$\Delta z_i \, C(\theta_i) \frac{\partial T_i}{\partial t} = K_T(\theta) \frac{\partial T}{\partial z}\Big|_{z_{i+1}} - K_T(\theta) \frac{\partial T}{\partial z}\Big|_{z_i} \qquad (34)$$

The upper boundary condition for the soil thermodynamic model is the soil heat flux, G, an important component in the surface energy balance. It is found from

$$K_T(\theta) \frac{\partial T}{\partial z}\Big|_{z=0} = G \qquad (35)$$

The system is closed except for the potential evaporation, which is defined in the next section.

d. Surface energy balance

Surface temperature is determined from the surface energy balance method:

$$(1-\alpha)S\downarrow + L\downarrow - \sigma T_s^4 = G + H + LE \qquad (36)$$

where the first term on the left-hand side of Eq. 36 is the downward shortwave radiation (solar radiation). The coefficient α is the surface albedo and is a function of surface type. The second term on the left-hand side is the downward longwave radiation. The third term on the left-hand side is the upward longwave radiation and the coefficient σ is the Stefan-Boltzmann constant (equal to 5.6696×10^{-8} W m^{-2} K^{-4}). The first term on the right-hand side of Eq. 36 is the soil heat flux defined in Eq. 35. The second term on the right-hand side is the sensible heat flux. It is defined as:

$$H = \rho_o c_p C_h (\theta_s - \theta_o) \qquad (37)$$

and is a function of the air density (ρ_o), the specific heat for air (c_p = 1004 J kg^{-1} K^{-1}), the exchange coefficient (C_h, Eq. 17) and the difference between the surface potential temperature (θ_s) and the air potential temperature at the first model level (θ_o). The last term on the right-hand side is the latent heat flux and is calculated from Eq. 31.

The potential evaporation (E_p) is calculated using the surface energy balance for the reference state of an open water surface:

$$(1-\alpha)S\downarrow + L\downarrow - \sigma T'^{4}_{s} = G + H' + LE_p \qquad (38)$$

where

$$E_p = \rho_o C_h (q_s^*(T'_s) - q_o) \qquad (39)$$

and

$$H' = \rho_o c_p C_h (T'_s - \theta_o) \qquad (40)$$

The temperature variable (T_s') that appears in Eqs. 38-40 is a fictitious temperature that the surface would have if the soil is sufficiently wet to evaporate at the potential rate. The variable $q_s^*(T'_s)$ in (39) is the saturation specific humidity for this fictitious temperature.

3. Computation Procedures

Computationally, the fictitious surface energy balance for an open water surface is first used to obtain potential evaporation (Eqs. 38-40). On the left-hand side of Eq. 38 are the downward shortwave and longwave radiative fluxes and the upward longwave radiative flux. On the right-hand side are the

soil heat flux, the sensible heat flux and the potential latent heat flux. The key quantity to be determined in this equation is the skin temperature (T_s') that the surface would achieve if it was saturated. Eqs. 38 and 40 are used to form a prediction for T_s' which is then used to predict potential evaporation from Eq. 39 (Mahrt and Ek, 1984). Both the soil heat flux G and the exchange coefficient take on the value from the previous time step.

Using potential evaporation as an upper limit, the soil hydrology package is updated. Eq. 26 is used to obtain direct evaporation from the soil-atmosphere interface. The terms on the right-hand side of Eq. 26 represent the moisture flux at the surface and serve to determine E_p as well as the top boundary condition for Eq. 25. When the evaporative flux is greater than potential, the potential evaporation is used both here and in Eq. 25; otherwise, the calculated flux is used. Transpiration from plants is evaluated using Eqs. 27-28. When precipitation occurs it wets the plant canopy first. Reevaporation occurs at the rate given by Eq. 29 with the conservation equation for canopy water in Eq. 30 (Mahrt and Pan. 1984; Pan and Mahrt, 1987).

The soil thermodynamic model (Eq. 34) is used to obtain the soil heat flux using Eq. 35. In the finite-difference form for Eq. 35, an additional unknown appears; namely, the skin temperature T_s. Because T_s is also an unknown in the surface energy balance (Eq. 36), the surface energy balance can be solved at the same time as Eqs. 34-35 (Pan and Mahrt, 1987). Once we obtain T_s the sensible heat flux is calculated via Eq. 37. When snowcover is present, changes are needed for the interface and these changes are described in Appendix C in Chapter V.

Having obtained T_s using Eq. 36 and q_s using Eq. 32, we use the surface layer parameterization (Eqs. 14-16) to obtain the surface stress, sensible heat flux and latent heat flux. Variables used in Eqs. 14-16 are further defined in Eqs. 17-20. In addition, we calculate the Monin-Obukhov scale height (Eq. 21) and the similarity diffusivity profiles K_m and K_h (Eqs. 22 and 23). The non-dimensional shear and thermal-gradient are given in Eqs. 12 and 13.

In the boundary layer model, we first determine the height of the

boundary layer (Eq. 10). The diffusivity coefficients above the surface layer are obtained using Eqs. 7-9. Finally, the tendencies of wind velocity, potential temperature and specific humidity are calculated via Eqs. 1-3.

REFERENCES

Businger, J. A., J. C. Wyngaard, Y. Izumi, and E. F. Bradley, 1971: Flux-profile relationships in the atmospheric surface layer. *J. Atmos. Sci.*, **28**, 181-189.

Louis, J.-F., 1979: A parametric model of vertical eddy fluxes in the atmosphere. *Bound.-Layer Meteorol.*, **17**, 187-202.

Mahrt, L., J. O. Paumier, H.-L. Pan, and I. Troen, 1984: A boundary layer parameterization for a general circulation model. Final contract report (AFGL-TR-84-0063) to Atmospheric Prediction Branch, Air Force Geophysics Laboratory, Hanscom AFB, Oregon State University, Corvallis.

Mahrt, L., and M. Ek, 1984: The influence of atmospheric stability on potential evaporation. *J. Clim. Appl. Met.*, **23**, 222-234.

Mahrt, L., and H.-L. Pan, 1984: A two-layer model of soil hydrology. *Bound.-Layer Meteorol.*, **29**, 1-20.

Pan, H.-L. and L. Mahrt, 1987: Interaction between soil hydrology and boundary-layer development. *Bound.-Layer Meteor.*, **38**, 185-202.

Troen, I., and L. Mahrt, 1986: A simple model of the atmospheric boundary layer: Sensitivity to surface evaporation. *Bound.-Layer Meteorol.*, **37**, 129-148.

Yang, C.-H., K. Mitchell, D. Norquist, and S. Yee, 1988: Diagnostics for and evaluations of new physical parameterization schemes for global NWP models. In preparation. Atmospheric Prediction Branch, Air Force Geophysics Laboratory, Hanscom AFB.

III. INTERACTION BETWEEN SOIL HYDROLOGY AND BOUNDARY-LAYER DEVELOPMENT

1. Introduction

Surface evaporation can substantially reduce surface heating and subsequent development of the daytime boundary layer. As a result, boundary layer development is quite sensitive to availability of surface moisture as previously demonstrated by McCumber and Pielke (1981).

The interaction among surface evaporation, soil moisture and boundary layer development is quite complex even in the cloudless case as noted schematically in Figure 1. For example, the reduction of boundary layer development is partially limited by negative feedbacks. As surface evaporation moistens the boundary layer, the potential evaporation normally decreases which in turn reduces the actual evaporation. Exceptions include the case of strong downward entrainment of dryer air where low humidities are maintained in spite of significant evaporation.

On a longer time scale, the surface evaporation may significantly deplete the soil moisture. This drying reduces the surface evaporation even though it also acts to increase the potential evaporation. The time scale for this process depends on soil properties as well as atmospheric conditions.

A suitable set of observations which include both adequate measurements of soil variables and atmospheric fluxes are not available to study the various stages of drying. In this paper we use a relatively simple model of the soil-atmosphere system to identify the importance of various interactions related to surface evaporation. The results of this study or any modelling effort will remain necessarily inconclusive until the required measurements become available. Our goal is to suggest which interactions are most important. Such information can assist in the design of future observational

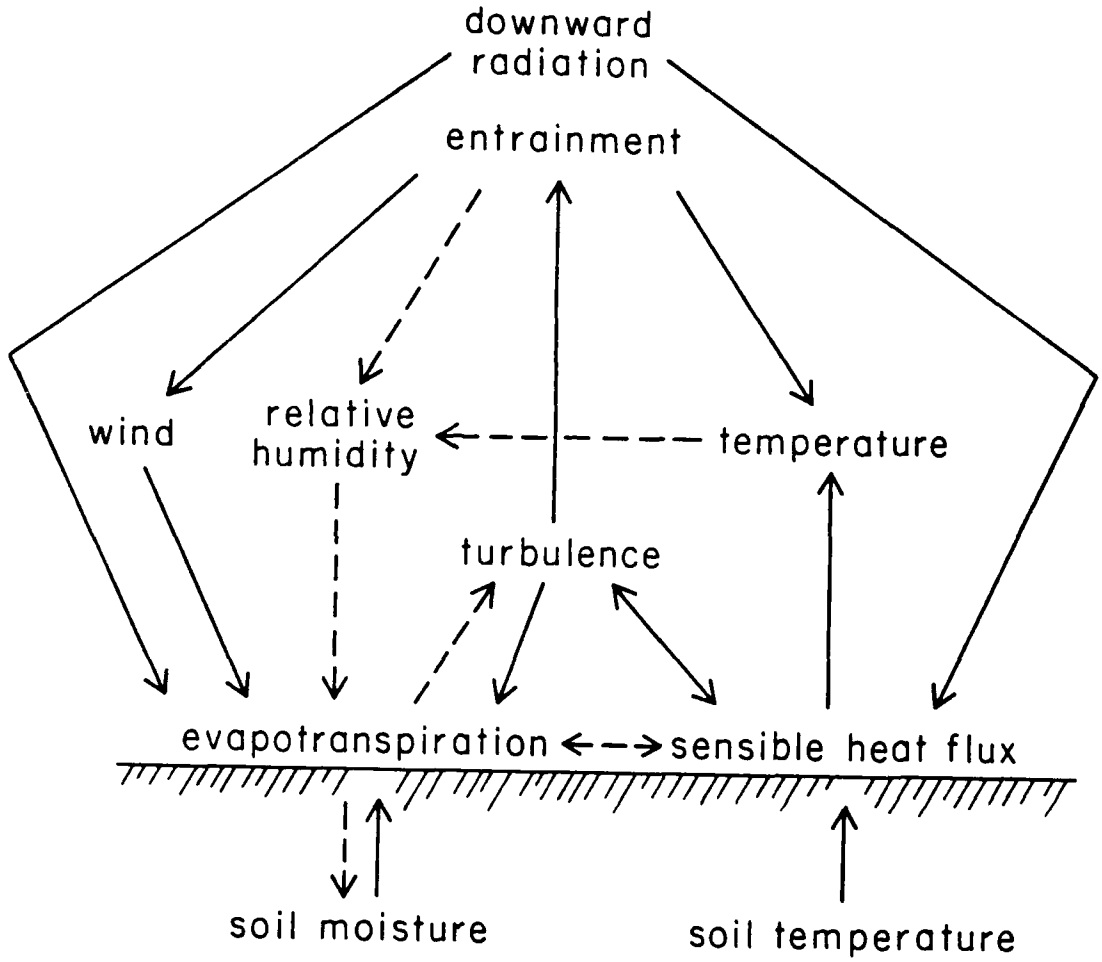

Figure 1. Suspected important interactions between surface evapotranspiration and boundary layer development for conditions of daytime surface heating. Solid arrows indicate the direction of those feedbacks which are normally positive (leading to increases of the recipient variable). Broken arrows indicate negative feedbacks. Two consecutive negative feedbacks make a positive one.

programs as well as help identify parts of the soil-atmospheric modelling which are most critical.

A second goal of this work is to provide a soil-atmosphere boundary-layer model which is sufficiently simple to use in concert with larger scale atmospheric models. Recent numerical experiments by Hunt (1985) indicate that formulations for soil moisture and surface evaporation presently used in general circulation models have serious shortcomings. The present formulation is somewhat more complicated but physically more direct.

2. The model

The atmospheric boundary-layer model of Troen and Mahrt (1986) is coupled to the soil moisture model of Mahrt and Pan (1984). The atmospheric model contains 34 levels between the surface and four kilometers, although approximately the same results can be obtained with as few as 10 levels. The boundary-layer height in the model is determined using a diagnostic relationship based on a modified bulk-Richardson number at each time step. During the day, boundary layer grows in response to turbulence generated by surface heating. When the solar radiation vanishes and if winds are weak, the boundary layer normally collapses to the first model layer (~50 m).

The soil model consists of a thin upper layer, 5 cm thick, which responds mainly to diurnal variations and a thicker lower layer, 95 cm thick, which participates more in seasonal changes of soil water storage. The potential evaporation is formulated with a modified Penman relationship (Mahrt and Ek, 1984). The finite differencing of the soil model has been chosen to minimize truncation errors. This choice is based on comparisons with higher resolution versions of the model up to 100 layers. The truncation errors for the two-layer model, compared to higher resolution versions, led to overestimation of the evaporation of about 10% for the case of clay soil and only a few percent for the case of sand. These errors are small compared to other uncertainties such as treatment of the soil-air interface. Because an accurate description of moisture transport close to the soil surface requires prohibitive vertical resolution, the modelled surface moisture flux is overestimated. This overestimation is compensated by increasing the air-dry values for the soil moisture content to 0.16 to 0.25 for sand and clay, respectively. A 10-minute time step is used in all model runs.

The soil model of Mahrt and Pan (1984) has been generalized to include soil heat flux using the usual thermodynamic relationship

$$C \frac{\partial T}{\partial t} = \frac{\partial}{\partial z} \left(K \frac{\partial T}{\partial z} \right)$$

where the volumetric heat capacity C and the thermal conductivity K are formulated as functions of soil water content as in McCumber and Pielke (1981). A more detailed discussion of the soil-thermodynamic model is given in Appendix A.

The soil drying period, and feedback to the atmosphere, usually extends over several days or even several weeks. Iteration of one-dimensional models for such periods leads to unrealistic buildup of moisture and heat. This buildup does not occur in the atmosphere because of clear-air radiative cooling, horizontal advection of heat and moisture, and consumption of moisture by precipitating systems. Such processes cannot be sensibly formulated within the present framework; instead we specify a climatic advection or restoring term of the form

$$(q_E - q)/\tau_q$$

$$(\theta_E - \theta)/\tau_\theta$$

where q and θ are the actual values of specific humidity and temperature, and q_E and θ_E are pseudo equilibrium values. In the present study q_E is specified to be the initial conditions described below, while θ_E is specified to be height-independent with a value of 270 K. Heat buildup was controlled by specifying a relaxation time of τ_θ = 10 days while long term moisture buildup was prevented with a shorter relaxation time of τ_q = 1 day. While advection is pragmatically specified in this modelling study, it

is also thought to exert a controlling influence on evaporation, at least in some flow situations (McNaughton, 1976).

The atmospheric temperature is initialized with a constant lapse rate (6 K km^{-1}). The temperature at the lowest atmospheric model-level is initialized at 283.6 K. The initial moisture content of the atmosphere is specified to be 3 g kg^{-1} in the lowest kilometer, 2 g kg^{-1} between 1 and 1.2 km, 1 g kg^{-1} between 1.2 km and 2 km, and 0.5 g kg^{-1} above 2 km. Both the initial wind and the time-independent geostrophic wind are specified to be 5 m s^{-1}. The initial volumetric moisture content of the soil is specified to be 0.42, a value which is saturated with respect to clay and super-saturated with respect to sand leading to large percolation through the bottom of the sand for the first day. The initial soil temperature is specified to be identical to the initial value at the lowest atmospheric level (283.6 K).

The short-wave radiative flux formulation of Holtslag and Van Ulden (1983) is applied for 45°N starting with 21 June. Albedo for the Earth's surface is set at 0.25. For simplicity, we neglect the change of soil surface albedo with soil drying which can lead to significant decreases of potential evaporation (Van Bavel and Hillel, 1976). Downward long-wave radiative flux is assigned to be constant corresponding to a black-body temperature of 270 K. Each numerical experiment is iterated for 21 days in order to include the important evaporation stages.

In the next section, four prototype numerical experiments are iterated for sand and clay soil types and for geostrophic wind speeds of 5 m s^{-1} or 10 m s^{-1}. Diffusivity and conductivity coefficients are specified following Clapp and Hornberger, 1978.

3. Drying Stages

Radiative fluxes, wind speed, moisture deficit, and atmospheric stability determine the potential evaporation which in turn forces the actual soil evaporation. When the soil is relatively wet, evaporation will be at the potential rate (atmospheric demand) as determined by atmospheric conditions. When the soil is sufficiently dry, the rate of evaporation is controlled by the soil moisture gradient in the upper part of the soil. The various atmospheric influences on the potential evaporation interact with soil moisture in a non-linear fashion. Some of the candidate interactions are noted in Fig. 1.

We first study the various stages of drying occurring during 21-day iterations by plotting the solar noon values of different variables over sand and clay soils for the two different values of the geostrophic wind speed. Since vegetation, clouds and precipitation are not included, extensive drying and warming will result.

The soil drying and long term boundary-layer changes can be divided into three main stages. In the first stage, the surface evaporation is at the potential rate which decreases slightly with time (Figs. 2-3). In the second stage, the actual evaporation decreases rapidly with time while the potential evaporation increases with time. The second stage leads to a near-equilibrium stage (third stage) where the evaporation and potential evaporation vary slowly with time. The evolution proceeds more rapidly with sandy soil partly because sand has a larger hydraulic diffusivity and conductivity at high volumetric water content and therefore loses more water to percolation. The stages of drying corresponding to Figs. 2-3 are similar to those in the modelling study of Van Bavel and Hillel (1976) except that they included the

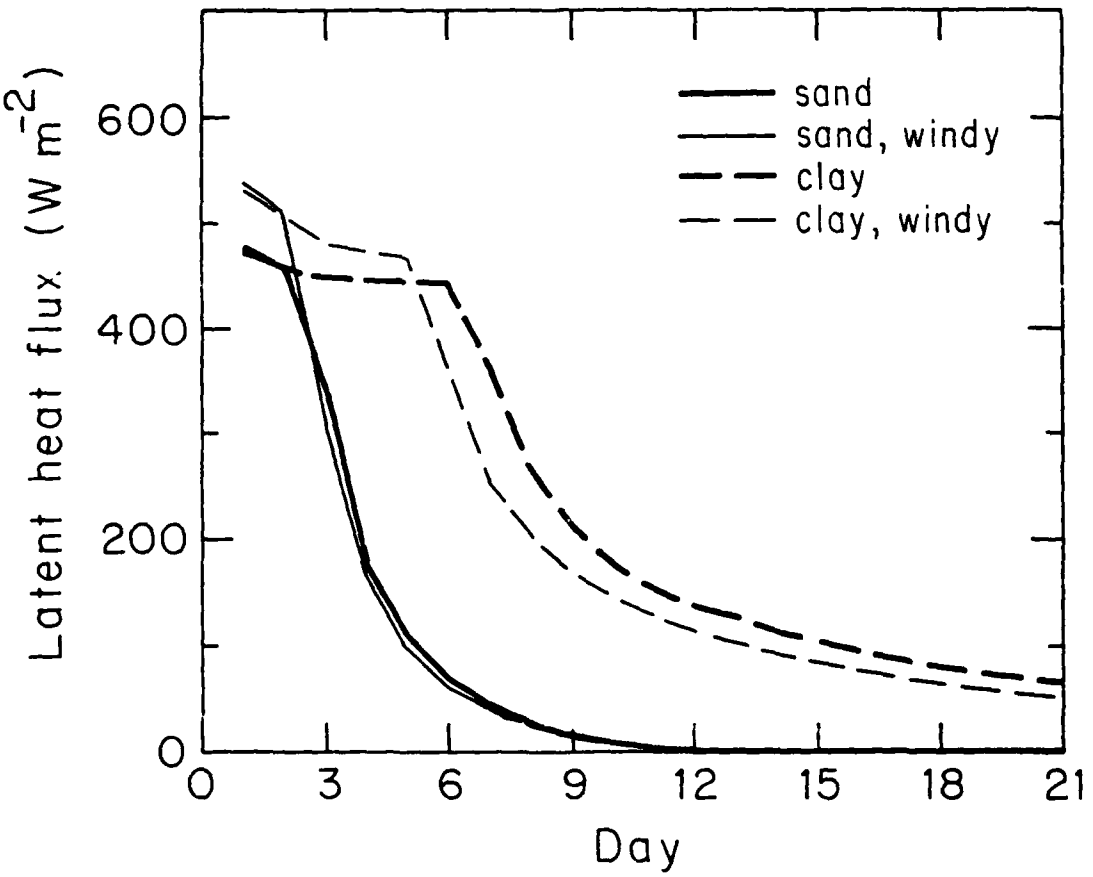

Figure 2. The evolution of the noontime surface evaporation for clay and sand for modest geostrophic winds of 5 ms^{-1} and strong geostrophic winds of 10 ms^{-1}.

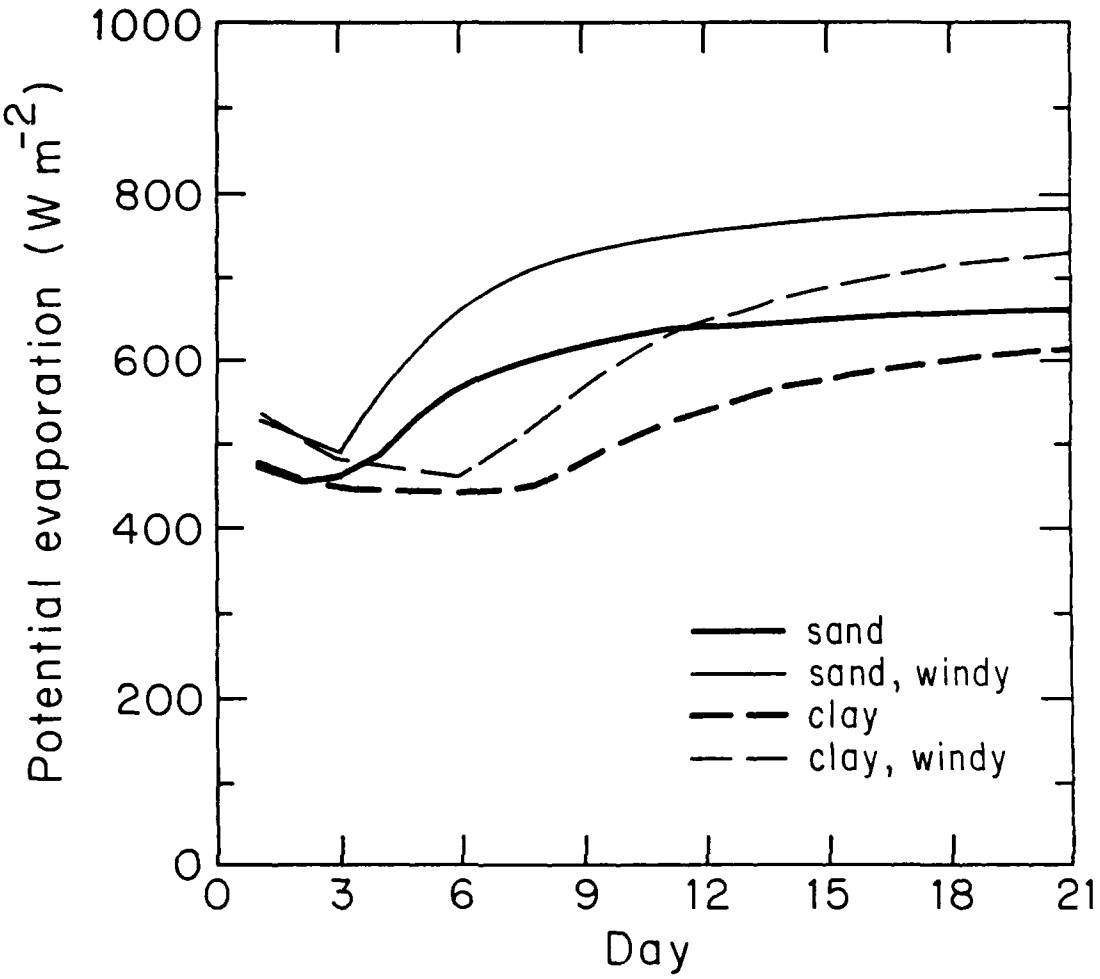

Figure 3. Evolution of the noontime potential evaporation.

dependence of surface albedo on soil wetness and neglected adjustment of the atmosphere to surface evaporation.

a) First stage: potential evaporation

During the first stage when evaporation is at the potential rate, both the specific humidity and the relative humidity increase with time (Fig. 4) leading to a modest decrease of the potential evaporation. In most previous modelling studies of the drying stages, the potential evaporation is held constant. The slight decrease of temperature (not shown) and the corresponding decrease of saturation vapor pressure also cause the potential evaporation to decrease during the first stage of drying. As a result of decreased evaporation, the surface sensible heat flux to the atmosphere increases during this period (not shown) even though the surface temperature decreases.

The boundary layer grows deeper (Fig. 5) each subsequent day partly due to the increase of sensible heat flux. Part of the increase is due to the fact that the boundary layer grows quickly through the weakly stratified layer remaining from the mixed layer of the previous day.

The wind speed significantly influences the surface heat budget and boundary-layer evolution during the first stage of drying since the surface evaporation is at the potential rate which depends on the wind speed. On the other hand, the soil type is of little importance since the evaporation is determined completely by the atmospheric demand during this stage and the influence of soil wetness on albedo is not included here.

b) Second stage: rapid decrease of evaporation

However, the onset of the second stage of drying is determined by the soil type. The clay soil is able to meet the potential evaporation for five

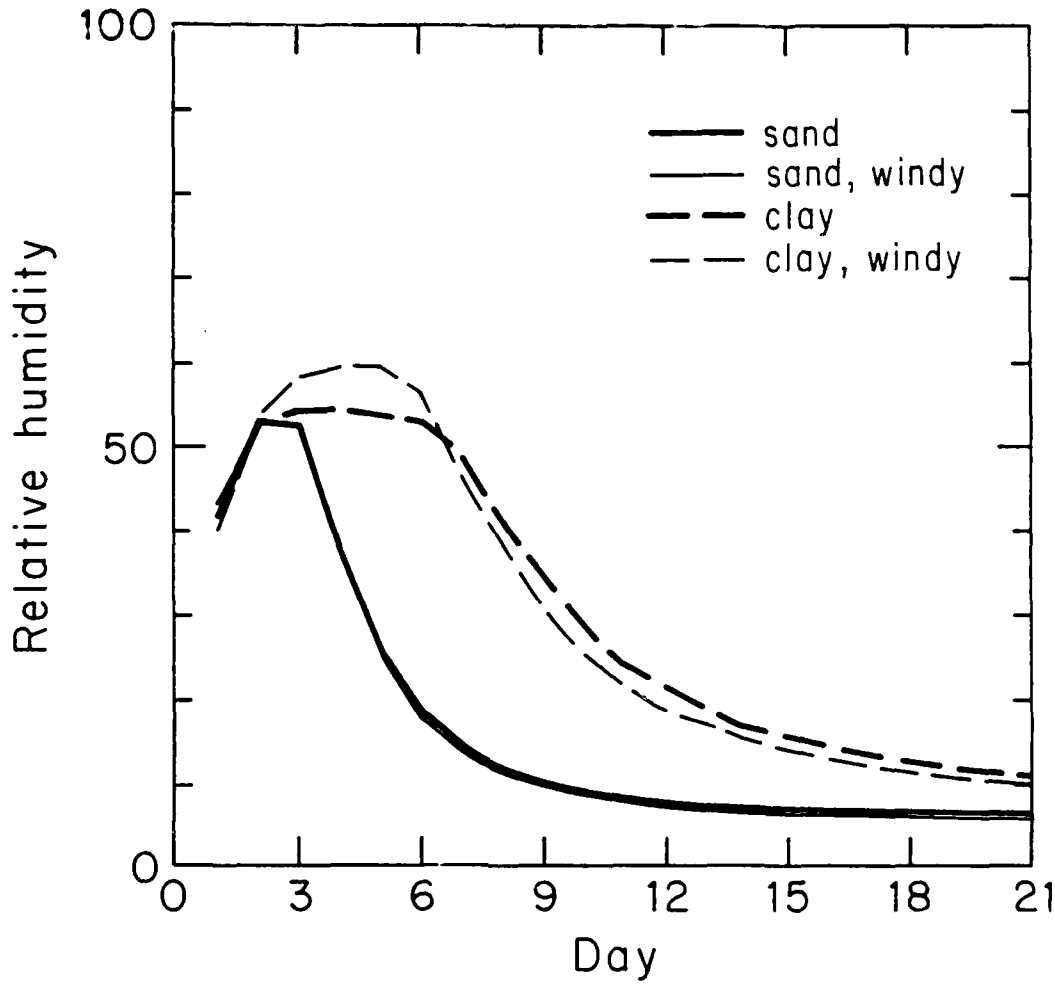

Figure 4. Evolution of the noontime relative humidity at 50 m.

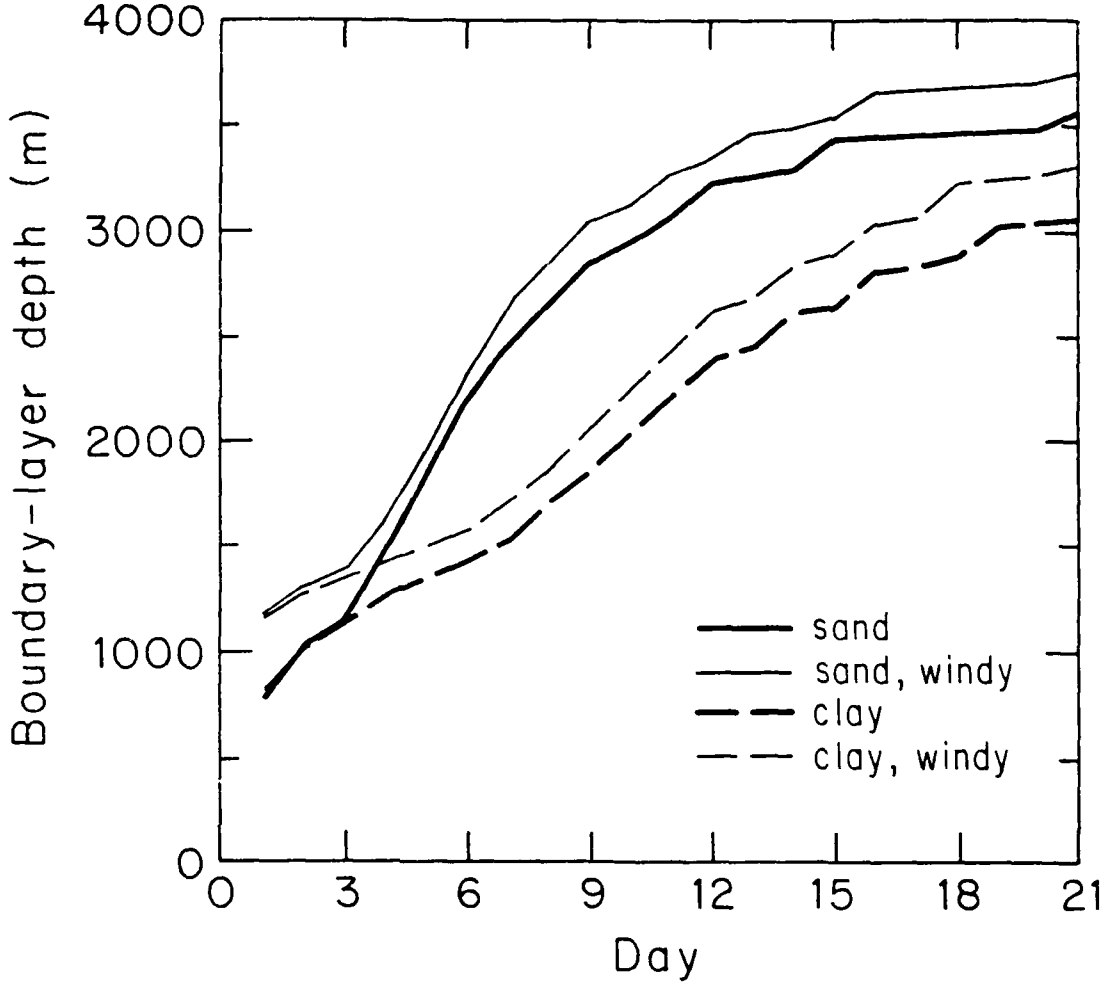

Figure 5. Evolution of the noontime boundary layer depth.

or six days while for sand the evaporation falls significantly below the potential rate during the third day. With the onset of the second stage of drying, the evaporation depends mainly on soil type and is less dependent upon wind speed and other atmospheric properties.

At the same time, atmospheric conditions change rapidly at the beginning of the second stage of drying. The decreasing surface evaporation causes a sharp increase of the surface temperature which in turn increases the surface heat flux and boundary-layer growth. Of special importance is that the downward entrainment of drier air from above the boundary layer can exceed the surface evaporation (Fig. 6a) leading to divergence of the upward moisture flux. This causes drying of the boundary layer. As expected, this net drying of the atmosphere occurs first over sandy soil. Entrainment drying is encouraged by the relatively dry air aloft. Entrainment drying is thought to be frequently important in the evolution of high-plains boundary layers where air above the boundary layer is often dry (Mahrt, 1976). In contrast, with weaker boundary-layer growth and more humid air aloft, the entrainment drying is relatively unimportant (DeBruin, 1983).

The warming and drying cause the relative humidity to decrease and the potential evaporation to increase. However, because of increasing control of evaporation by the drying soil, the actual evaporation decreases rapidly during stage two. The decrease of surface evaporation during stage two causes major changes in the development and structure of the boundary layer. For example, consider the atmosphere profiles at 1000 solar time on day 8 (Fig. 6b). Over sandy soil, the surface evaporation is already quite small leading to large surface heat flux and vertical profiles of the heat flux typical of the convective mixed layer. The heat flux decreases linearly with height

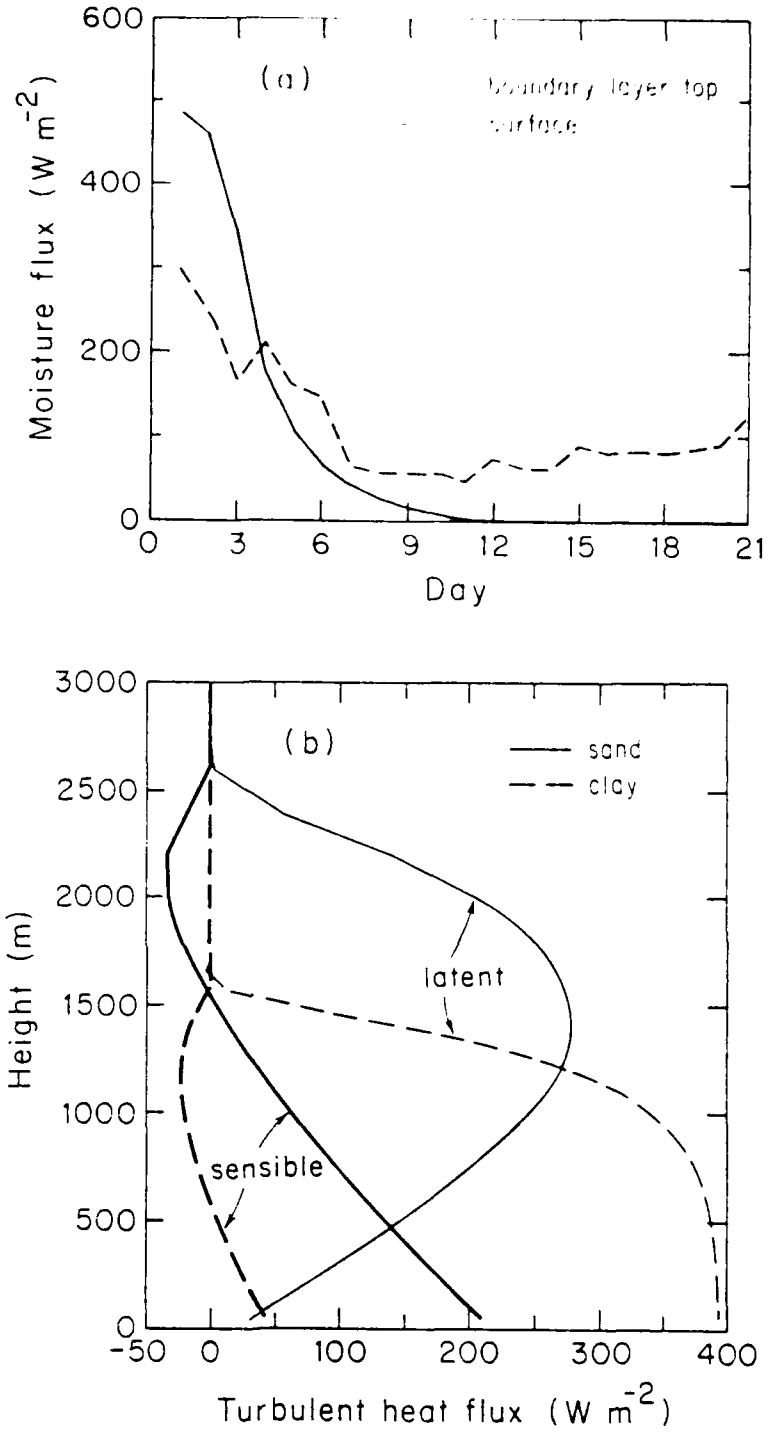

Figure 6. (a) Evolution of the surface moisture flux and the moisture flux near the boundary-layer top over sandy soil with a geostrophic wind speed of 5 ms^{-1}. (b) Vertical profiles of the heat flux and moisture flux at 1000 hours on day 8 with a geostrophic wind speed of 5 ms^{-1}.

reaching negative values near the boundary-layer top due to downward entrainment of warmer air.

In contrast, the surface evaporation over the clay soil is still relatively large leading to smaller surface heating and thinner boundary-layer depth. The upper two-thirds of the boundary layer is characterized by downward heat flux associated with entrainment. This implies that during this period, the mixing in the boundary layer over clay is driven primarily by mean shear whereas mixing in the boundary layer over sand is primarily driven by convection. This example shows how boundary-layer development depends on soil type through the role of surface evaporation.

c) Stage three: near-equilibrium

Eventually the boundary layer approaches an equilibrium state characterized by warm and dry conditions. At noon the surface evaporation becomes negligible for sand and less than 10% of the potential rate over the clay soil. The boundary layer is deep, exceeding four kilometers for sand. At this stage of development, the depth of real boundary layers would normally be constrained by synoptic or cloud-induced subsidence and/or advection of smaller boundary layer depth while some surface evaporation would be maintained by vapor transport in the soil and perhaps transpiration, all of which are neglected in these numerical experiments.

4. Transpiration

Realistic modelling of interaction between the soil and the atmospheric boundary-layer must include the influence of the vegetative canopy. Vegetation moderates diurnal variations. Furthermore, the difference between the three stages of drying are not as distinct since the vegetation removes water from the deeper root zone which dries only slowly. Here the root zone is specified to extend to the bottom of the 1 meter layer. With deep rooted plants the influence of rapid drying of the soil surface is then less important.

We formulate the influence of the vegetative canopy in the simplest possible way which approximates the most important aspects of the canopy; namely, transpiration and shading of the soil surface. These formulations are detailed in Appendix B.

With other conditions the same as in Section 3, the presence of the canopy shading 70% of the ground extends the period of evaporation at the potential rate by several days for clay (Fig. 7); less soil water is removed from near the soil surface to meet the atmospheric demand. The decrease of evapotranspiration during stage two is less compared to the case of no canopy. In other terms, drying of the soil surface does not substantially reduce the transpiration rate in that significant transpiration of deep soil water is maintained during stages 2 and 3. As a further result of the transpiration, the boundary layer is cooler, more moist and not as deep compared to the case with no vegetation. A fourth stage where transpiration decreases due to depletion of deep soil moisture was not studied here.

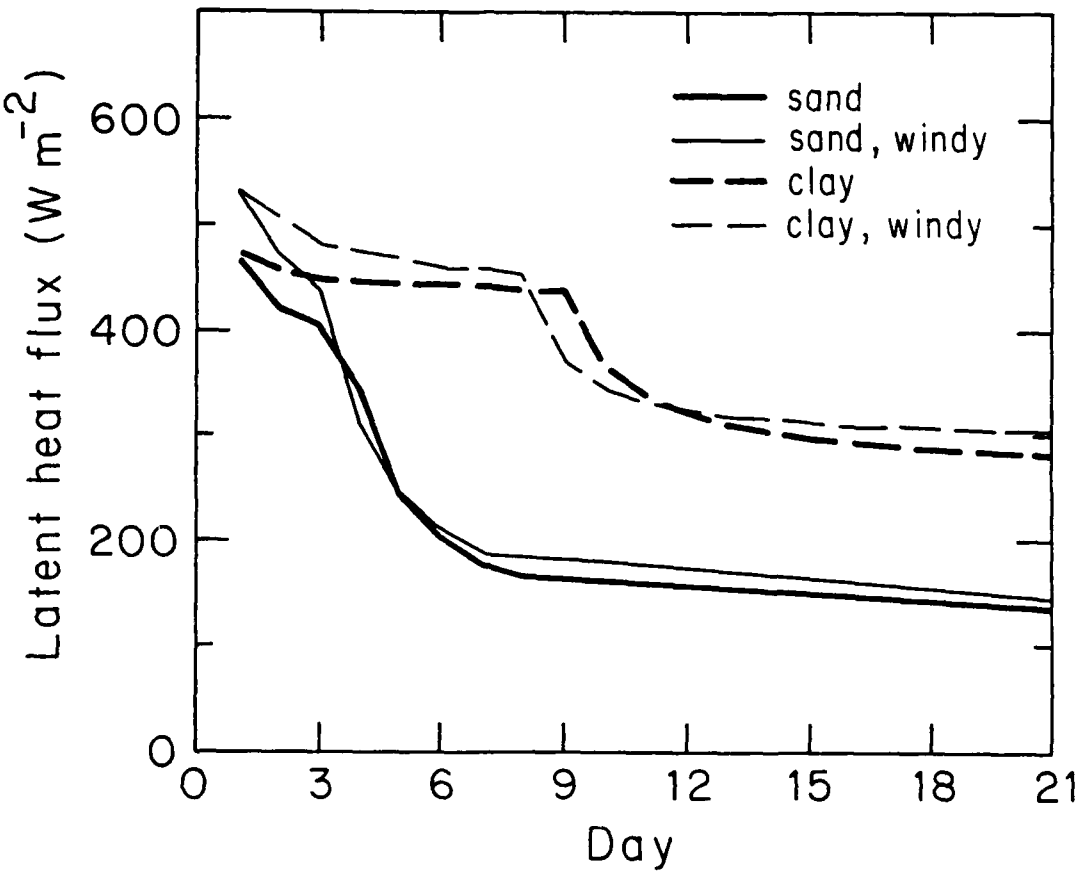

Figure 7. Evolution of noontime evaporation for the case of surface transpiration as compared to the standard case with no transpiration.

5. Influence of Solar Radiation, Climatic Advection, and Soil Properties

It is instructive to study the sensitivity of the above conclusions to variations of the external forcing. This is most simply carried out by neglecting the canopy. We first examine the winter case (solstice) where the incoming solar radiation is much reduced. Under such conditions, the drying stages evolve more slowly (Fig. 8a) due to much lower rates of potential evaporation. The second stage of drying with sand does not begin until after one week, while the evaporation from the clay soil remains near the potential rate during the entire twenty one day period of numerical integration. The potential evaporation reaches only about 100 W m^{-2} during mid-day so that transport of moisture within the clay soil is able to meet the demand. During the night, vertical transport within the clay is able to restore the soil moisture near the surface to the extent that the evaporation is near potential during the subsequent daytime period.

In actual atmospheric conditions, advection of heat and moisture can significantly alter the boundary-layer evolution even on short time scales. Here we study the influence of advection as formulated in Section 2 for the summertime case. With less dry-air advection, the boundary layer moistens which reduces the potential evaporation and significantly delays the transition to the second stage of drying for clay, as is evident in Figure 8b, for the case where the relaxation time for moisture is increased to 10 days. With reduced cold-air advection (not shown), the boundary layer heats up and grows faster which in turn increases the downward flux of dry air.

When the soil is thinner, it stores less moisture. As a result, the second stage of drying begins slightly earlier. As an example, decreasing the soil depth from 1 m to 1/2 m advances onset of the second stage of drying by only a day or less, depending on soil type (Fig. 8c). However, the influence

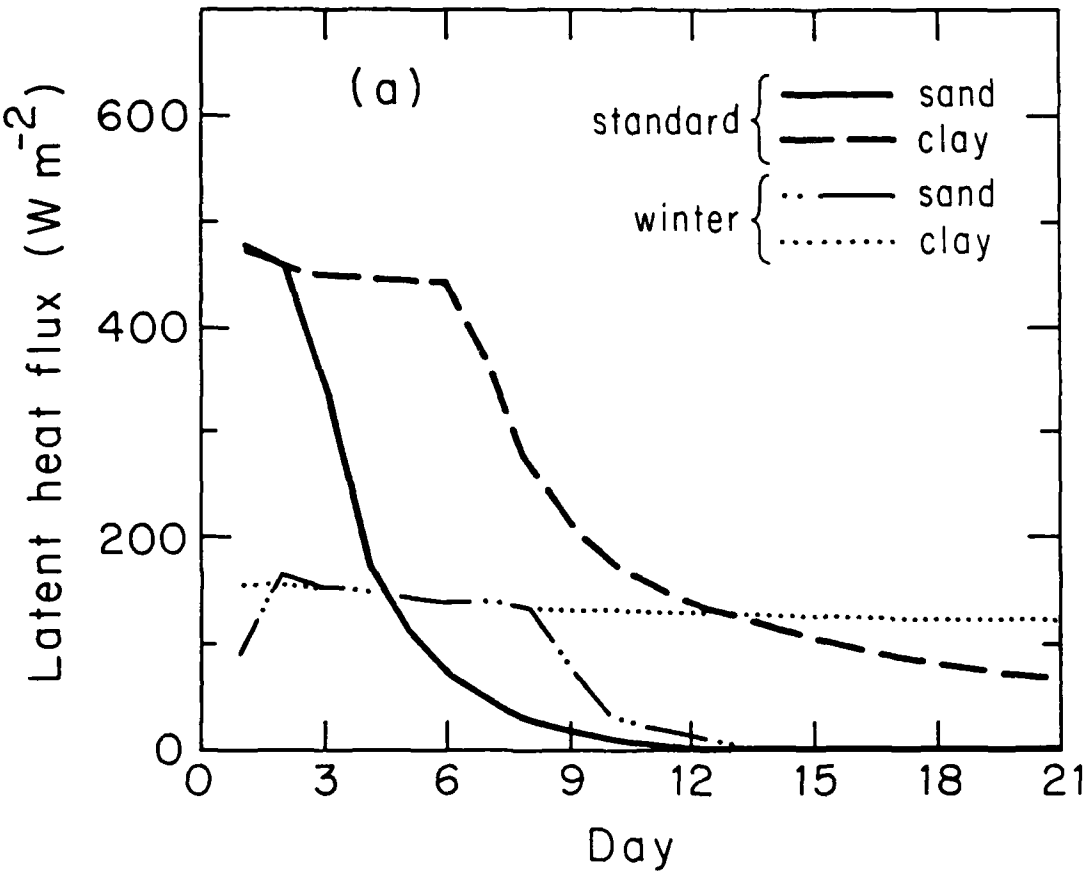

Figure 8. The noontime surface evaporation for the special cases of (a) winter solstice sun angle, (b) reduced dry-air advection and (c) thin soil depth, all compared to the standard case.

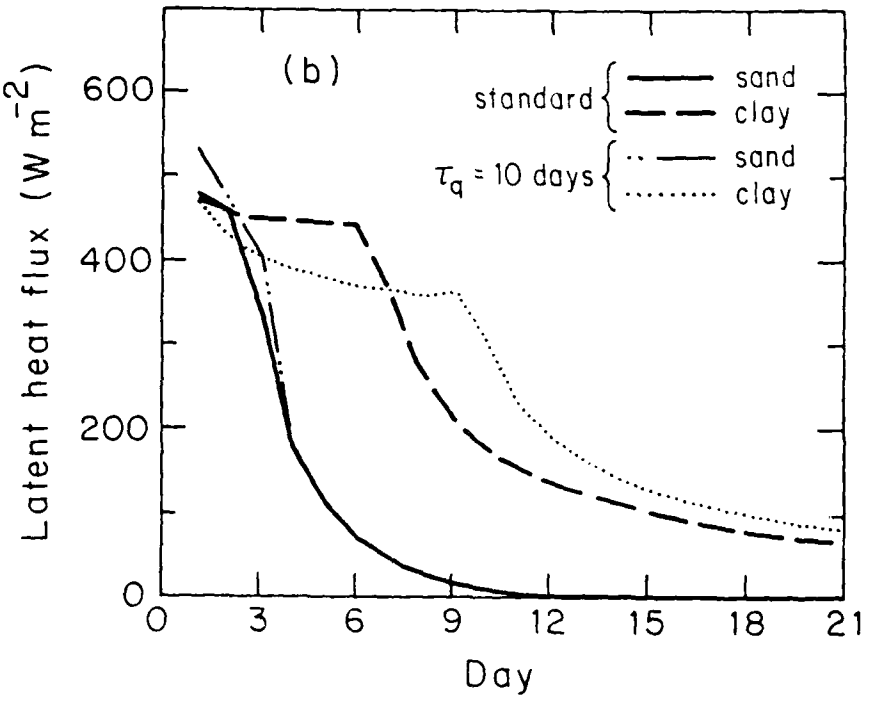

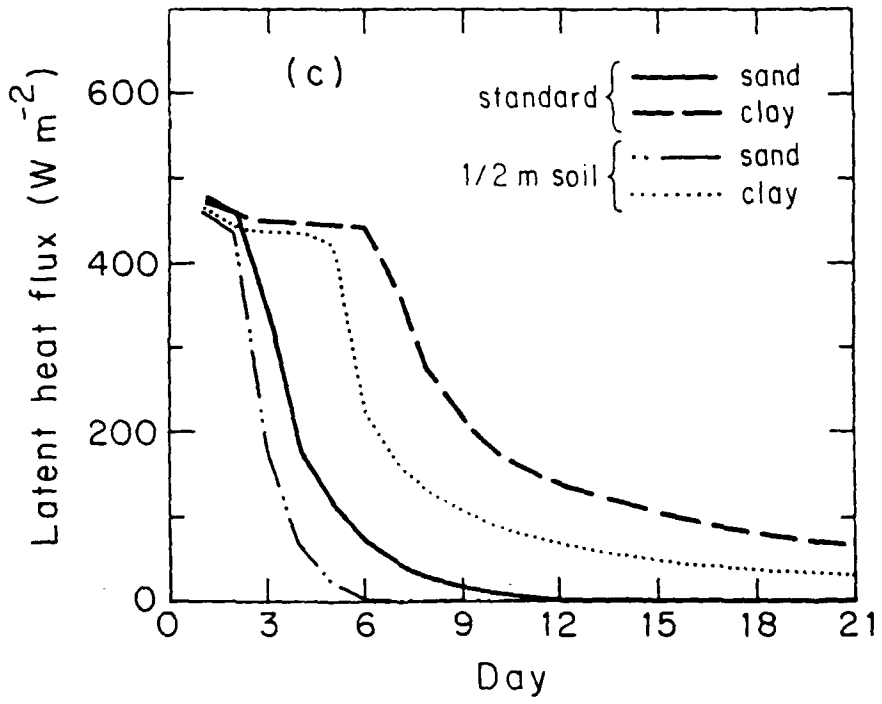

Figure 8. (continued)

of thinner soil becomes more significant at later times when the moisture content of the thin soil decreases to near air-dry values. The surface evaporation rates at stages 2 and 3 are only a fraction of the corresponding values for a 1 m thick soil.

Often natural surfaces are covered by organic "debris" or "litter" consisting of dead grass and leaves, conifer needles and other organic matter. Such materials cover a major portion of natural land surfaces. When dry, these materials are characterized by extremely low hydraulic conductivities; such surfaces then act as a moisture barrier and the soil becomes decoupled from the atmosphere on short time scales in cases with little transpiration.

The thermal and hydraulic properties of such organic debris are not known with quantitative accuracy. Better known are the properties of peat soils which are between those properties of organic surface material and those of other soils. In this study, we use the thermal and hydraulic properties for peat adopted by McCumber and Pielke (1981). The saturation water content for peat is nearly twice that of the other soil types. The hydraulic conductivity coefficient of saturated peat is similar to that of other soil types at or near saturation. However, as soil moisture decreases, the hydraulic conductivity for peat decreases rapidly to values several orders of magnitude smaller at water contents comparable to the saturation values of sand and clay. At this stage the peat becomes an effective moisture barrier which decouples direct exchange between the soil and atmosphere.

Several numerical iterations were performed where the upper 5 cm was specified to be peat (not shown). The contribution of the surface evaporation to the surface energy balance quickly becomes negligible. In any event, the usual neglect of organic litter in large scale modelling studies probably

leads to significant overestimation of evaporation from the soil over vegetated natural surfaces. Results are only useful qualitatively since the interface between the organic material and the more conventional soil cannot be modelled with certainty. Furthermore, organic litter can reduce run-off by absorbing more rain water. This can actually lead to increased evaporation at a later stage during near drought conditions.

6. Diurnal Variation

As an example, the diurnal variation of the surface energy budget is shown in Fig. 9 for the standard case with sandy soil during days 3 and 4, which corresponds to the beginning of the second stage of soil drying. Note that on day 4, the evaporation is significantly reduced leading to greater sensible heat flux to the atmosphere.

The surface evaporation increases during the morning as dictated by increasing net radiation and resulting increase of potential evaporation (Fig. 9). This rapid increase of evaporation suppresses sensible heat flux to the atmosphere and leads to temporary retardation of heat flux to the soil. By late morning, the soil surface layer has dried to the extent that the evaporation becomes subpotential and decreases in an absolute sense. With less evaporation, the sensible heat flux to the atmosphere increases rapidly and more heat is transported into the soil. Note that the heat flux to the soil peaks before the sensible heat flux to the atmosphere, since the soil warms more rapidly than the atmosphere. The delay of the diurnal increase of sensible heat flux to the atmosphere is often observed (e.g., Oke, 1978).

7. Conclusions

In the above modelling study, the soil drying advances in three stages as has been previously observed. In the first stage, the rate of surface evaporation proceeds at the potential rate and therefore depends mainly on atmospheric conditions such as wind speed, relative humidity and incoming solar radiation. Surface heating is limited by the surface evaporation and the boundary layer may develop primarily due to shear. In such cases, weak downward heat flux can extend downward throughout much of the boundary layer. In the second stage, the evaporation decreases rapidly to well-below potential

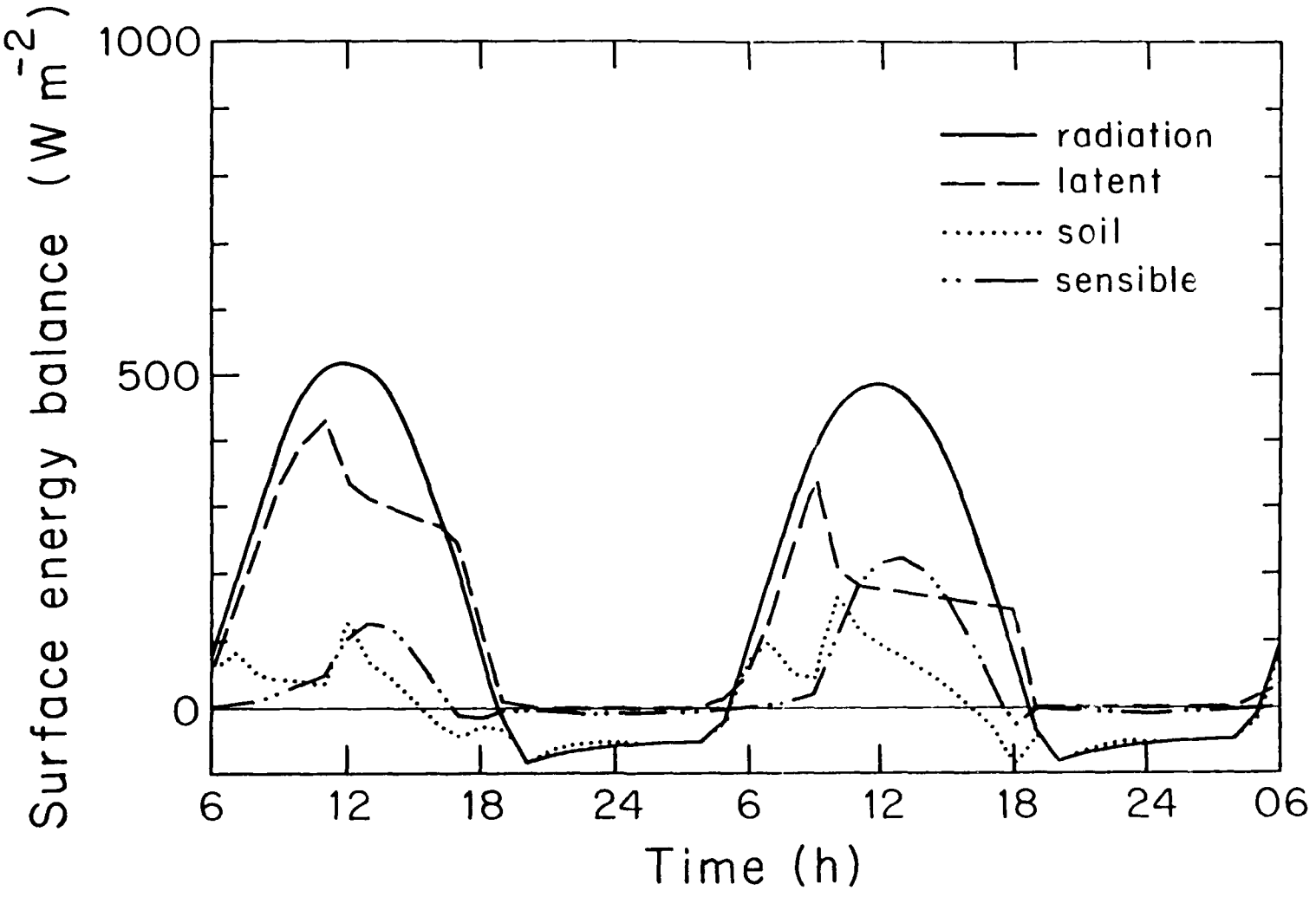

Figure 9. The diurnal variation of the surface energy balance over sand with a geostrophic wind of 5 ms^{-1}. Positive net radiation corresponds to a net heat gain at the surface while positive values of the other terms correspond to a heat flux away from the surface.

values and becomes controlled more by the moisture gradients in the soil. In the final stage, the drying reaches a small near-equilibrium value. The surface heat flux becomes much larger than the latent heat flux and upward heat flux extends upward to the entrainment region of the boundary layer top.

The duration of each stage depends critically on the soil type as well as on atmospheric conditions. The occurrence of dry organic debris, such as leaves and dead grass, appears to partially decouple the atmosphere and soil resulting in significant slowing of the advance of the second and third stages of drying. The development of significant transpiration reduces the importance of direct surface evaporation from the soil and thus reduces the distinction between the three stages. Entrainment drying of the boundary layer can become important with dry air aloft and strong surface heating. The latter is encouraged by dry soil conditions.

Climatic cooling and drying was specified to simulate advection, clear air radiative cooling and removal of moisture by convective clouds. Such mechanisms are not necessary when simulating only one diurnal cycle or when the one-dimensional model is combined with a larger scale model We are presently using the boundary layer-soil model with the global spectral model of Brenner et al., 1984, as reported further by Yang et al., 1988.

Acknowledgements

The authors gratefully acknowledge the helpful comments of Stuart Childs of the Soil Physics Department at Oregon State University. This work was supported by Contract No. F19628-84-K-0044 from AFGL, Cambridge, MA, U.S.A. Computational assistance provided by Mr. Wayne Gibson is gratefully appreciated.

APPENDIX A: The Two-Layer Soil Thermodynamic Model

The two-layer structure used for the soil moisture model (Mahrt and Pan, 1984) should adequately resolve the diurnal variation of the soil thermodynamics; the thin top layer with a thickness of 5 cm can provide an estimate of the sharp diurnal thermal gradient and the thicker second layer (95 cm) allows us to incorporate heat storage and seasonal variations and to specify a constant lower boundary soil temperature which, in reality, varies on the annual time-scale.

The heat conduction equation, neglecting horizontal interactions, is given as

$$C \frac{\partial T}{\partial t} = \frac{\partial}{\partial z} \left(K \frac{\partial T}{\partial z} \right) \qquad \text{(A-1)}$$

where C is the volumetric heat capacity and K is the thermal conductivity. The heat capacity for water is 4.2×10^6 W m^{-3} K^{-1} and for soil is chosen as 1.26×10^6 W m^{-3} K^{-1} for simplicity even though it varies slightly for different soil types. The heat capacity of the composite soil is simply defined as

$$C = (1 - \theta) C_{soil} + \theta C_{water},$$

where θ is the volumetric water content. In this definition, we have neglected the contribution due to air following DeVries (1975). The thermal conductivity, K, is strongly dependent on the soil moisture content. Similar to McCumber and Pielke (1981), we also adopted the functional form for K following Al Nakshabandi and Kohnke (1965):

$$K(\theta) = \begin{cases} 420 \exp(-P_f + 2.7) & P_f \leq 5.1 \\ 0.1722 & P_f > 5.1 \end{cases} \qquad \text{(A-2)}$$

where $P_f = \log_{10}[\psi_s(\theta s/\theta)^b]$. The factors ψ_s, θ_s, and b are functions of the soil textural class (Clapp and Hornberger, 1978).

In the finite difference formulation, the model equation (A-1) will be integrated first over the two layers to explicitly express the flux $K\,\partial T/\partial z$, through each layer. The model grid staggering is presented in Fig. A1 and the level $\tilde{z}_k$ represent the level along which the temperature T_k is the same as the layer-average T (in this study, the mid-point of the layer is selected). The layer integrated equation becomes

$$C(\tilde{\theta}_K)\,\frac{\partial \tilde{T}_K}{\partial t} = \frac{1}{\Delta z_K}\left[K(\theta_{K-1})\,\frac{\partial T}{\partial z}\Big|_{z_{K-1}} - K(\theta_K)\,\frac{\partial T}{\partial z}\Big|_{z_K}\right]. \qquad \text{(A-3)}$$

where the gradient $\partial T/\partial z$ is evaluated as

$$\frac{\partial T}{\partial z}\Big|_{z_K} = \frac{\tilde{T}_K - \tilde{T}_{K+1}}{(\tilde{\Delta z})_K} \quad . \qquad \text{(A-4)}$$

At the top of the model, the surface temperature T_s will be used to form a one-sided estimate of the gradient

$$\frac{\partial T}{\partial z}\Big|_{z_0} = \frac{\tilde{T}_s - \tilde{T}_1}{0.5\Delta z_1} \quad . \qquad \text{(A-5)}$$

The gradient at the bottom of the model is estimated using a specified constant temperature, T_{bot} (Fig. A1).

In order to interface the soil thermodynamics into the model, the prediction of $\tilde{T}_k$ using (A-3) is performed using the fully implicit Cranck-Nicholson scheme given by

$$\tilde{T}_k^{(n+1)} - \tilde{T}_k^{(n)} = \frac{\Delta T}{C(\tilde{\theta}_x)}\,\frac{1}{(\tilde{\Delta z})_k}\left[K(\theta_{k-1})\,\frac{\partial T}{\partial z}^{(n+1)}\Big|_{z_{k-1}} - k(\theta_k)\,\frac{\partial T}{\partial z}^{(n+1)}\Big|_{z_k}\right] \qquad \text{(A-6)}$$

where the superscripts designate the time levels.

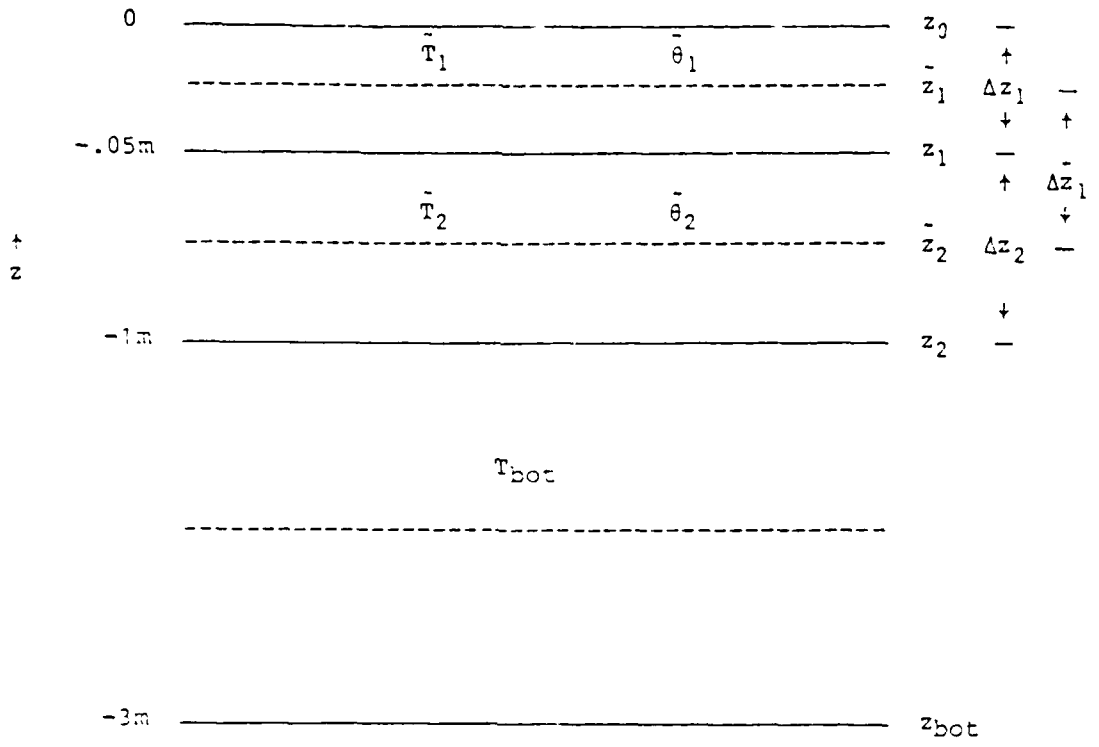

Fig. A-1. The geometry of the soil thermodynamics.

Figure A-1. The geometry of the soil thermodynamics.

For moist soil, a small difference in the thermal gradient in (A-5) can lead to large soil heat flux because the thermal conductivity increases rapidly with soil moisture content. For this reason, the surface energy balance equation must be updated simultaneously with the soil thermodynamic equations so that the resulting surface temperature and soil temperature satisfy the surface energy balance constraint at the next time step.

APPENDIX B: Transpiration

This appendix describes the transpiration formulation for the results in Section 4. We want to preserve the distinction since the direct soil evaporation is most appropriately related to the soil moisture of an upper thin layer while water for transpiration originates more from the deeper root zone. The total evaporation can be written as

$$E = E_{dir} + E_T + E_C \tag{B-1}$$

where E_{dir} is the direct evaporation from the soil, E_T is the transpiration, and E_C is the evaporation of precipitation intercepted by the canopy. Each of the evaporation terms on the right-hand side are proportional to the potential evaporation E_p (we do not differentiate between ground temperature and "leaf" temperature in this study).

Vegetation reduces the direct evaporation from the soil by shading the ground and reducing the wind speed near the ground. The reduction of wind speed can be posed in terms of increased surface roughness parameter and increased displacement height.

The reduction of solar radiation reaching the ground surface through the vegetation can be expressed as a linear dependence on the shading factor by neglecting complexities due to varying sun angle.

To minimize the number of parameters, we relate both the influences of shading and wind speed reduction to the shading factor σ_f according to the format

$$E_{dir} = E_{soil} (1 - \sigma_f) \tag{B-2}$$

E_{soil} is the evaporation from the soil in the absence of vegetation as discussed in Section 2.

> Transpiration is related to the density of vegetation and the soil moisture content. For the two-layer model, these influences are most simply included with the following formulation for transpiration

$$E_T = E_p k_v \sigma_f \frac{z_1}{z_2} g(\theta_1) + \frac{(z_2 - z_1)}{z_2} g(\theta_2)[1 - (C^*/S)^n]$$

$$g(\theta) = \begin{cases} 1 & \theta > \theta_{ref} \\ \dfrac{\theta - \theta_{wilt}}{\theta_{ref} - \theta_{wilt}} & \theta \leq \theta_{ref} \\ 0 & \theta \leq \theta_{wilt} \end{cases} \qquad \text{(B-3)}$$

where z_1 is the depth of the upper layer (here 5 cm) and z_2 is the depth of the entire two layers (1 m). We have assumed that the root uptake rate is independent of depth within a given layer. After consulting numerous studies, the wilting point, θ_{wilt}, where root uptake ceases, is assigned to be 0.12. The parameter θ_{ref} is the soil moisture content where the soil moisture deficit begins to reduce root uptake and transpiration. θ_{ref} is chosen to be 0.25 which is significantly below the saturation values for most soil types.

C* is the canopy water content and S is the canopy water capacity and are included to represent reduction of evaporation of heat surfaces covered by a water film. The coefficient k_v is the plant resistance factor chosen to be 1.0 and σ_f is specified to be 0.7. The product of $k_v\sigma_f$ is similar to the commonly used plant coefficient. The parameter n is chosen to be 1/2 to be consistent with the interception model discussed below.

Some dewfall occurs in the iterations reported in Section 4. Interception is modelled as

$$\frac{dC^*}{dt} = \sigma_f P - E_C \qquad \text{(B-4)}$$

$$E_C = \sigma_f (C^*/S)^n E_p$$

The storage capacity of the canopy, S, is chosen to be 2 mm. P is the precipitation or dewfall rate. This interception model is similar to that of Rutter et al. (1971) except that:

1) the throughfall parameter is replaced with the closely related expression $1 - \sigma_f$ in order to reduce the number of parameters;
2) the evaporation factor C^*/S is multiplied by σ_f to account for the asymptotic limit that canopy evaporation vanishes as the canopy vanishes; and
3) n is chosen to be less than unity to correspond to a finite time for the canopy to dry following rainfall as modelled in Deardorff (1978).

Based on the work of Leyton et al. (1967), a value of $n = 1/2$ is inferred which is somewhat less than the $n = 2/3$ value chosen by Deardorff (1978).

Once the canopy is saturated ($C^* = S$), all additional rainfall is assumed to fall through to the ground. This is analogous to assuming that drip processes occur instantaneously so that the canopy is never temporarily "supersaturated."

References

Al Nakshabandi, G., and H. Kohnke, 1965: Thermal conductivity and diffusivity of soils as related to moisture tension and other physical properties. Agric. Met., 2, 271-279.

Brenner, S., C-H. Yang, and K. Mitchell, 1984: The AFGL global spectral model: Expanded resolution baseline version. Report no. AFGL-TR-84-0308, 72 pp. [Air Force Geophysics Laboratory/LYP, Hanscom AFB, MA, 01731, USA] ADA 160370.

Clapp, R.B., and G.M. Hornberger, 1978: Empirical Equations for Some Soil Hydraulic Properties. Water Resources Res., 14, 601-604.

Deardorff, J., 1978: Efficient prediction of ground surface temperature and moisture with inclusion of a layer of vegetation. J. Geophys. Res., 83, 1889-1903.

DeBruin, H.A.R., 1983: A model for the Priestly-Taylor parameter α. J. Cli. Appl. Met., 22, 572-578.

DeVries, D.A., 1975: Heat transfer in soils. In: Heat and Mass Transfer in the Biosphere (D.A. DeVries and N.H. Afgan, eds.), Scripta Book Co., Washington, D.C., pp. 5-28.

Holtslag, A.A.M., and A.P. Van Ulden, 1983: A simple scheme for daytime estimates of surface fluxes from routine weather data. J. Cli. Appl. Met., 22, 517-529.

Hunt, B.G., 1985: A model study of some aspects of soil hydrology relevant to climatic modelling. Quart. J. R. Met. Soc., 111, 1071-1085.

Leyton, L., E.R.C. Reynolds, and F.B. Thompson, 1967: Rainfall interception in forest and moorland. In: Forest Hydrology (W.E. Sopper and H.W. Lull, eds.), Pergamon, Oxford, pp. 163-178.

Mahrt, L., 1976: Mixed layer moisture structure. Mon. Wea. Rev., 104, 1403-1407.

Mahrt, L., and M. Ek, 1984: The influence of atmospheric stability on potential evaporation. J. Cli. Appl. Met., 23, 222-234.

Mahrt, L., and H.-L. Pan, 1984: A two-layer model of soil hydrology. Bound.-Layer Met., 29, 1-20.

McCumber, M.C., and R.A. Pielke, 1981: Simulation of the effects of surface fluxes of heat and moisture in a mesoscale numerical model soil layer. J. Geophy. Res., 86, 9929-9938.

McNaughton, J.L., 1976: Evaporation and advection. I. Evaporation from extensive homogeneous surfaces. Quart. J. Roy. Met. Soc., 102, 181-191.

Oke, T., 1978: Boundary Layer Climates, Methuen, London, 372 pp.

Rutter, A.J., K.A. Kershaw, P.C. Robins, and A.J. Morton, 1971: A Predictive Model of Rainfall Interception in Forests, 1. Derivation of the Model From a Plantation of Corsican Pine. Agric. Met., 9, 367-384.

Troen, I., and L. Mahrt, 1986: A simple model of the boundary layer: Sensitivity to surface evaporation. Bound.-Layer Met. (in press).

Van Bavel, C.H.M., and D.I. Hillel, 1976: Calculating potential and actual evaporation from a bare-soil surface by simulation of concurrent flow of water and heat. Agric. Met., 17, 453-476.

Yang, C.-H., K. Mitchell, D. Norquist, and S. Yee, 1988: Diagnostics for and Evaluations of New Physical Parameterization Schemes for Global NWP Models. In preparation, Air Force Geophysics Laboratory, Hanscom AFB, MA.

IV. GRID-AVERAGED SURFACE FLUXES

1. Introduction

Numerical models of geophysical flows require parameterization of the transport by all motions which are not resolved by the grid. The parameterization of such "subgrid-scale flux" at the surface is normally based on boundary layer similarity theory and definition of a surface exchange coefficient.

Formulations of sub-grid scale flux suffer several major problems:

a) They do not explicitly include transport by motions which are larger than turbulent scale but still small enough to be subgrid scale. These motions include nonlinear gravity waves, cloud-induced motions and flow responding to subgrid terrain and differential heating. Transport by such motions is poorly understood because they are usually observed with significant sampling problems. Since the smallest resolved motion and the largest subgrid-scale motions are of comparable scale and may be strongly interactive, the transport by the largest subgrid-scale motions cannot be simply related to the resolved gradient.

b) The surface is inhomogeneous on subgrid scales. Because the transport by the turbulence is related to gradients and stability in a nonlinear way, the area-averaged flux is not related to the area-averaged gradient in a simple manner. For example the vertical gradient of the area-averaged potential temperature often corresponds to stable stratification even though the area-averaged heat flux is upward; that is, strong turbulence in small regions of unstable stratification can dominate the area-averaged heat flux which then becomes "counter" to the area-averaged vertical gradient of potential temperature. Small subregions of unstable

stratification could result from local terrain elevation, dryer soil, or cloud-free pockets. As a result of similar averaging effects, the downward grid-averaged heat flux in the stable case may be substantially larger than predicted by the stability based on grid-averaged variables.

c) With stronger subgrid-scale inhomogeneity, the turbulence may not achieve equilibrium with the local surface in which case practical representations of turbulence are not applicable.

The above averaging problems are rarely formally recognized in modeling studies. Wyngaard (1982) and others have examined the mathematics of grid-volume averaging for cases where the grid volume is both larger and smaller than the characteristic scale of the turbulence. Sud and Smith (1984) simulate idealized grid-volume averaging by assuming that the surface bulk Richardson number varies within a grid box according to a Gaussian frequency distribution. The surface exchange coefficient for the bulk aerodynamic relationship, which depends on the Richardson number, is then averaged over the hypothetical grid volume. The resulting averaged exchange coefficient exhibits a much smoother dependence on stability which eliminates troublesome numerical oscillations. Further application of the smoothed exchange coefficient is found in Sud and Smith (1985).

Analogous problems have been studied with respect to longer term time averaging. Saltzman and Ashe (1976a,b) have considered contributions to the monthly averaged heat flux due to diurnal and synoptic variations and how such contributions relate to a local flux-gradient formulation. Mahrt et al. (1986) have studied certain averaging problems associated with use of the surface flux relationships with long time steps or omission of the diurnal variation. For the data sets examined, the actual long-term surface heat flux

was upward and counter to the long-term vertical gradient of potential temperature.

In the present study, we examine the influence of horizontal averaging on the relationship between the flux and gradients. In particular we horizontally average the local surface flux relationship to show how the nonlinear dependence of the exchange coefficient on local gradients generally leads to larger flux in the stable case than would be predicted by the usual neglect of spatial averaging.

The formal grid-area averaging of the flux-gradient relationship is developed in Section 2. In Section 3, the surface exchange coefficient is averaged for idealized distributions of the Richardson number. Low-level aircraft observations in the stable boundary layer are considered in Section 4. In Section 5, various averaging terms are evaluated by using a mesoscale model and viewing it as a grid box of a larger scale general circulation model. A modified relationship for the surface exchange coefficient is constructed in Section 6.

2. Formulation

In numerical models, the flow is automatically divided into the resolved part and the unresolved or subgrid part. The flux divergence due to the subgrid flow influences the resolved flow and must be parameterized. In this study we are concerned with fluxes from the earth's surface through the lowest atmospheric level in the model.

We partition the flow at the lowest model level as

$$\phi(x,y,t) = [\phi] + \hat{\phi}(x,y,t) \tag{1a}$$

where $[\phi]$ is the grid area-average of the local time averaged part of the flow

$$[\phi] = \frac{1}{\tau A} \int_{dA} \int_{t}^{t+\tau} \phi(x,y,t)\, dt\, dA \ , \tag{1b}$$

and $\hat{\phi}$ is the deviation from the grid-averaged part. Here the independent variables x and y refer to position within the grid area, and t refers to a "fast" time for averaging the local flow. This averaging eliminates turbulent fluctuations corresponding to time scales smaller than τ. The grid-averaged flow is constant in terms of these independent variables, but of course varies on larger space and time scales.

In order to apply existing formulations for the surface fluxes, the subgrid-scale flow must be partitioned into a local time-averaged part $\phi^*(x,y)$ and fluctuations from this time average $\phi'(x,y,t)$ so that

$$\hat{\phi}(x,y,t) \equiv \phi^*(x,y) + \phi'(x,y,t) \tag{1c}$$

where

$$\phi^*(x,y) \equiv \frac{1}{\tau} \int_{t}^{t+\tau} \phi(x,y,t)\, dt - [\phi] \ . \tag{1d}$$

The part ϕ' is usually referred to as turbulent fluctuations although in practice ϕ' includes all motions whose time scales are smaller than the

averaging time τ. Existing formulations for the surface fluxes are based on fluxes estimated from observations which use averaging times typically between ten and thirty minutes. The flow component ϕ^* includes all motions on spatial scales larger than the "turbulent" scale (time scale τ) and smaller than the scale of the resolved flow. In global models with grid resolutions of 100 km or more, ϕ^* includes mesoscale motions. The particular partitioning of the flow selected above is not the only possibility but provides a useful framework for identifying the important grid-averaging problems.

The expression for the grid averaged surface flux using the above decompositions becomes

$$[w\phi] = [w][\phi] + [w^*\phi^*] + [w'\phi'] + \big[[w]\phi^*\big] + \big[w^*[\phi]\big] + \big[[w]\phi'\big] + \big[w'[\phi]\big] + [w^*\phi'] + [w'\phi^*]$$

The last six terms on the right-hand side are cross terms which vanish for simple unweighted time and space averaging; that is, [w] can be pulled outside the space and time integrals defining the operator [ ], w^* can be pulled outside the time integral, the areal integral of w^* vanishes and the time integral of w' vanishes. With weighted averaging such as filtering, the cross terms would not normally vanish (e.g., Charnock, 1957). With simple unweighted averaging, the expression for the grid-averaged surface flux simplifies to

$$[w\phi] = [w][\phi] + [w^*\phi^*] + [w'\phi'] \qquad (2)$$

The term $[w][\phi]$ is the resolved flux which is usually converted to advection format by applying incompressible mass continuity to the divergence of the flux. The term $[w^*\phi^*]$ represents the vertical flux due to the time-averaged flow which varies spatially within the grid area. Near the surface, w^* is

normally small except in terrain-related flows. Higher in the boundary layer, the transport term $[w^*\phi^*]$ can be large partly because the spatial (wavenumber) energy gap between the turbulent scales included in ϕ' and the resolved flow, $[w]$, often disappears. The subgrid-scale flux $[w^*\phi^*]$ is so situation dependent, there is no practical way to parameterize it in terms of the resolved flow. As a result, sophisticated formulations for the remaining flux are not justified for use in large-scale models.

To apply existing relationships for the turbulent surface fluxes in familiar form, we symbolize the time-averaging operator with an overbar and using (1d) define the total, local, time-averaged flow as

$$\bar{\phi}(x,y) \equiv \frac{1}{\tau} \int_{t}^{t+\tau} \phi(x,y,t)\, dt = [\phi] + \phi^*(x,y) \quad .$$

It will also be useful to express $[w'\phi']$ as

$$\frac{1}{\tau A} \int_{dA} \int_{t}^{t+\tau} w'\phi'\, dt\, dA = \frac{1}{A} \int_{dA} \overline{w'\phi'}\, dA = [\overline{w'\phi'}] \quad .$$

The use of the overbar is redundant but poses the grid-averaging problem in terms of the usual local operators.

With these expressions, we can now relate the surface turbulent flux to the local time-averaged flow using the usual bulk aerodynamic relationships for surface fluxes. The basic problem for numerical models is that such existing formulations relate the local turbulent flux to the local vertical gradient. In numerical models it has been necessary to use the identical relationship for relating the grid-averaged flux to the vertical gradient of the grid-averaged (resolved) flow even though there is no justification for such use. Except for the exploratory study of Sud and Smith (1984), there are no existing formulations for relating the area-averaged flux to the flow

gradients resolved by the model. The following analyses will show that the difference between the local flux-gradient relationship and the grid-averaged one is more than a mathematical subtlety.

Although it is not possible to construct a relationship for $[w^*\phi^*]$, it is possible to examine plausible behavior of the area average of the flux due to the "turbulence" $[\overline{w'\phi'}]$. For example, consider the local surface flux formulated with the bulk aerodynamic relationship, which in present notation is of the form

$$(\overline{w'\phi'})_{sfc} = \overline{C_\phi}\ \bar{V}(\bar{\phi}_{sfc} - \bar{\phi})$$

or, in terms of the model resolved flow

$$(\overline{w'\phi'})_{sfc} = ([C_\phi] + C_\phi^*)([V] + V^*)\{([\phi_{sfc}] + \phi^*_{sfc}) - ([\phi] + \phi^*)\} \qquad (3)$$

where "sfc" refers to the surface value while other variables are defined with respect to the lowest atmospheric level, C_ϕ is the surface exchange coefficient, V is the surface wind speed, and ϕ represents the transported quantity such as heat, moisture or momentum. The surface exchange coefficient depends on the choice of the atmospheric level, such as 10 m or 50 m, and is especially sensitive to the stability of the flow. The validity of this relationship (3) in evolving boundary layers is discussed in the next section.

Spatially averaging the surface flux relationship over the grid volume, we obtain

$$[(\overline{w'\phi'})_{sfc}] = [C_\phi][V]([\phi_{sfc}] - [\phi]) + [C_\phi^* V^*]([\phi_{sfc}] - [\phi])$$

$$+ [C_\phi][V^*(\phi^*_{sfc} - \phi^*)] + [V][C_\phi^*(\phi^*_{sfc} - \phi^*)] + [C_\phi^*\ V^*\{\phi^*_{sfc} - \phi^*\}] \qquad (4)$$

where, again, only area-averaged variables are resolved by numerical models. Substitution of this expression into (2) then defines the total vertical flux

of ϕ within a grid box. However, only the first term in (2) can be computed in modeling studies and then only with the additional approximation that the spatially averaged exchange coefficient is related to that stability evaluated from spatially-averaged variables. Formally,

$$[C_\phi] = \frac{1}{A} \int \bar{C}_\phi(S, z_0)\, dA \tag{5}$$

whereas numerical models can evaluate only

$$\tilde{C}_\phi(\tilde{S}, [z_0]) \tag{6}$$

where S is the stability parameter and z_0 is the surface roughness parameter; dependencies on the boundary-layer depth and thermal wind are not considered here. The tilde signifies that the function is computed from variables that are already averaged over the entire grid box as opposed to averaging the function itself. Sud and Smith (1984) have examined the behavior of the area average of the surface exchange coefficient of Deardorff (1972) for a special case where the wind speed and roughness was constant over the grid area and the subgrid variation of vertical temperature gradient obeyed a Gaussian distribution. In their case, $[C_\phi] = \tilde{C}_\phi$. Except for their study, the dependence of $[C_\phi]$ on stability has received little formal attention.

In summary, the formulation of subgrid fluxes in a numerical model suffer three types of errors: a) omission of the subgrid flux $[w^*\phi^*]$, b) omission of the various interaction terms in the expression for the averaged surface flux (4), and c) approximation of $[C_\phi]$ in terms of area-averaged variables instead of area-averaging the exchange coefficient. Analogous averaging problems occur with formulation of fluxes at model levels above the surface. In the next section, we examine the spatial averaging of the surface exchange coefficient.

3. Area-Averaged Exchange Coefficient

The area-averaged exchange coefficient may be quite different from the exchange coefficient computed from the stability parameter based on area-averaged variables. This is because the turbulence and exchange coefficient depend on the stability in a nonlinear way. As one example, consider the case where the area-averaged stratification is stable but varies within the grid area. The exchange coefficient predicted by the area-averaged stability may be quite small in stable conditions. However due to the strong nonlinearity of the stability dependence, the area-average of the local exchange coefficient may be significantly larger due to subgrid areas where the stratification is near-neutral or unstable. In these subgrid areas, the local exchange coefficient may be one or more orders of magnitude larger than implied by the spatially averaged stability. Because of the nonlinear dependence of the exchange coefficient on stability, small subgrid regions could have a strong influence on the grid-averaged exchange coefficient and flux but little influence on the grid-averaged stability.

(a) Relationship for exchange coefficient

To illustrate such averaging problems, we will adopt the formulation of Louis (1979) for the exchange coefficient for heat. This formulation closely approximates similarity theory but is considerably simpler and, consequently, has found considerable use in large scale models. The exact form of the relationship for the exchange coefficient is not too important provided that it includes the rapid decrease of the exchange coefficient with increasing stability which occurs at near-neutral values of stability. The behavior of the exchange coefficient at strong stability is quite uncertain partly due to flux sampling problems such as those discussed by Wyngaard (1973). The

ability to assign roughness values and the occurrence of nonequilibrium conditions over realistic surfaces also reduces the importance of the details of the exchange relationship.

The Louis formulation relates the surface exchange coefficient to the surface bulk Richardson number[1]

$$Ri = \frac{g}{\theta_0} [\bar{\theta}(z) - \bar{\theta}_{sfc}] \, z/(\bar{V}(z))^2 \qquad (7)$$

where $\bar{\theta}_{sfc}$ is the potential temperature corresponding to the surface temperature, z is the height of the first model level above ground and θ_0 is a basic state temperature scale. The dependence of the Louis excnange coefficient is plotted in Figure 1 for three different values of z/z_0. The rapid variation of the coefficient at near-neutral stability will dominate the averaging effects.

(b) Spatial variation and adjustment

The surface exchange coefficient varies primarily due to interrelated spatial changes of surface temperature, wind speed and surface roughness. Many land surfaces experience continuous changes of surface characteristics whereas previous studies have concentrated primarily on discontinuities of surface properties. Previous studies have also largely neglected variations of surface evapotranspiration which can occur over surfaces which otherwise appear to be homogeneous. This inhomogeniety is forced by variations of vegetation and variations of soil moisture. Soil moisture variations are forced by spatial changes of soil type and small scale precipitation

---

[1] Although the Richardson number approaches infinity with free convection, the dependence of the Louis exchange coefficient on the Richardson number is such that the predicted heat flux remains well behaved in the free convection limit.

patterns. Such inhomogeneity can force significant spatial variations of surface heat flux, atmospheric stability and boundary layer development (Ookouchi et al., 1984; Pan and Mahrt, 1987). As a result, all surfaces are potentially inhomogeneous and the problem of adjustment to surface inhomogeneity must be considered before applying existing flux-gradient relationships.

Existing formulations for surface fluxes invoke a form of the flux-gradient relationship; nonequilibrium formulations do not exist. Even though the fluxes and other boundary layer characteristics may change rapidly downstream from a change of surface properties, existing models assume that a local equilibrium is maintained betweeen the local surface flux and the local vertical gradient. For example in studies of neutral flow over a discontinuity of surface roughness, the flux-gradient relationship is assumed in the form of the logarithmic relationship as the lower boundary condition (Peterson, 1969; Panchev et al., 1971; Rao et al., 1974; and others).

Observational studies of flow over changes of surface heating and roughness have normally concentrated on the horizontal variation of the depth of the internal boundary layer. Little attention has been devoted to the degree of internal equilibrium between surface fluxes and local vertical gradients. Some studies of internal boundary layers generated by onshore flow have shown that turbulence statistics at relatively short distances from the shore show considerable agreement with similarity relationships based on observations over homogeneous terrain. Such similarity describes much of the data collected by Smedman and Högström (1983) 1500 m from the shore in weakly heated onshore flow. In a study of sea breeze flow 2 km inland, Mizuno (1982) also found turbulence statistics to be described by local similarity theory, although the depth of the internal boundary layer exerted a greater influence

compared to observations over homogeneous terrain. The local equilibrium implied by the success of similarity theory was argued by Mizuno in terms of small values of the turbulent adjustment time scale compared to the Langrangian time scale of the mean flow between the coast and observation point.

For example the adjustment length scale for turbulence equilibrium can be posed as

$$L = U\ \ell/u$$

where ℓ is the length scale of the main eddies, probably some fraction of the depth of the internal boundary layer, u is the turbulence velocity scale which can be estimated as the square root of the turbulence kinetic energy and U is a scale value for the speed of the mean flow. For plausible values of ℓ=100 m, u=1 m/s, and U=5 m/s, the adjustment length scale is 500 m. For this particular example, the transition region where equilibrium conditions are not approximately valid, would be narrow compared to the grid width of most larger scale models. However it is not known how to apply this information to surfaces with continuous changes of surface conditions. Surface features which are smaller scale than the main tranporting motions in the boundary layer will probably not exert an important influence on the overall boundary layer flux. The influence of such surface variations will be integrated by the main boundary-layer eddies.

While it is not possible to consider realistic surfaces where distinct internal boundary layers are often prevented by complex continuous changes of surface conditions, it is necessary that the idealized subgrid variations are consistent with the application of the local flux-gradient approximation. More specifically it must be assumed that changes in surface conditions are

either sufficiently gradual that the flux-gradient relationship remains a useful approximation or that nonequilibrium regions occupy a small fraction of the grid area. Then the bulk aerodynamic relationship is a useful approximation if one can account for subgrid variations of the exchange coefficient due to horizontal variations of stability, roughness, and boundary layer depth. Here we address the variations of the exchange coefficient due to variations of stability which appears to be the most important influence.

(c) Distribution and averaging

Variations within a given grid area depend on geograpnic location, time of day, season, and synoptic situation. It is not possible nor practical to explicitly consider such variations in large scale models. Here we consider the probability distribution of a generic grid box. A Gaussian probability density of the Richardson number is suitable for demonstrating the potential importance of averaging errors.

Employing the Gaussian distribution as in Sud and Smith (1985), the averaged exchange coefficient becomes

$$[C_H] = \frac{1}{A} \int \bar{C}_H(Ri)dA = \int \bar{C}_H(Ri)\ f(Ri)dRi \qquad (8)$$

where f(Ri) is the assumed Gaussian probability density of the Richardson number over area A where Ri (7) is defined in terms of local time-averaged variables. Relationship (8) assumes nothing about the spatial coherence or pattern of the Richardson number but assumes that the overall distribution is Gaussian. The integral on the right-hand-side of (8) was evaluated using Simpson's rule. It was found that using a step size of $.1\sigma$ over a range of $\pm 8\sigma$ provided accurate results in that additional widening of the range or shortening the step size no longer significantly altered the results.

As an example, Figure 1 shows the area-averaged surface exchange coefficient for a Gaussian distribution of the Richardson number with unity standard deviation and zero mean. The variation of the Richardson number together with the nonlinear dependence of the exchange coefficient cause the spatially averaged exchange coefficient to be significantly larger for stable conditions compared to the values for the original local relationship. In other words, when the area-averaged Richardson number is stable, the spatially averaged exchange coefficient may be dominated by the small part of the area corresponding to the unstable tail of the frequency distribution. In the sub-areas of near neutral or unstable stratification, the exchange coefficient is much larger than in stable areas and therefore has an important influence on the area-averaged value even if most of the area is stable.

The influence of averaging is minimal for near-neutral average stability where the dependence of the exchange coefficient on the Richardson number is characterized by an inflection point. The averaging influence on the exchange coefficient is percentage-wise small for large instability where the dependence of the exchange coefficient on the Richardson number becomes more linear. Considering the uncertainty of the original formulation for the exchange coefficient, the influence of averaging for the above conditions is probably important only for the stable case.

The enhancement of the exchange coefficient for stable conditions is even greater with larger standard deviation of the Richardson number since larger standard deviation implies that a greater portion of the area will be near neutral or unstable. This is indicated in Figure 2, where the area-averaged exchange coefficient is shown for different values of the standard deviation.

When the standard deviation of the Richardson number exceeds about 1/2, the averaging effect begins to completely change the behavior of the exchange

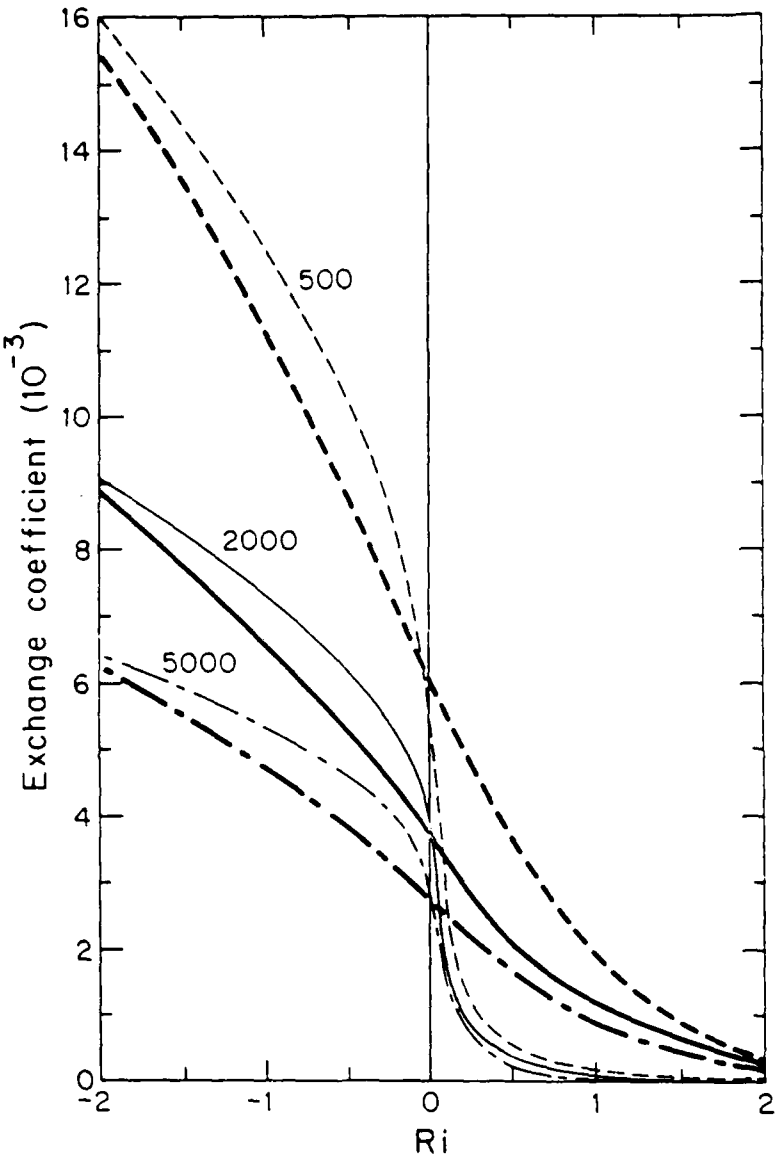

Figure 1. Dependence of the averaged exchange coefficient on the averaged Richardson number for three different values of z/z_0 for standard deviation of the Richardson number equal to one (thick lines) and the original unaveraged exchange coefficient (thin lines).

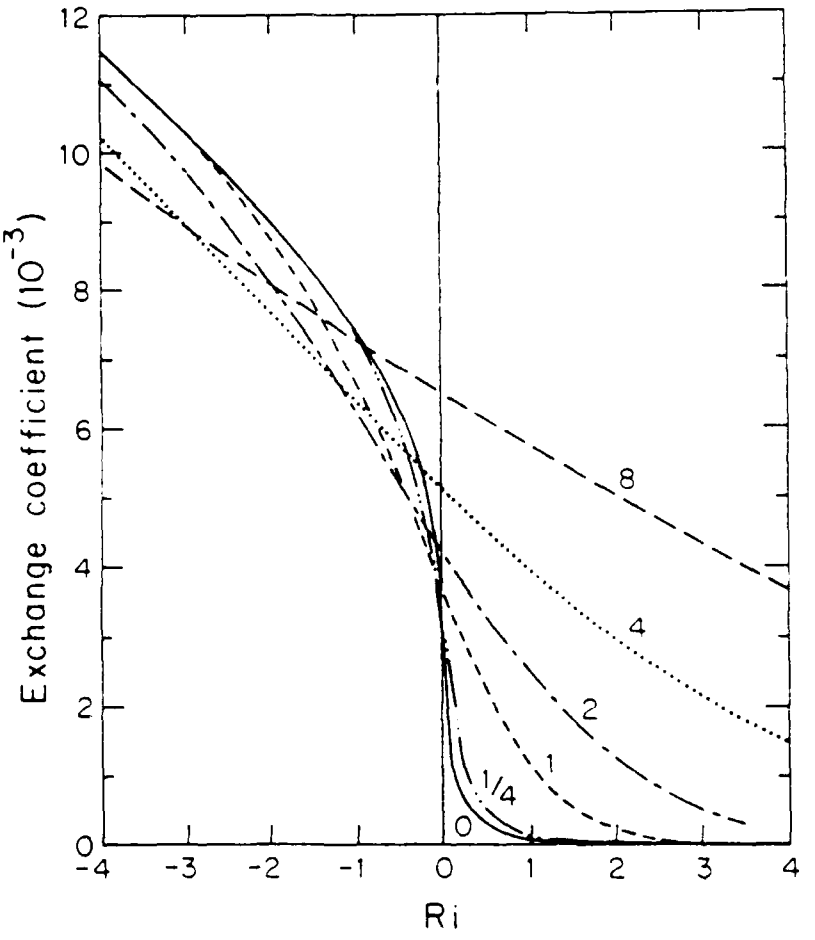

Figure 2. Dependence of the averaged exchange coefficient on the standard deviation of the Richardson number for z/z_0 = 2000.

coefficient. This change is partly due to extreme values at deviations greater than one or two standard deviations toward the unstable regime. When the standard deviation of the Richardson number becomes very large, say greater than five, the dependence of the averaged exchange coefficient on the averaged Richardson number becomes almost linear and the rapid change of the exchange coefficient at near-neutral stability disappears.

The averaging effect could be even greater with significant skewness of the distribution of the Richardson number. However, typical distributions of the Richardson number over a given land area are not known. In the next section, limited information on frequency distributions of the Richardson number is computed from data collected with low-flying aircraft.

4. Observations

We have computed the Richardson number from data collected with low-flying aircraft in the stable nocturnal boundary layer over gently undulating terrain in south central Oklahoma, USA, during quiet periods of the Severe Environmental Storms and Mesoscale Experiment (SESAME). The aircraft instrumentation is described in Mahrt (1985) and Wyngaard et al. (1978).

The Richardson number is computed between the aircraft level and the surface. The surface temperature is estimated from the radiation temperature inferred from the downward pointing radiometer mounted on the aircraft. The estimated error of the surface temperature is thought to be small compared to the temperature difference except for near-neutral conditions. Errors due to the assumption of unity surface emissivity are partially cancelled by the surface reflection of downward longwave radiation. More importantly, the difference between the surface land temperature and the air temperature at $z = z_0$ must be neglected, as in most modeling situations. Such differences may be several degrees with strong cooling or heating.

The surface-based layer Richardson number in analogy with (7) is

$$Ri = \frac{(g/\theta_0)(\bar{\theta}-\bar{\theta}_{rad})z}{\bar{V}^2} \qquad (9)$$

where the potential temperature θ and wind speed V are averaged over segments of the aircraft record and θ_{rad} is the potential temperature corresponding to the surface radiation temperature. The level z of the horizontal flights ranges between 20 m and 100 m for the various legs.

To estimate the "local" average $\bar{\phi}$ in lieu of a time average, the record is divided into 75 m segments (20 observational points) and the Richardson number was computed from variables averaged for each segment. This estimate is useful if the grid width of the intended model is large compared to 75 m. With increased averaging length, the standard deviation of this Richardson number for a given flight leg decreases but the relationship between the Richardson number, its standard deviation and the turbulence intensity does not change appreciably for the data analyzed here.

Statistics for the spatial distribution of the Richardson number were computed for each of the 37 aircraft legs which were typically 15-30 km long. The standard deviation of the Richardson number within a given flight leg increases significantly with increasing stability of the leg (Figure 3a). As a result of this variability, some subregions of weak stability and significant turbulence are possible even when the averaged stability is large. As a further consequence, the turbulence and turbulence flux are unlikely to vanish even with large averaged stability. Note that in Figure 3a, the standard deviation is plotted as a function of the mean of the Richardson numbers computed along the flight leg. This mean Richardson number was generally closely related to the mean Richardson number computed from variables averaged along the leg, although one can imagine realistic situations where this relationship would not hold.

The dependence of the standard deviation of the Richardson number on its mean value does not seem to be sensitive to the aircraft flight level although both the standard deviation and mean value tend to decrease with the height of the aircraft level. This decrease is due to the decrease of stratification with height. The correlation between the mean value and standard deviation of the Richardson number is partly due to the fact that the Richardson number is,

with a few exceptions, bounded by zero since the surface is almost everywhere cooler than the overlying air for this data. As a result, greater standard deviation of the Richardson number leads to greater mean value and vice versa.

The Richardson number computed from the present data is often characterized by skewness towards large positive values although this behavior is too erratic to incorporate into the analysis of Section 3. On one of the days, the wind speed nearly vanishes leading to extremely large positive Richardson numbers which in turn cause the standard deviation and mean value of the Richardson numbers to be "off scale" for Figure 3. This occurred in three of the 37 aircraft legs. This behavior is one of the natural, but unfortunate, characteristics of the Richardson number which can lead to misleading statistics.

Since the standard deviation of the Richardson number increases with stability, the most appropriate averaging for the results reported in Figure 2 would use larger standard deviations at larger Richardson numbers. This has the effect of slowing the decrease of the exchange coefficient with increasing stability as composited over many distributions with different means. The data cannot be used to directly study the relationship between the actual flux and the layer Richardson number. Fluxes computed at the flight level would be contaminated by large sampling problems. Since the fluxes are relatively weak and intermittent under very stable conditions, a much longer record over relatively homogeneous terrain would be needed.

However, it was possible to compute the variance of the vertical velocity as an indicator of turbulence strength for each record segment. The variance is less sensitive to sampling problems. The variance computed for each 75 m segment is undoubtedly due almost exclusively to small scale turbulence with little influence of gravity waves. The variances were then further averaged

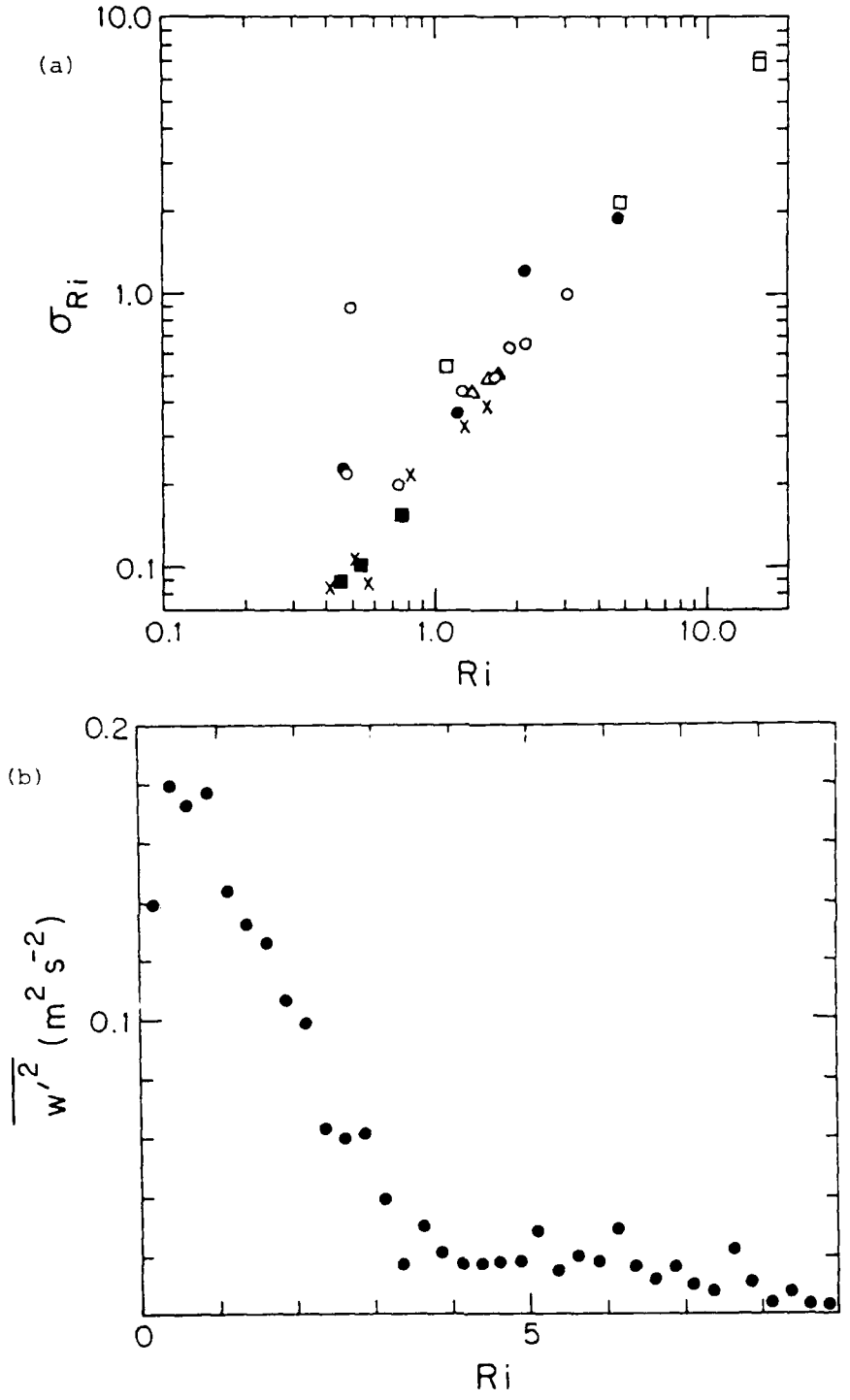

Figure 3. (a) Standard deviation of the Richardson number for each aircraft leg as a function of the leg-averaged Richardson number for the evening of 4 May 1979 (open circles), early morning of 5 May (squares), evening of 5 May (triangles), early morning of 6 May (solid circles), early morning of 7 May (crosses), and early morning of 9 May (solid squares). (b) Composited vertical velocity variance as a function of the Richardson number.

for different stabilityclasses based on the value of the Richardson number; each class corresponds to a Richardson number interval of 0.25.

The dependence of the vertical velocity variance on the stability suggests three distinct regimes (Fig. 3b). For weak stability (Ri < 1), the strength of the turbulence does not appear to be sensitive to the value of the Richardson number although the class, 0 < Ri < 0.25, contains fewer cases and may be subject to inadequate sampling. With moderate stability (1 < Ri < 3), the turbulence decreases linearly with increasing stability. In the very stable case (Ri > 3), the turbulence is quite weak and not very sensitive to the strength of the stability. Apparently, when the turbulence is sufficiently suppressed by the stratification, some residual weak turbulence remains regardless of the strength of the stability. Presumably, this weak turbulence occurs on scales smaller than that used to compute the Richardson number although the nature of motion was not studied.

The critical values of the Richardson number corresponding to the transitions, and the existence of the sharp transitions themselves may depend upon the way in which the Richardson number is defined. It must be noted that the Richardson number used here is a layer Richardson number in contrast to the local gradient Richardson number where the turbulence is thought to be suppressed for values greater than about 0.25.

For the present data, the transition values did not depend on the choice of averaging length used to define the local average. Using only the lowest aircraft levels (20-35 m), the transitions are sharper and shifted toward slightly smaller values of the Richardson number. With higher flight levels, the transitions are less defined and shifted to significantly larger values of the Richardson number. That is, with stable stratification, the turbulence at higher levels becomes more determined by conditions at that level and less

related to surface processes. Furthermore, Richardson numbers computed over thicker layers may be large but still allow for turbulence in thinner sublayers.

Although the relationship between the turbulence variance and the stability depends on the way in which the Richardson number is computed, the above turbulence-stability regimes are similar to those found by Kondo et al. (1978, Fig. 6). The main difference is that in the study of Kondo et al. (1978) the transition to the very stable regime of weak turbulence occurs at smaller Richardson numbers. This is probably related to the fact that in their study, the Richardson number was computed over thinner layers.

In conclusion, the surface-based Richardson number is a useful indicator of turbulence strength in spite of the fact that the Richardson number varies dramatically at low wind speeds. More sophisticated formulations of the averaging problem (8) might take advantage of the well defined relationship between the mean value and standard deviation of the Richardson number. Even though the above data includes different synoptic conditions, the relationship between the turbulence and the Richardson number should be evaluated over other types of land surfaces.

5. Model Evaluation

As an example of the behavior of the flux terms due to subgrid spatial correlations, we have iterated the three-dimensional, four layer, mesoscale model of Han et al. (1982) (see also Deardorff et al., 1984) for an idealized diurnal cycle.

The entire mesoscale model is viewed as one grid box of a larger scale model so that $[\phi]$ is the average value over the entire mesoscale model, $\bar{\phi}$ is the local time-average evaluated at each grid point and ϕ' is the parameterized "turbulence". The surface turbulent transport is again formulated with the Louis relationship for the surface exchange coefficient. The model includes some surface terrain variations which lead to nocturnal drainage of cold air for cloudless cases of weak ambient flow. In the prototype numerical experiment, the incoming solar radiation varies diurnally leading to a surface heat flux which reaches a daytime maximum of about .2 K m s^{-1}. The geostrophic wind is specified to be constant with a nominal speed of .1 m s^{-1} to simulate conditions approaching free convection.

For the unstable daytime case, all of the spacial correlation terms in the expression for the grid-averaged flux (4) are small except for the contribution due to spatial correlation between the exchange coefficient and the surface wind speed (second term in Eq. 4). This term acts to reduce the total grid-averaged heat flux ($[C_H^* V^*]<0$), in this case by 30-40% (Figure 4a). In other words, where the wind speed is stronger, the instability tends to be significantly less so that the exchange coefficient is significantly smaller.

However, the error due to the neglect of subgrid correlations between wind speed and the exchange coefficient is largely compensated by underestimation of the area-averaged exchange coefficient (Figure 4b) which appears in the main contribution to the grid area-averaged heat flux (first term in

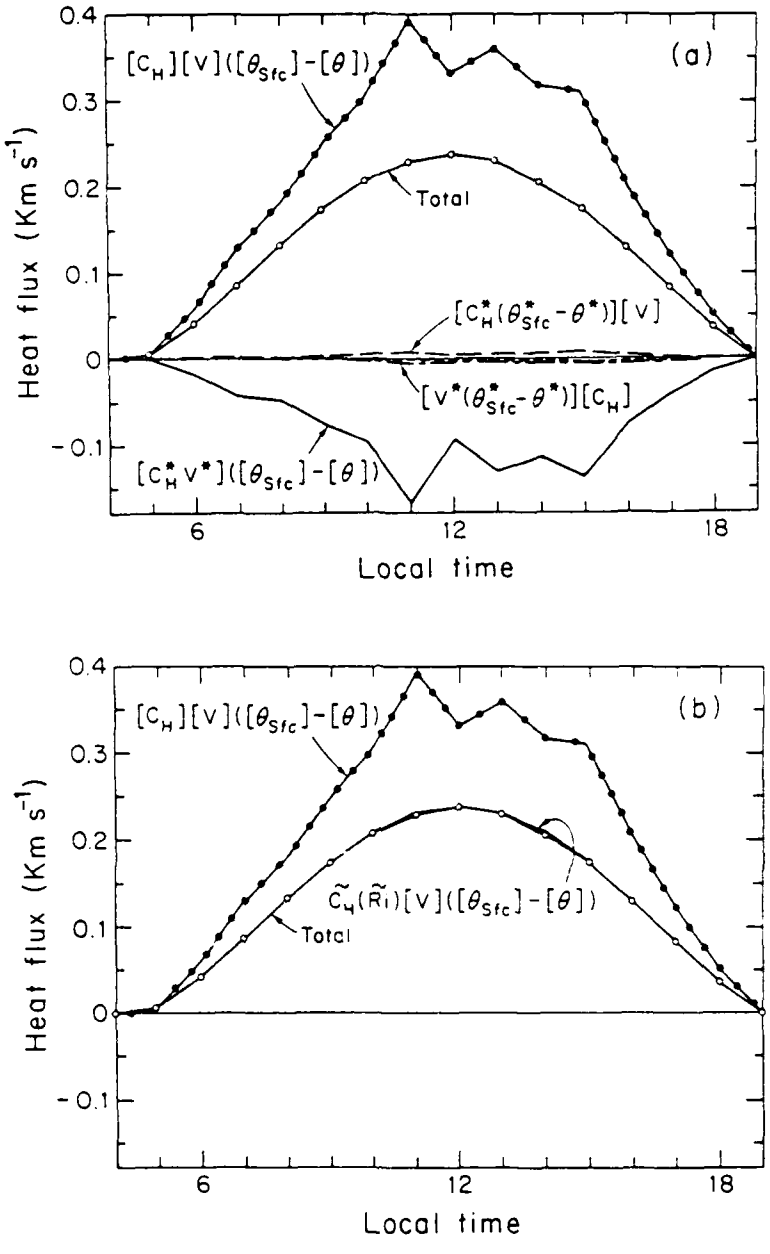

Figure 4. (a) Various contributions to the grid-area surface heat flux (see Eq. 4) for the daytime period. The triple correlation term is negligible. (b) The total heat flux computed from Eq. 4 (open circles) as compared to the flux computed from area-averaged variables and area-averaged exchange coefficient (solid circles) and the flux corresponding to the "model available" exchange coefficient computed from Ri (solid line with no circles; essentially coincides with line with open circles for this case).

Eq. 4). As a result, the model-estimated flux is close to the true grid-averaged flux. Recall that the large scale model can evaluate the exchange coefficient only in terms of the Richardson number based on grid area-averaged variables (6). That is, the exchange coefficient in the large scale model must be computed as

$$\tilde{C}_H = f(\tilde{Ri}) \qquad (10)$$

$$\tilde{Ri} = (g/\theta_0)([\theta]-[\theta_{sfc}])z/[V]^2$$

where f is the function for the dependence of the exchange coefficient on stability. Compared to $\tilde{C}_H$, the true area-average of the exchange coefficient $[C_H]$ is augmented by especially large values occurring at "hot spots" where the instability is enhanced due to larger vertical gradients of temperature and/or weaker winds. The near-cancellation of the important spatial correlation term with errors due to the underestimation of $[C_H]$ can be shown to occur with the Louis expression for the conditions $-Ri > 10$ and $[\theta^{1/2}] \approx [\theta]^{1/2}$.

During the transitions between stable and unstable periods, the bulk aerodynamic relationship in the large scale model can easily predict the wrong sign of the grid area-averaged heat flux as occurs in Figure 5b. This averaging problem results from the importance of subgrid correlations between the exchange coefficient and the temperature gradient (fourth term in Eq. 4). Large upward heat flux in regions where the vertical temperature gradient is unstable dominates the grid area-averaged heat flux even though the grid average of the vertical temperature gradient corresponds to stable stratification. This "countergradient" heat flux results from the fact that the exchange coefficient is much larger in the small part of the grid area which

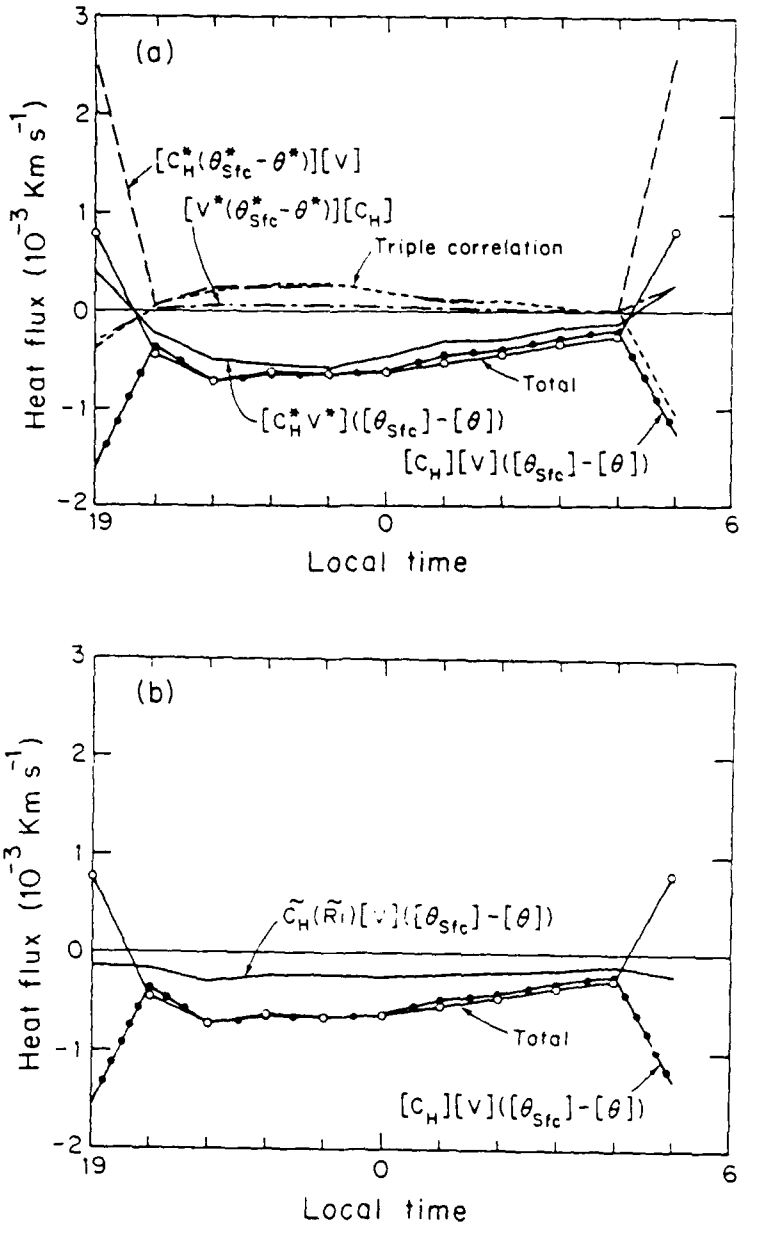

Figure 5. (a) Various contributions to the grid-area surface heat flux for the nocturnal period. (b) The total heat flux computed from Eq. 4 (open circles) as compared to the flux computed from area-averaged variables and area-averaged exchange coefficient (solid circles) and the flux corresponding to the "model available" exchange coefficient computed from Ri (solid line with no circles). For comparison with Fig. 4, note the factor of 10^3 scale shift for the ordinate.

is unstably stratified. This particular averaging problem appears to be rather short-lived with diurnally varying flow. However, such an effect could exert a longer term influence in situations which are persistently characterized by near neutral stratification. This averaging problem is somewhat analogous to the countergradient heat flux resulting from time-averaging the vertical temperature gradient in the interior of the heated boundary layer (Deardorff, 1966) or time iteration which excludes diurnal variations (Mahrt et al., 1986).

For the strongly stratified, nocturnal, situation, the relative importance of the various subgrid correlation terms (Figure 5a) is quite different from the unstable case. Now the wind speed and the exchange coefficient are positively correlated, leading to enhancement of the downward heat flux. That is, the stability is locally reduced in regions of strongest airflow which increases the exchange coefficient.

This increase of the grid-averaged heat flux is opposed by the negative correlation between spatial variations of the exchange coefficient and the vertical gradient of potential temperature. The exchange coefficient is small where the vertical gradient of potential temperature is large. The grid-averaged heat flux is also reduced by the triple correlation term (last term in Eq. 4) which is physically quite complex.

The spatial correlation terms in (4) sum to near zero for the stable case so that the net modification of the area-averaged heat flux due to the subgrid correlation terms is small. That is, the total flux is close to that predicted by the main contribution to the area-averaged heat flux (first term in Eq. 4). However this main term is underestimated by models due to the fact that the exchange coefficient $\tilde{C}_H$, which is based on the Richardson number computed from area-averaged variables, is considerably smaller than the

true area-averaged exchange coefficient [C_H] (Figure 5b). This underestimation of the downward heat flux would be expected to lead to modelled surface temperatures which are too cold.

These results are for the case of strong radiational cooling at the surface. If the geostrophic wind speed is increased, subgrid variations are reduced. For winds on the order of 10 m s^{-1}, the averaging problems have become negligibly small at least based on the numerical experiments with the mesoscale model used in this study. The generality of these results is not known and Figures 4-5 must be considered only as examples of potential averaging problems.

The transport by subgrid scale motions associated with local topography is not explicitly reported here because it involves correlations between temperature and downslope flow. The bulk aerodynamic relationship describes heat flux perpendicular to the local ground. In an absolute coordinate system where the vertical coordinate is parallel to the gravity vector and independent of local slope, downslope currents lead to an upward heat flux. Such a heat transport redistributes heat in response to cooling over sloped terrain. Since such differential heating is not included in numerical models on subgrid scales, the inclusion of such redistribution of heat would appear to be not appropriate. The same could be said of the influence of heat transport by daytime upslope currents. However, secondary effects could be important particularly if the upslope currents initiate moist convection.

The estimation of the area-averaged momentum flux is more difficult because of the influence of the terrain-induced pressure drag. This pressure drag is often incorporated by enhancing the drag coefficient or surface roughness length. However, the practice of using the subsequently enhanced surface friction velocity in the formulations for mixing in the

boundary layer is not justified since the pressure drag of the topography does not translate into boundary layer turbulence or at least not in a way which is described by existing boundary-layer theory.

6. Reformulation

Before reformulating the dependence of the exchange coefficient on the Richardson number, several additional complications must be noted. In theory the turbulence vanishes as the gradient Richardson number exceeds a critical value. In numerical models, this asymptotic possibility should not be invoked, not only because of horizontal averaging problems but also because the Richardson number is computed over a finite depth determined by the model resolution. No matter how large the Richardson number for the grid layer, turbulence in actual atmospheric flows can always be generated over thinner layers where the Richardson number is locally small. The turbulence over such thin layers often occurs intermittently at changing levels so that flux over a deeper layer is established on a time scale which is longer than that of the intermittency.

In addition, momentum can be transported vertically by nonlinear gravity waves while significant vertical transport of heat may be generated by radiational flux divergence, especially with strong surface inversions. Both of these transport mechanisms are generally neglected in large scale boundary-layer models. Because of these influences, and the significant spatial averaging effects in the stable case, any formulation of the surface flux may suffer large errors. For this reason complicated schemes attempting to include the details of the influence of stability are not justified.

Both the idealized analysis in Section 3 and the specific calculations in Section 5 indicate that for the stable case, the exchange coefficient relating area-averaged fluxes to area-averaged gradients should be significantly larger than predicted by the usual expressions for the exchange coefficient. Furthermore, the exchange coefficient should not vanish for large Richardson number as is implied by the observations reported in Section 4 and as

previously recommended by Kondo et al. (1978). The case of unstable stratification does not require systematic modification at least based on the above results, although the flux due to mesoscale subgrid motions could be important.

A slower decrease of the value of the exchange coefficient with increasing positive stability can be most simply formulated as

$$C_H(Ri) = C_{HO} \exp(-mRi) \qquad (11)$$

where C_{HO} is the value at neutral stability as predicted by the Louis formulation. The idealized averaging results in Figure 1 suggest that m is a little greater than one for unity standard deviation of Richardson number. Considering the dependence of the standard deviation on the Richardson number (Section 4) and additional influences which enhance the area-averaged flux in stable conditions (Section 5 and discussions above), m = 1 appears to be a suitable value.

Thus, expression (11) for the stable case and the usual Louis formulation for the unstable case form a tentative model of the surface exchange coefficient which attempts to include the most important qualitative aspects of grid-area averaging. With present lack of understanding, (11) could be applied to the transfer of other quantities in addition to heat. The performance of (11) in a given large scale model would presumably depend on the details of the model, especially the height of the lowest model level. In the model of Troen and Mahrt (1986), relationship (11) applied to heat, momentum, and moisture leads to the expected enhancement of downward fluxes for the very stable cases although realistic representation requires several levels within the thin nocturnal boundary layer. In models which have been indirectly adjusted to compensate for the underestimation of downward heat fluxes and anomalous cooling, the use of (11) may not be beneficial.

7. Conclusions

The formulation of the subgrid scale flux in numerical models commits three types of errors related to the implied spatial averaging of the grid area. First, the flux due to subgrid motions larger than turbulence scales [see Eq. (2)] is not included. We did not examine this problem here since it is strongly dependent on situation. Secondly, extra flux terms result from the spatial averaging of the local flux-gradient relationship [see Eq. (4)]. These terms are due to spatial correlation between the locally averaged variables appearing in the flux-gradient relationship. Thirdly, errors result from necessity of relating the exchange coefficient to resolved grid area-averaged variables instead of spatially averaging the local exchange coefficient as required by the Reynolds averaging. Because these errors can be large, the use of sophisticated local relationships between fluxes and gradients does not appear to be justified for use in large-scale numerical models.

The particular, modeling results of Section 5 indicate that the important spatial correlation term for the unstable case approximately cancels errors due to the use of existing local formulations for the exchange coefficient. For the stable case, the spatial correlation terms approximately cancel each other while the required grid-averaged exchange coefficient is seriously underestimated. This underestimation is due to relatively large values of the exchange coefficient within the parts of the grid area where the stability is weakest. This problem is important because of the strong nonlinearity of the relation between the exchange coefficient and stability. Even though the absolute magnitude of the surface fluxes is small in the stable case, and probably exerts little influence on the overlying free atmosphere, such small fluxes become important in the surface energy balance and significantly

influence the surface air temperature. The convergence of downward turbulent flux of heat occurs over a thin boundary layer in the strongly stratified case and therefore can be locally significant even if the flux magnitude is small. Then use of the usual local flux-gradient relationship and the associated underestimation of the grid-averaged downward heat flux will lead to unrealistically rapid surface cooling.

A revised formulation (11) for the dependence of the exchange coefficient on the Richardson number is constructed for the stable case. The revised formulation is thought to improve significantly the prediction of the grid-area averaged flux. However, any formulation for the stable case remains tentative due to the incomplete understanding of turbulence with stable conditions and due to the lack of observations of spatial variations of surface fluxes.

Observational verification for the stable case is difficult since fluxes are weak and computed fluxes are often seriously contaminated by sampling problems. The observed relationship between small scale vertical velocity variance and the layer Richardson number indicates three distinct regimes as previously found in Kondo et al. (1978), although the values of the Richardson number at the transitions between regimes depend on the depth of the layer for the computation of the Richardson number. For the weakly stratified case ($Ri < 1$), the turbulence variance does not systematically vary with the Richardson number. For the moderately stratified case ($1 < Ri < 3$), the turbulence strength decreases linearly with increasing Richardson number. For strong stability ($Ri > 3$), the turbulence is weak but is not significantly reduced by further increases of the Richardson number. Even with large layer Richardson number, turbulent transport may continue over thinner layers, at

least intermittently. As a result, the exchange coefficient should not totally vanish with large layer Richardson number.

Acknowledgements

The author gratefully acknowledges the computational assistance and comments of Paul Ruscher, Kyozo Ueyoshi, and the helpful comments of Michael Schlesinger. This material is based upon work supported by the Air Force Geophysics Laboratory, Cambridge, MA, under Contract No. F19628-81-K-0046.

References

Charnock, H., 1957: Notes on the specification of atmospheric turbulence. Roy. Statist. Soc. Proc., A120, 398-408.

Deardorff, J.W., 1966: The counter gradient heat flux in the lower atmosphere and in the laboratory. J. Atmos. Sci., 23, 503-506.

Deardorff, J.W., 1972: Parameterization of the planetary boundary layer for use in general circulation models. Mon. Wea. Rev., 100, 93-106.

Deardorff, J.W., K. Ueyoshi, and Y.-J. Han, 1984: Numerical study of terrain-induced mesoscale motions and hydrostatic form drag in heated growing mixed layers. J. Atmos. Sci., 41, 1420-1441.

Han, Y.-J., K. Ueyoshi, and J.W. Deardorff, 1982: Numerical study of terrain-induced mesoscale motions in a mixed layer. J. Atmos. Sci., 39, 2464-2476.

Kondo, J., O. Kanechika, and N. Yusuda, 1978: Heat and momentum transfers under strong stability in the atmospheric surface layer. J. Atmos. Sci., 35, 1012-1021.

Louis, J.-F., 1979: A parameteric model of vertical eddy fluxes in the atmosphere. Boundary-Layer Meteor., 17, 187-202.

Mahrt, L., 1985: Vertical structure and turbulence in the very stable boundary layer. J. Atmos. Sci., 42, 2333-2349.

Mahrt, L., C. Berthou, P. Marquet, and J.-C. André, 1986: Time-averaging the flux-profile relationship. To appear in Annales Geophysicae.

Mizuno, T., 1982: On the similarity of the characteristics of turbulence in an unstable boundary layer. Boundary-Layer Meteor., 23, 69-83.

Ookouchi, Y., M. Segal, R.C. Kessler, and R.A. Pielke, 1984: Evaluation of soil moisture effects on the generation and modification of mesoscale circulations. Mon. Wea. Rev., 112, 2281-2292.

Pan, H.-L., and L. Mahrt, 1987: Interaction between soil hydrology and boundary-layer development. Boundary-Layer Meteor., 38.

Panchev, S., E. Donev, and N. Godev, 1971: Wind profile and vertical motions above an abrupt change in surface roughness and temperature. Boundary-Layer Meteor., 2, 52-63.

Peterson, E.W., 1969: Modification of mean flow and turbulent energy by a change in surface roughness under conditions of neutral stability. Quart. J. Roy. Meteor. Soc., 95, 561-575.

Rao, K.S., J.C. Wyngaard, and O.R. Coté, 1974: The structure of the two-dimensional internal boundary layer over a sudden change of surface roughness. J. Atmos. Sci., 31, 738-746.

Saltzman, B., and S. Ashe, 1976a: The variance of surface temperature due to diurnal and cyclone-scale forcing. Tellus, 28, 307-322.

Saltzman, B., and S. Ashe, 1976b: Parameterization of the monthly mean vertical heat transfer in the earth's surface. Tellus, 28, 323-332.

Smedman, A.-S., and U. Högström, 1983: Turbulent characteristics of a shallow convective internal boundary layer. Boundary-Layer Meteor., 25, 271-287.

Sud, Y.C., and W.E. Smith, 1984: Ensemble formulation of surface fluxes and improvement in evapotranspiration and cloud parameterizations in a GCM. Boundary-Layer Meteor., 29, 185-210.

Sud, Y.C., and W.E. Smith, 1985: The influence of surface roughness of deserts on the July circulation (A numerical study). Boundary-Layer Meteor., 33, 15-49.

Troen, I., and L. Mahrt, 1986: A simple model of the atmospheric boundary-layer; sensitivity to surface evaporation. Submitted to Boundary-Layer Meteorology.

Wyngaard, J.C., 1973: On surface layer turbulence. Ch. 3 Workshop on Micrometeorology, D.A. Haugen, (ed.), Amer. Meteor. Soc., Boston, Mass.

Wyngaard, J.C., 1982: Boundary-layer modeling. Atmospheric Turbulence and Air Pollution Modelling. Edited by F.T.M. Nieuwstadt and H. van Dop, D. Reidel Publishing Co., Dordrecht.

Wyngaard, J.C., W.T. Pennell, D.H. Lenschow, and M.A. LeMone, 1978: The temperature-humidity covariance budget in the convective boundary layer. J. Atmos. Sci., 35, 47-58.

CHAPTER V

PARAMETERIZATION OF THE STABLE BOUNDARY LAYER

1. Introduction

In this study, the planetary boundary layer (PBL) model of Troen and Mahrt (1986; hereafter referred to as TM86) is examined to determine its response to specific parameterization changes. This model is currently used in AFGL's 3-D global spectral model (Brenner *et al.*, 1984; Yang *et al.*, 1988). The modifications discussed below are motivated by examination of other model formulations as well as analysis of aircraft and tower data in the stable boundary layer (SBL). Any model improvements must be weighed against potential increases of computational costs and model complexity.

The parameterization of the very stable boundary layer is an important problem. For example, consider the forecasting problems of minimum temperature and pollution concentrations. Under very stable conditions with clear skies and calm winds at night, the minimum surface temperature can be determined to a large degree on the solution of the surface energy balance (Pan and Mahrt, 1987). With inadequate sensible heat transfer, the amount of nocturnal cooling of the surface can easily be overpredicted. The predicted formation of dew also plays an important role (Oke, 1978).

The more statically stable the lower atmosphere, the greater the potential for serious air pollution episodes. The meteorological conditions which favor serious air stagnations are well-known to be associated with synoptic scale high pressure, when large-scale subsidence acts as a cap to boundary layer growth. The presence of a capping temperature inversion on a statically stable PBL restricts vertical mixing of pollutants. In addition, horizontal advection of pollutants away from their source is not likely near the centers of high pressure systems, where winds are weak. The mechanism which is perhaps most important in this regard is the strength of the turbulence (parameterized through the eddy diffusivity) which can diffuse the pollutants upward from the surface. With inadequate vertical mixing, the model would predict higher concentration values than might be expected.

The main changes studied here involve, firstly, the determination of the height of the PBL under stable conditions, where a critical Richardson number

formulation is used. The second change involves application of a modified exchange coefficient for momentum, heat, and moisture, following Mahrt (1987). The final change, and perhaps the most significant one, involves the reformulation for the eddy diffusivity in the boundary layer for very stable conditions following Kondo *et al.*, (1978). The motivations for considering and ultimately implementing these changes will become apparent separately in each of the following sections.

These examinations involve running the one-dimensional version of the model of TM86, performing separate sensitivity tests of each of the new formulations. Finally, all three changes are included together. Initial conditions for this sensitivity experiment were specified for a 48 hour run, using latitude 20°N, longitude 10°E, 0800 GMT on 21 June. The soil and atmosphere are both taken to be dry, the modelled soil properties are those of sand, the atmospheric lapse rate is 6°C km^{-1} with an initial surface temperature of 20.7°C; the time step used in the model is 180 s and the vertical resolution is 20 m.

The suggested reformulations are described in detail in Section 2. Section 3 presents the results of the sensitivity tests for the initial conditions listed above. In Section 4, other tests of the 1-D model are discussed, including a simulation of conditions during the Wangara field experiment (Clarke *et al.*, 1971) and a winter snow cover situation over Manitoba using a new model package for surface snow cover. Finally, the results are summarized in Section 5.

2. New Formulations

a. *PBL height and the critical Richardson number*

The Richardson number is viewed as the ratio of buoyancy destruction of turbulence to its production by shear, and in gradient form has a theoretical critical value of 0.25, according to many studies over the past fifty years (Panofsky and Dutton, 1984). Recently, however, the value of the critical Richardson number has again come into question. Miles (1987) (whose 1961 contribution had much to do with the instillation of the value $^1/_4$) gives an historical accounting of the Richardson number and its usage and finally suggests, based on recent advances in nonlinear hydrodynamic stability theory (e.g., Abarbanel *et al.*, 1986), a value of $Ri_c = 1$.

The Richardson number may take different forms, but in numerical models the layer Richardson number is the only type which can be used. It is defined as

$$Ri_L = \frac{g\ \Delta z\ \Delta\theta}{\theta_0\ [\Delta U]^2}\ , \tag{1}$$

with θ_o the mean potential temperature of the layer, $\Delta\theta$ the change in potential temperature across the model layer, Δz the thickness of the model layer, and ΔU the change in wind speed over the layer. If the bottom layer is the ground surface, ΔU becomes simply U, Δz becomes z, and Ri_B is called the bulk Richardson number. Because of the sensitivity of Ri to the depth over which gradients are measured, it is generally believed that the true critical Richardson number actually increases as the depth increases (Lyons *et al.*, 1964). In fact, turbulence is often observed, at least on an intermittent basis, for layer Richardson numbers much larger than 0.25. A critical value of 1.0 is often used in applications (Brutsaert, 1982), and this value will be used in the control experiment.

In the present model, the height of the boundary layer for the stable case is determined from

$$h = \frac{Ri_c\ \theta_0\ U^2}{g\ \Delta\theta_v}\ , \tag{2}$$

where h is the boundary layer height, U is the wind speed in the model layer, and $\Delta\theta_v$ is the virtual potential temperature change from the top of the layer to a point near the surface (see TM86), and Ri_c is the critical Richardson number. The determination of h is an iterative procedure, beginning at the surface. At each model level, the bulk Richardson number is calculated and compared to the critical Richardson number. When Ri_B exceeds Ri_c, the boundary layer height is found by a procedure which is illustrated graphically in Fig. 1.

The proposed change to TM86 does not involve the format for determination of h but rather the value of the critical Richardson number. Because of the sensitivity of h to Ri_c, it is important that a critical value be chosen which simulates a realistic transition to suppressed turbulence (for $Ri > Ri_c$). TM86 chose a value of 0.5. It is clear from (2) that any change in Ri_c will force a direct response in the predicted value of h. Observations do support the notion that turbulence continues at layer Ri values well above 1 (e.g., Portman *et al.*, 1962; Webb, 1970; Kondo *et al.*, 1978; Kunkel and Walters, 1982; Louis *et al.*, 1983; Mahrt, 1987). In light of these observations and new theoretical developments, perhaps a value as large as 5 for a critical value of the *bulk* Richardson number may not seem unreasonable. Experiments will be carried out for several values of the critical Richardson number.

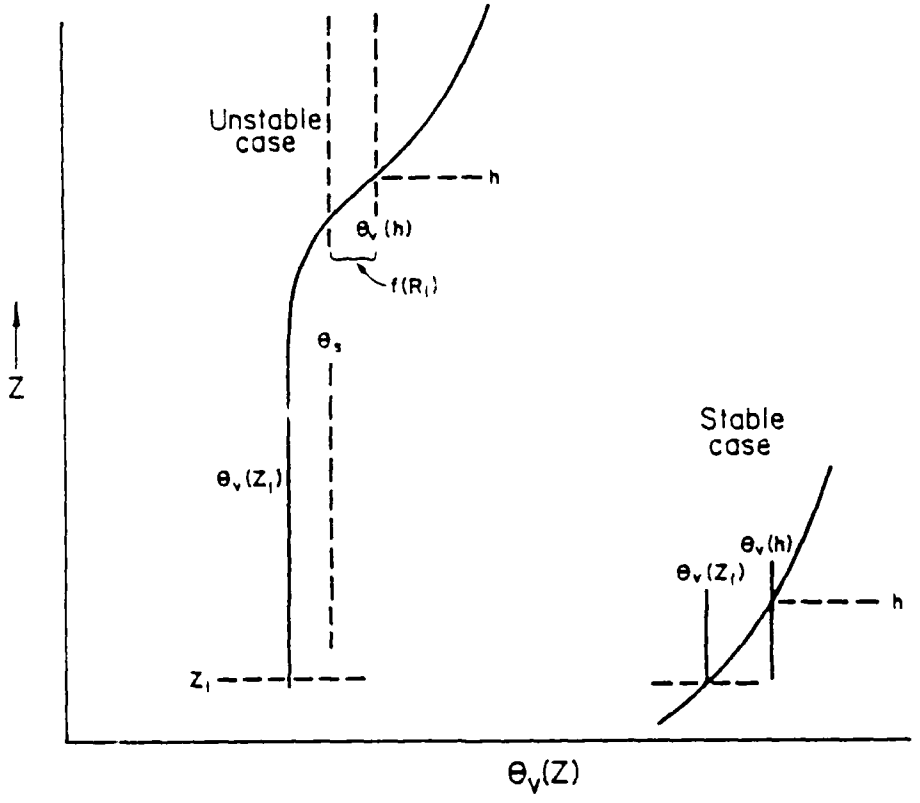

Figure 1. Determination of boundary layer height in the PBL model (Troen and Mahrt, 1986).

b. Surface exchange coefficients

As mentioned earlier, Mahrt (1987) has proposed that a modified exchange coefficient for heat be implemented in atmospheric PBL models. Such a change is motivated because present models underestimate the strength of heat transfer in the very stable case, due to typical subgrid-scale variations of surface conditions. Recently, the European Centre for Medium Range Weather Forecasts (ECMWF) modified the parameterization of surface processes in their operational model (Böttger, 1987), partly motivated in part by exaggerated nocturnal cooling under clear skies. Apparently PBL models often predict surface temperatures which are too cold at night due to erroneous elimination of downward heat flux in the strongly stratified surface inversion layer. Other corrections to compensate for the lack of sensible heat transport under statically stable conditions are sometimes used, or a stable layer may not be permitted to develop, in which case the exchange coefficient for the neutral case is used, ensuring continuation of sensible heat transport.

In TM86, the coefficients of Louis (1979) have been used for momentum, heat, and moisture. Sensitivity tests have been performed to compare this relationship with the one proposed by Mahrt for the stable case, namely

$$C_h = C_{ho}\, e^{-m\, Ri_B}, \qquad (3)$$

where C_h is the calculated heat exchange coefficient, C_{ho} is its value for neutral conditions as calculated in the Louis formulation, and m is an adjustable parameter thought to be about 1.

The heat exchange coefficient will be substantially larger for the Mahrt formulation, as can be seen in comparing Fig. 2a to 2b. Also as m in (3) is decreased, the exchange coefficient decreases more slowly with increasing bulk Richardson number (Fig. 2c). Results from experiments for a few values of the adjustable parameter m will be presented in Section 3. The control run uses the Louis formulation for C_h.

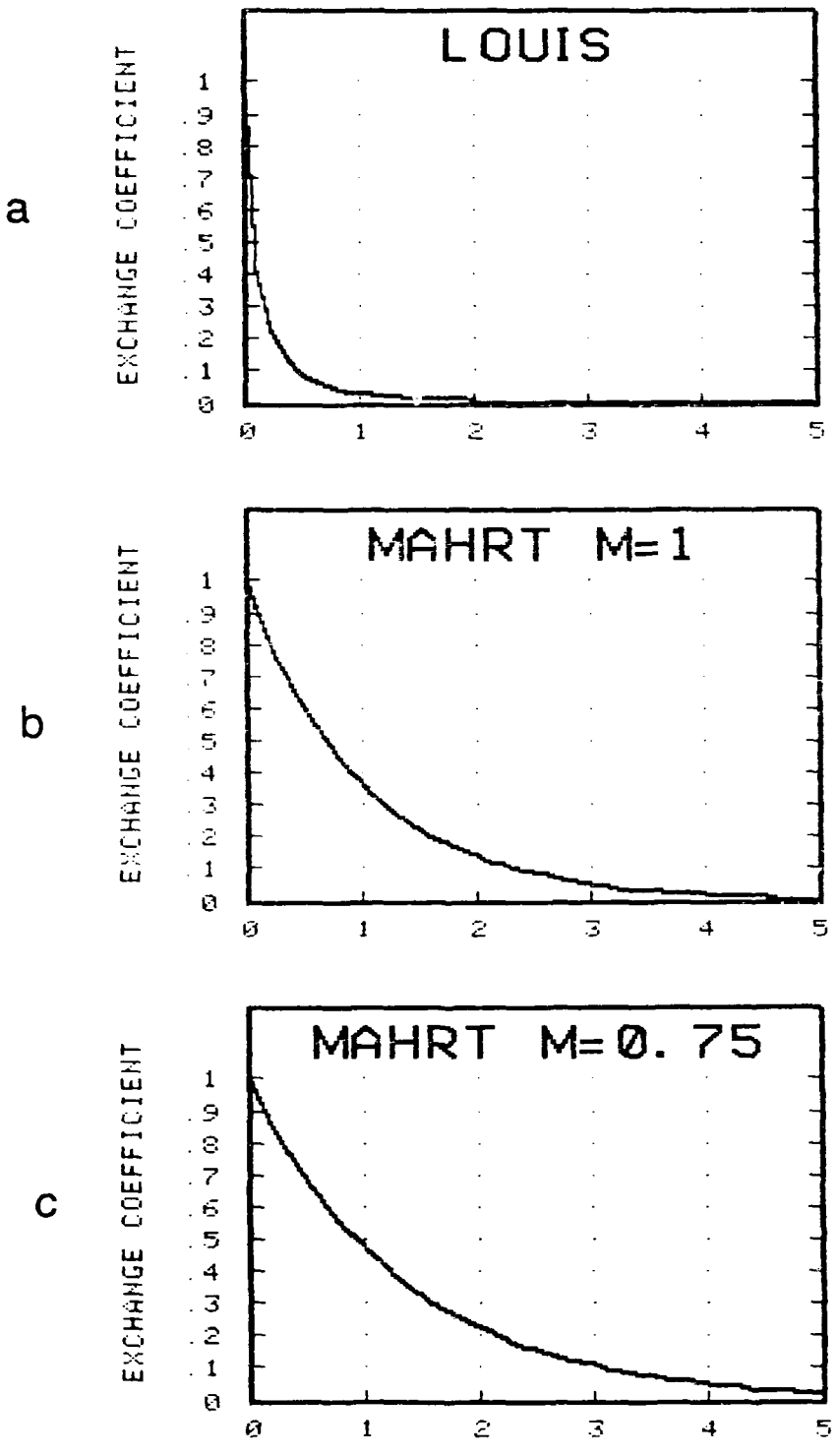

Figure 2. The effect of bulk Richardson number on the surface exchange coefficient. (a) $(1 + 4.7\ Ri_B)^2$, as in Louis (1979). (b) $\exp\{-m\ Ri_B\}$, as in Mahrt (1987); m=1. (c) as in (b) but for m=0.75.

c. *Eddy diffusivity*

Many simple models of the planetary boundary layer parameterize turbulence transport in terms of eddy diffusivities for momentum, K_m, and heat, K_h. Sommeria (1987) recently reviewed simple and complex parameterizations. Simple treatments suffer in the stable case because the turbulence in the so-called outer layer are governed by surface fluxes. Recent work in the stable case supports the notion of local scaling (Nieuwstadt, 1984) and applying a layer-by-layer approach (Lacser and Arya, 1986) to the turbulence parameterization. Such detail cannot be included in large scale models as in the present case.

In the present formulation, the eddy diffusivity for momentum is given as

$$K_m = \frac{u_* k z}{\phi_m}(1 - \frac{z}{h})^p \tag{4}$$

with u_* the surface friction velocity, given by

$$u_* \equiv \sqrt{C_m \overline{|V_H|^2}} \quad , \tag{5}$$

k is von Kármán's constant, taken here to be 0.4, z the model height, ϕ_m the nondimensional shear function, and p=2. This follows the treatment of Brost and Wyngaard (1978). Following Businger *et al.* (1971), the shear function takes the form

$$\phi_m = (1 + 4.7\frac{z}{L}) \tag{6}$$

under stable conditions, where L is the Monin-Obukhov length

$$L \equiv - \frac{u_*^3}{g\, k \left(\overline{w'\theta_v'}\right)_s} \, . \tag{7}$$

Although (6) was intended for use in the surface layer, some PBL models simply use the same form in the parameterization for turbulence in the outer layer as well, with the $(1 - {}^{z}/_{h})$ factor included to allow for gradual decrease of K_m as the top of the boundary layer is approached.

TM86 show that in their model, K_m effectively reduces to

$$K_m = 0.09\ L\ u_* \left(1 - \frac{z}{h}\right)^p , \qquad \frac{z}{L} > 1. \tag{8}$$

On dimensional grounds, the eddy diffusivity can be seen as the product of a velocity and length scale, so that

$$K_m \sim U \quad . \tag{9}$$

Comparing (9) to (8) would seem to indicate L is one of the relevant length scales for turbulent mixing above the surface layer in TM86. However, the Monin-Obukhov length is a valid length scale only in the surface layer according to similarity theory; the surface layer may be only a few meters deep under very stable conditions. In some of our 1-D PBL sensitivity experiments, L is about 1 m, and therefore the surface inversion layer extends well above L. Brutsaert (1982) notes that for $^z/_L > 1$, observations support use of a constant value of ϕ_m, such as that suggested by Kondo *et al.* (1978),

$$\phi_m = 6 \quad . \tag{10}$$

Most recently Lacser and Arya (1986) and Sorbjan (1987) have, in observational and modelling studies, respectively, verified fairly constant vertical profiles of the nondimensional shear functions ϕ_m and ϕ_h.

Since K_m is *inversely* proportional to ϕ_m, a limitation of the maximum value on ϕ_m corresponds to substantially larger diffusivities, increased mixing in the PBL, and a deeper surface inversion layer, compared to TM86 and previous models. This constant ϕ_m formulation incorporates observations which virtually suggests a third regime for boundary layer stability in the model, namely the *very* stable case. This tendency for three regimes of boundary layer stability based on the bulk Richardson number has been noted in observational studies in the past, including Portman *et al.*, (1962), Kondo *et al.*(1978), and Mahrt (1987).

In the changed model studied here, the third regime is enacted if $^z/_L > 1$ in the outer layer. The new eddy diffusivity is adopted here by modifying the nondimensional shear function as alluded to earlier:

$$\phi_m = \begin{cases} (1 - 7\frac{z}{L})^{-1/3} , & L < 0 \\ (1 + 4.7\frac{z}{L}) , & 0 \le \frac{z}{L} \le 1 \\ 5.7 , & \frac{z}{L} > 1 \end{cases} \quad . \qquad (11)$$

d. *Summary of sensitivity studies*

The experiments performed and the parameters changed in the runs are summarized in Table 1; changes are indicated in italics. The three changes should show some improvement if incorporated into TM86 separately, but we might expect the results to be best if they are all coupled in one run. This makes sense in view of the results of Ruscher (1987) and other observational studies which have shown that although the large eddies in the SBL are important features of the flow, they do not contribute much to the overall mixing which is occurring. This mixing appears to be concentrated at the edges of the eddies. Such a small-scale feature cannot be adequately resolved in a global model, so horizontal averaging is implied.

The formulation of Mahrt (1987) was designed to represent the implied horizontal averaging. The increased surface exchange coefficient leads indirectly to increased vertical mixing through the parameter u_*, as seen in Fig. 3. This figure is a representation of only the "first-order" feedbacks of the parameters indicated; others of course are occurring which are not shown.

An increase in the surface temperature will result from these last two modifications described, and by increasing the critical Richardson number, we can increase the PBL height. This will produce mixing over a deeper boundary layer, perhaps further increasing the surface temperature. Such an increase of Ri_c is warranted also in view of the observations, where very small-scale mixing zones are seen to exist despite overall very stable stratification on the larger scale. By allowing turbulence to continue in the model boundary layer under more stable conditions (through use of a larger critical Richardson number), we are effectively adding another facet to the parameterization of turbulence in the very stable boundary layer.

Table 1

Sensitivity Experiments

Run	Ri_c	C_h	K_h
CONTROL	1.0	Louis	TM86
TM86	0.5	Louis	TM86
RIC=3	3.0	Louis	TM86
RIC=5	5.0	Louis	TM86
MCH1.0	1.0	Mahrt, m=1	TM86
MCH0.75	1.0	Mahrt, m=0.75	TM86
MCH0.1	1.0	Mahrt, m=0.1	TM86
KONDOK	1.0	Louis	new ϕ_m
ALL	5.0	Mahrt, m=1	new ϕ_m

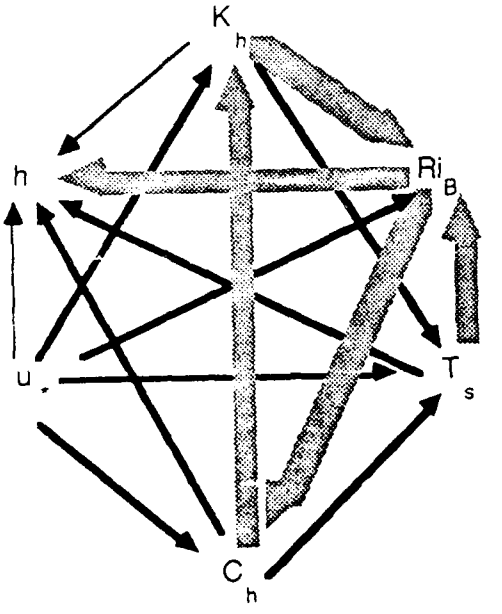

Figure 3. Interrelationships between several parameters in the proposed SBL treatment. Solid arrows represent positive feedback, large dotted arrows indicate negative feedback. The direction of the arrows show which variable is affected (at the head of the arrow).

3. Results

a. *Specification of PBL height*

In the model of TM86, a value of 0.5 for the critical Richardson number is used; the value in the present control run is 1.0. Runs of the model were also made for $Ri_c = 3$ and $Ri_c = 5$. The most pronounced impact of this change is expected to be found in the PBL height from (2), this is shown in Fig. 4. The daytime boundary layer height depends very little on the critical Richardson number; it depends much more on the temperature profile. There is not a great impact on other variables, such as skin temperature (Fig. 5), except that in the TM86 run, dew was predicted, and the additional condensational heating warmed the surface about 1.5°C.

The vertical temperature profile after 46 hr of integration time, roughly the time of minimum temperature is depicted in Fig. 6. This figure will be referred to in the sections which follow involving other comparisons. The vertical temperature structure for the runs with other critical Richardson numbers are qualitatively similar to Fig. 6, but there is some tendency for predicted boundary layer height to not match the inversion top, due to the sharpness of the initial potential temperature profile. The increased critical Richardson number does have the desired effect of deepening the SBL. This is important because predictions of SBL height for 5 m s^{-1} winds in the model of TM86 seem unrealistically shallow.

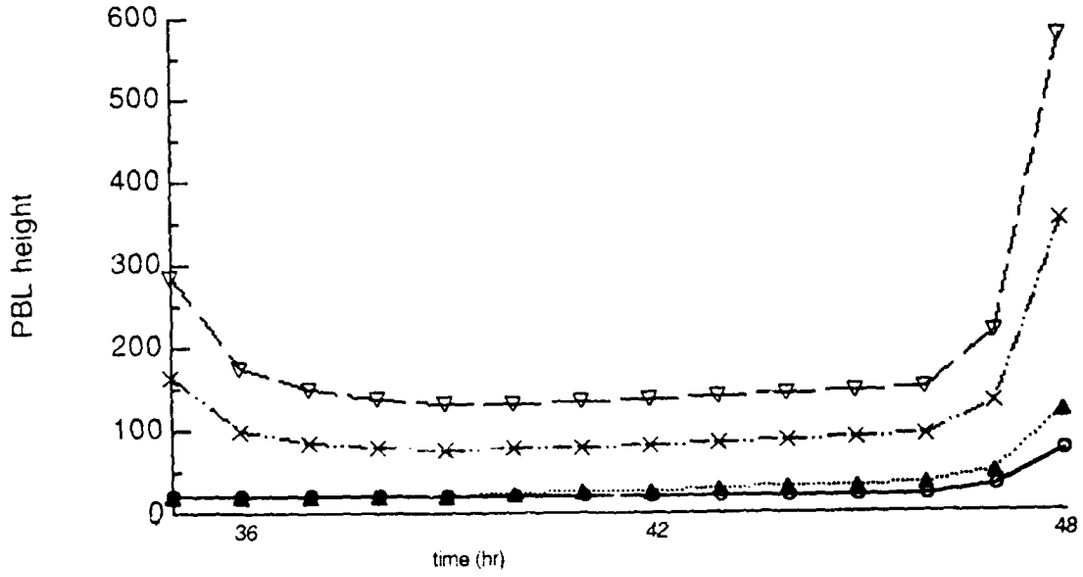

Figure 4. The effect of critical Richardson number on diagnosed boundary layer height for the control run (solid triangles); TM86 (open circles); Ri_c = 3 (X); Ri_c = 5 (inverted open triangles).

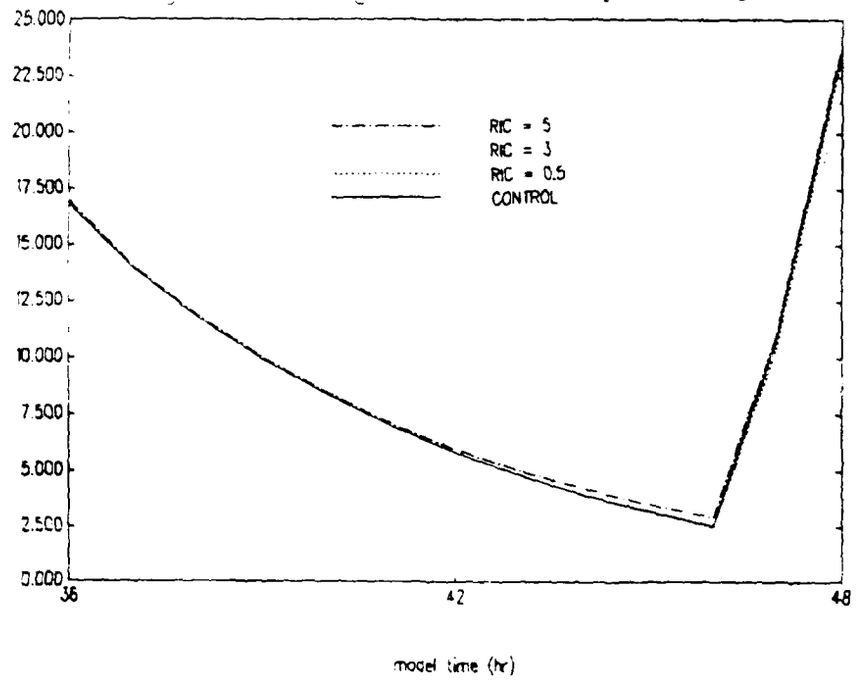

Figure 5. Effect of critical Richardson number change on skin temperature.

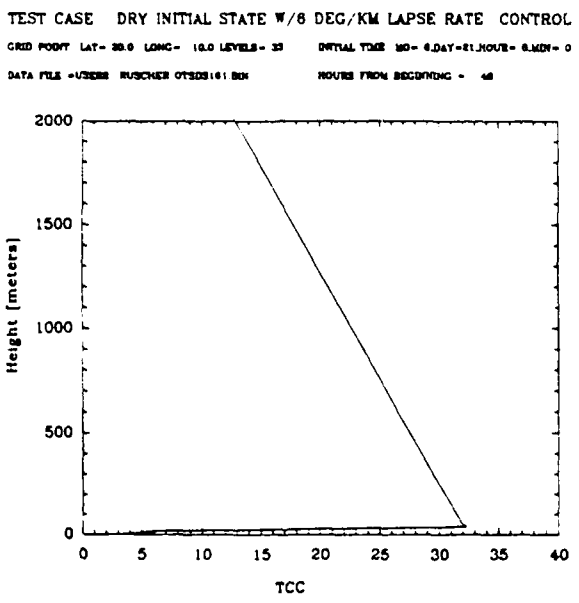

Figure 6. Predicted vertical temperature profiles for the control run after 46 hr.

b. Smooth exchange coefficient

This section discusses the impact on the SBL formulation of changing the formulation of the surface exchange coefficient. Mahrt (1987) recommends a value of m in Eq. 3 or order 1; here we test three values of m (1.0, 0.75, and 0.1). Because the new C_h falls off exponentially as $-m\ Ri_B$, a smaller value of m will enhance the exchange coefficient (fig. 6.2). Recall also the primary reason for this change; an attempt to represent the implied horizontal grid-area averaging of large subgrid scale variations of C_h, which presumably acts to increase the surface temperature.

Inclusion of the modified exchange coefficient increases the value of C_h by a factor of five, causing the skin temperature to increase, but only 0.1°C (fig. 6.7) The enhanced C_h (five times the value in the control run) more strongly mixes the lowest layer so as to *reduce* the 20 m temperature by 1.5°C (fig. 6.8). Even with m=0.1, the increase in skin temperature was a modest 0.6°C compared to the control run. Neither the PBL height nor the surface energy balance terms showed any appreciable difference for the various values of m and the control run.

Apparently the modified surface exchange coefficient enhances downward mixing of heat when the model boundary layer is stably stratified, cooling the atmosphere but only slightly warming the surface skin temperature.

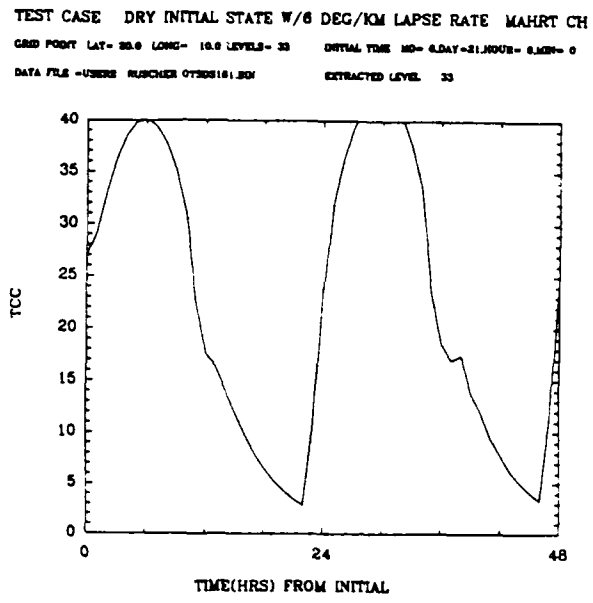

Figure 7. The time series of skin temperature for the modified exchange coefficient run with m = 1.

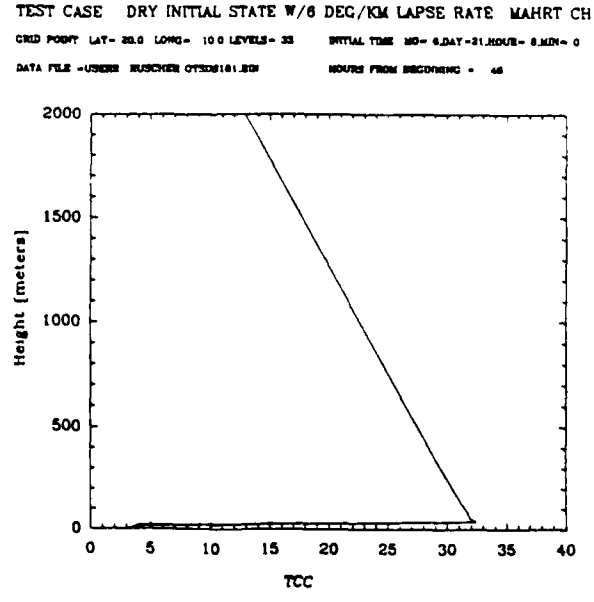

Figure 8. Predicted vertical temperature profile after 46 hr for the modified exchange coefficient run; m = 1.

c. *Enhanced eddy diffusivity*

This section describes the effects of the modified K_h, which is expected to enhance downward mixing of sensible heat at night, partially ameliorating the effects of longwave radiative heat loss from the earth's surface.

After 46 hr for the control experiment, the boundary layer depth is only 40 m (Fig. 9a), so that there are only three levels which have non-zero heat flux. In addition, the heat flux at the surface and lowest model level are always taken to be equal.. The effect of increased diffusivity with the Kondo formulation causes the surface heat flux to decrease from -2.8 W m^{-2} for the control run to -10.5 W m^{-2} (Fig. 9b).

The Kondo formulation for eddy diffusivity increases the predicted surface temperature by 0.6°C and increases the predicted air temperature by several degrees (Fig. 10). As a result, the temperature difference between the inversion top and the surface is substantially reduced. Increased magnitudes of downward sensible heat flux lead to warming in the lower boundary layer, and cooling at the boundary layer top (Fig. 11), as expected. The Kondo modification apparently exerts greater impact than the other two changes involving tunable parameters.

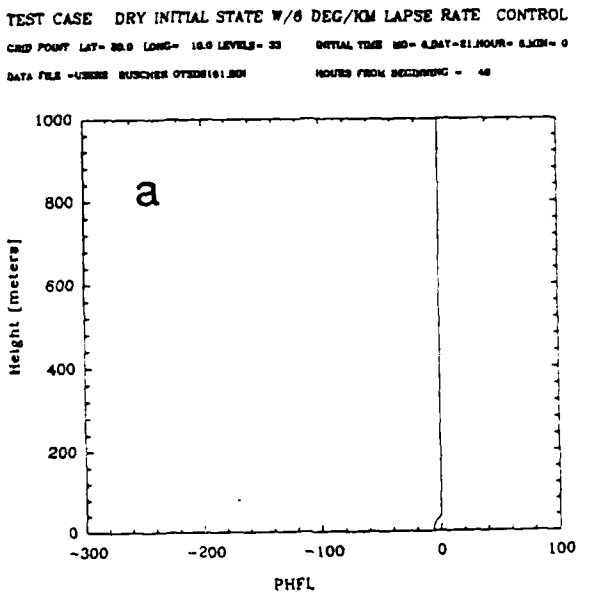

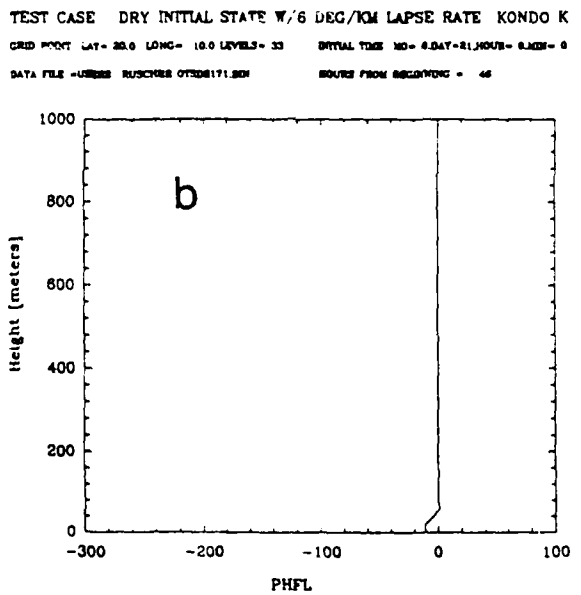

Figure 9. Vertical profile of heat flux after 46 hr: (a) for the control experiment; (b) for the enhanced eddy diffusivity experiment.

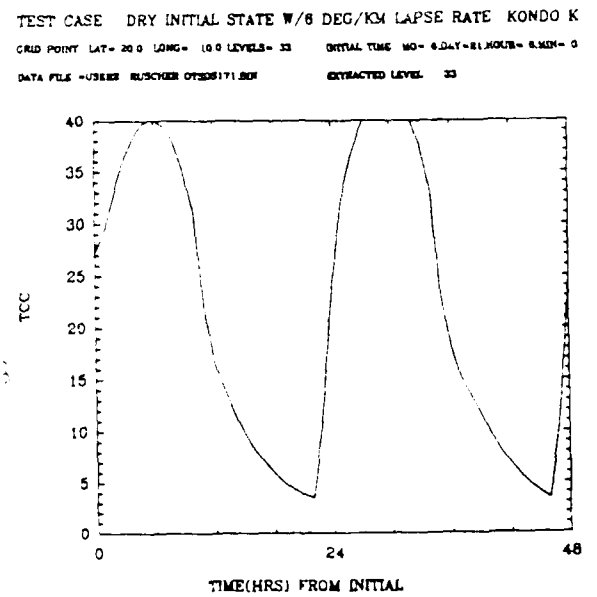

Figure 10. Time series of skin temperature for the enhanced eddy diffusivity experiment.

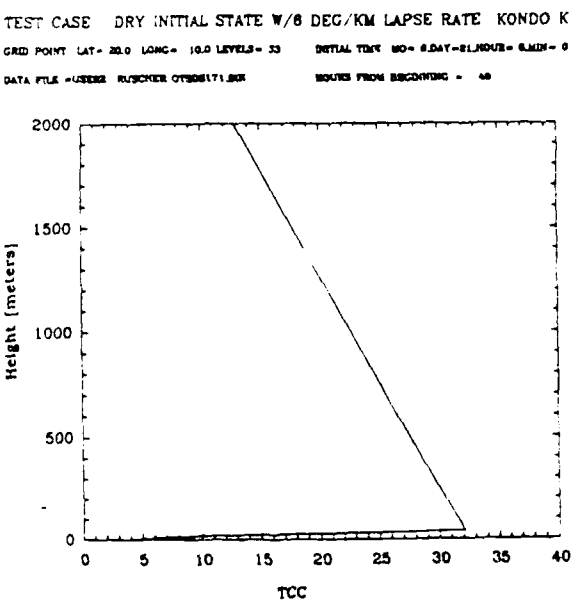

Figure 11. Vertical temperature profile after 46 hr for the enhanced eddy diffusivity experiment.

d. Summary and synthesis

The first two revised formulations for the SBL parameterization scheme lead to the desired effects, an increased PBL height and enhanced surface temperature, although the impacts seen in modified exchange coefficient experiments were quite small. It was decided that all three formulations would be incorporated into a final run; combined, these changes might be expected to work together in a synergistic effect.

By increasing the PBL height through the modification of the critical Richardson number, the Kondo-K modification affects a much deeper boundary layer, significantly changing the vertical temperature profile (Fig. 12). The surface temperature is significantly changed, as well, increasing by nearly 5°C over the control run. The surface exchange coefficient modification plays a role here, as well. The effect of increasing the eddy diffusivity alone has the undesirable effect of reducing the exchange coefficient. Apparently by smoothing out the boundary layer temperature profile and momentum profile through increased mixing, u_* will be reduced, since it depends on the vertical difference of wind speed between the surface and lowest model layer. This reduction of the surface exchange coefficient does not occur when all three changes are made. This effect is seen in Figure 13, a time series of the Kondo-K prediction of C_h and that of the control experiment. The way the Kondo-K formulation works with the other two changes is reason enough for recommending that all three changes be implemented in further tests of this revised SBL parameterization for the 1D model. Their minimal impact on daytime changes is important, as we do not wish to alter the character of the daytime PBL, which is controlled by a completely different set of equations due to the quite different dynamics involved.

The three modifications in concert lead to a more realistic boundary layer depth for 5 m s^{-1} winds (172 m compared to 20 m; Fig. 14), matching the boundary depth with the inversion top during periods of boundary layer growth, and warmer temperatures due to increased downward heat flux.

The results of all experiments are summarized in Table 2 (z_i refers to the height of the inversion; T_2 is the air temperature at the lowest model level above the surface). Of course, the model initial conditions are highly idealized in this case. In the next section, Wangara day 33 is chosen as an initial condition for one run, while a winter snow cover simulation is carried out in a second simulation. For these comparisons, only the control run and the run with all changes are shown here.

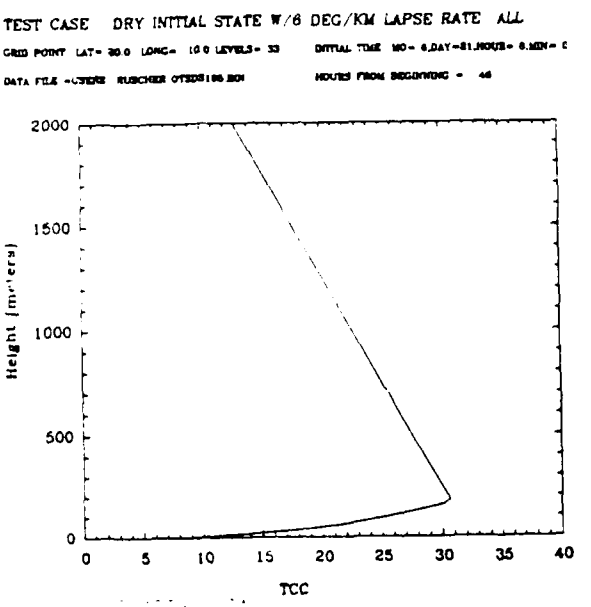

Figure 12. The vertical temperature profile after 46 hr for the experiment made using all modifications to the SBL parameterization.

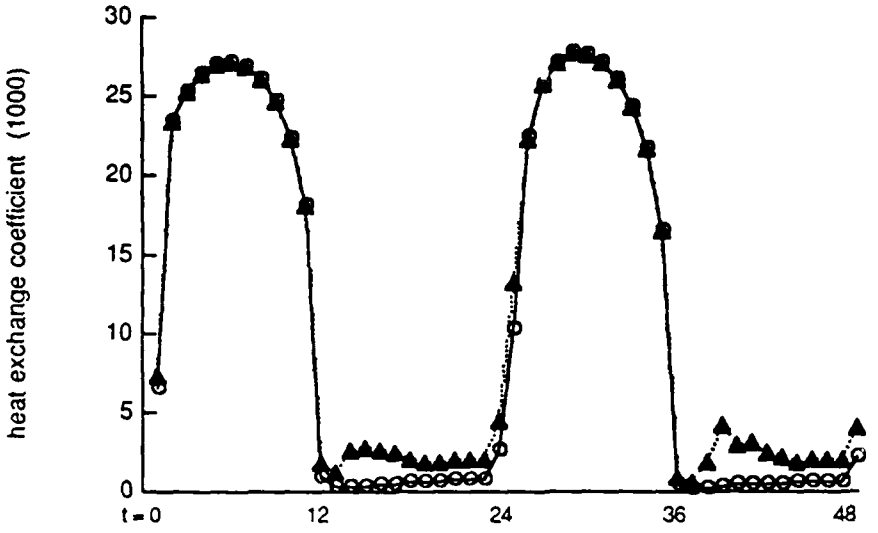

Figure 13 Time series of surface heat exchange coefficient for the MCH1.0 (solid triangles) and KONDOK (open circles) experiments.

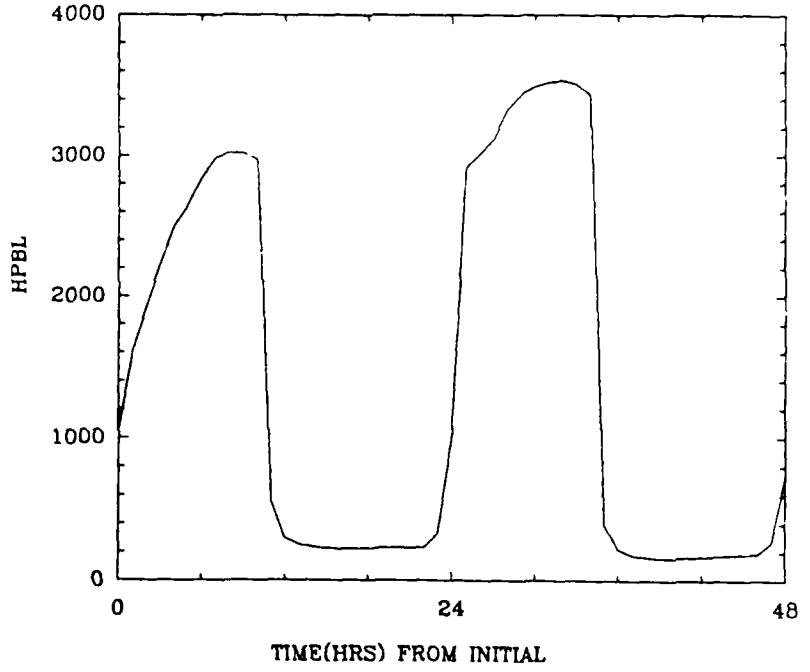

Figure 14. Time series of boundary layer height for the experiment with all modifications included.

Table 2

Results of Changes to Stable Layer Formulation for idealized dry sandy soil case

Run	h (m)	z_i (m)	T_S (°C)	T_2 (°C)
Control	40	38	2.7	5.0
TM86	20	38	4.3	9.1
RIC=3	142	38	2.5	6.3
RIC=5	172	38	3.0	8.4
Mahrt C_h, m=1	40	38	2.8	3.5
Mahrt C_h, m=0.75	40	38	2.9	3.6
Mahrt C_h, m=0.1	44	38	2.5	2.9
Kondo-K	42	38	3.3	11.3
ALL	191	181	8.0	14.0

4. Other tests

a. *Wangara Day 33*

The initial vertical temperature profile for 0610 EST (Eastern Australia Standard Time) on Wangara day 33 is shown in Fig. 15a. The surface temperature is just below freezing and a strong radiation inversion develops under conditions of high pressure, clear skies, and modest winds. The modified model predicts much warmer surface temperatures than the control run (Fig. 16). The observed surface temperature at 0604 on day 35 was 7.3°C. The control run predicted a surface temperature of 2.1°C, while the modified run yielded 7.6°C, quite close to the observed value.

The heat flux for the modified model run is much larger than the control run (Fig. 17). Due in part to the increased heat flux, z_i for the modified run is 288 m, while it is only 1.. m for the control; this is not a result of only the enhanced diffusivity as the increased Ri_c also plays a role. The observed inversion top at 0623 on Wangara day 35 was 400 m (Fig. 15b); again the modified model results look superior. However, this is tempered by the observation that the strength of the inversion (measured here in terms of T_{z_i} - T_{sfc}) for day 35 was only 3.4°C; the modified run had a vertical temperature change of 7.3°C, while the control run had an inversion strength of 13.4°C! There is certainly room for improvement and runs which include prescribed vertical motion and perhaps the cloud model of Chu (1986) are indicated in future research. Nevertheless, the comparison indicates optimistic results for the three model changes.

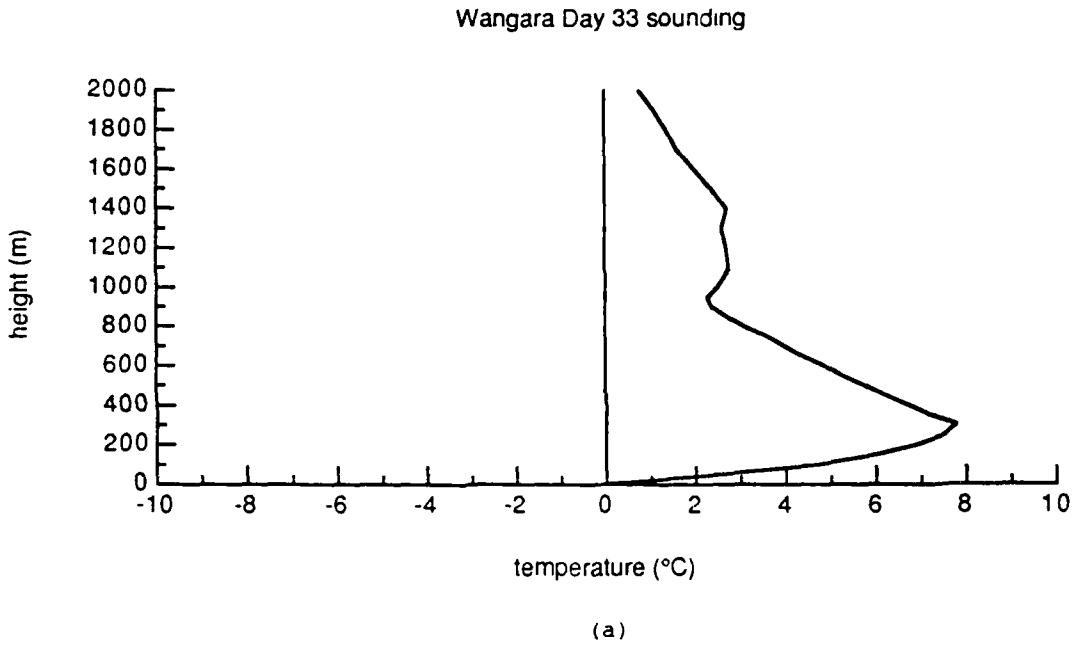

(a)

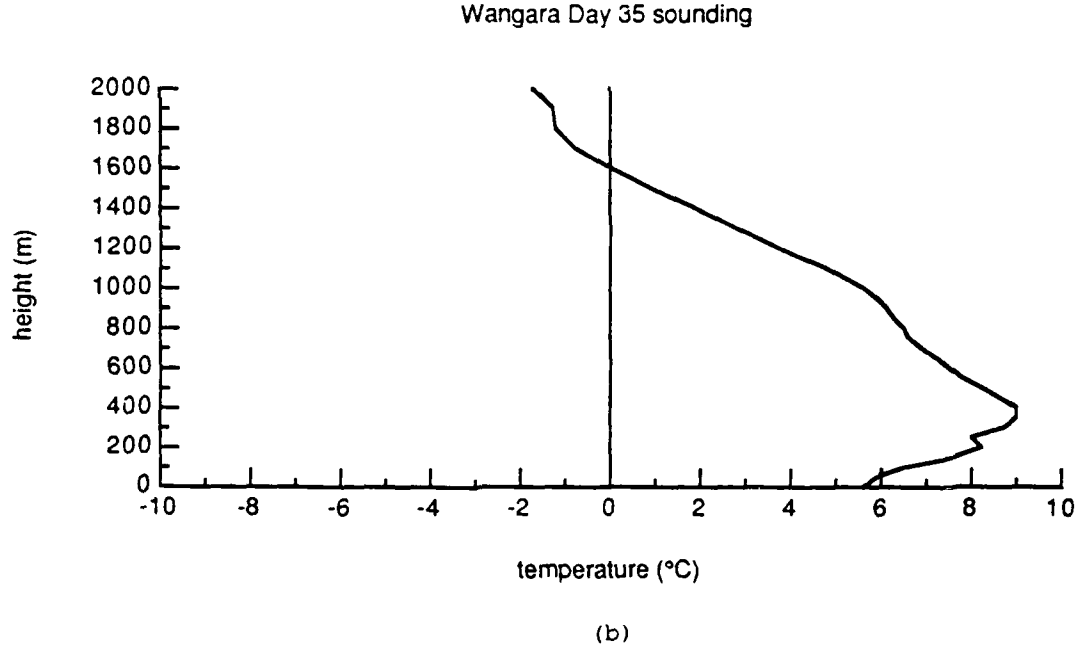

(b)

Figure 15. Observed temperature from early-morning sounding for Wangara day 33 (a). As in (a) except for Wangara day 35 (b).

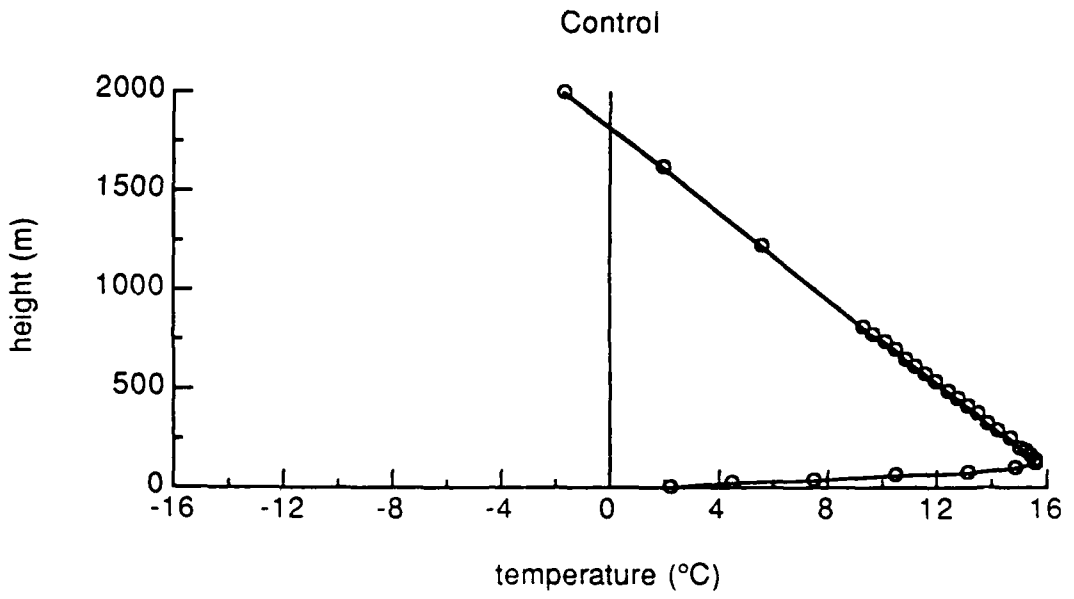

(a)

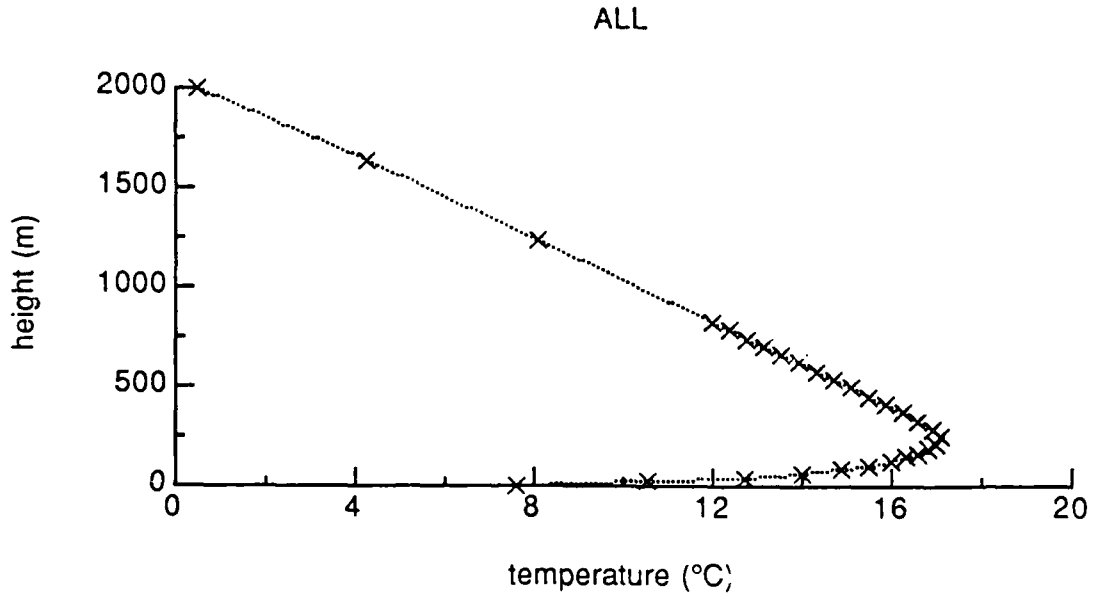

(b)

Figure 16. Simulated Wangara temperature profile for control run after 48 hr (a). As in (a) except for modified run (b).

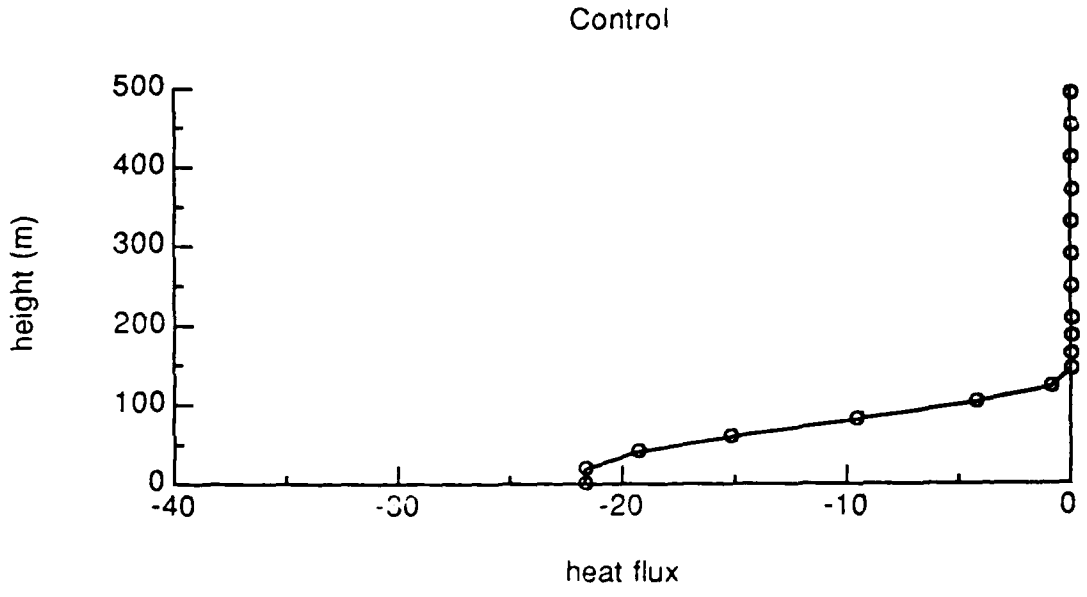

(a)

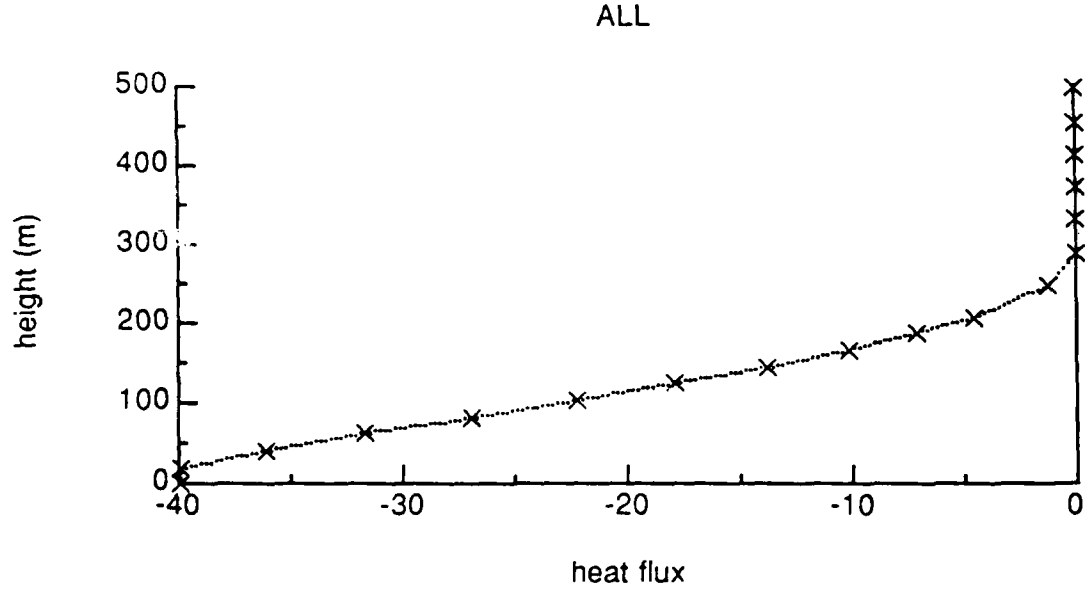

(b)

Figure 17. Simulated heat flux profile (W m^{-2}) after 48 hr for the Wangara control run (a). As in (a) except for the Wangara modified run (b).

b. Winter snow cover simulation

Sensitivity tests were also performed for the 1-D model run with a surface snow cover. The surface snow cover model of Pan (see Appendix C) is included in this run. The initial conditions for this test are a 10 cm snow cover, and a 1200 GMT sounding taken from The Pas, Manitoba, during February of 1987. There were northwest winds of about 5 m s^{-1} near the surface; again, moisture effects are not included. Comparison to observations is of course an impossibility here because of the neglected large-scale forcing.

A pronounced inversion typical of the arctic or well-developed cP (continental polar) air mass is present in the initial temperature profile (Fig. 18). The control run is colder at the surface than the modified run after 46 hr, as expected (Fig. 19). The diagnosed PBL height is 160 m for the modified model, compared to 41 m for the control model; in each case the surface inversion has a deeper inversion overlying it, a manifestation of the original input data. The vertical temperature profile for the modified case (Fig. 20) is quite typical of high-latitude wintertime inversions (Dalrymple, 1966). Sensible heat transport seems to be playing an important role in the maintenance of the inversion in this test.

Oke (1978) presents a typical surface energy balance over snow cover and a main feature is a negative sensible heat flux. The model-simulated sensible heat fluxes are -3.0 W m^{-2} and -16.7 W m^{-2} for the control and modified runs, respectively; Oke reports values of order -10 W m^{-2}. Other than these comparisons, we cannot make any definitive conclusions either about the abilities of the snow cover model or about the impact which the modifications will have on snow cover simulations.

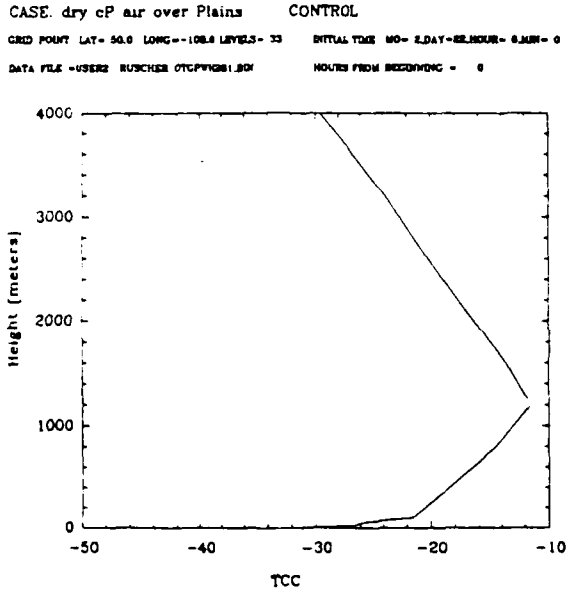

Figure 18. Initial temperature profile for snow cover simulation.

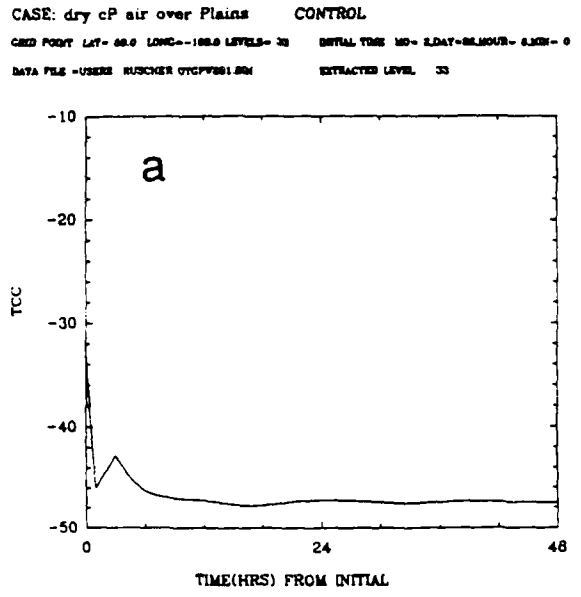

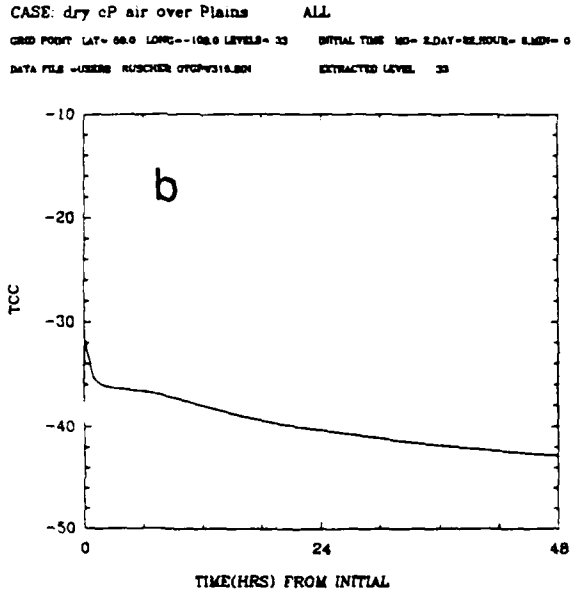

Figure 19. Time series of skin temperature for the control run of the snow cover case(a) As in (a) except for modified run (b).

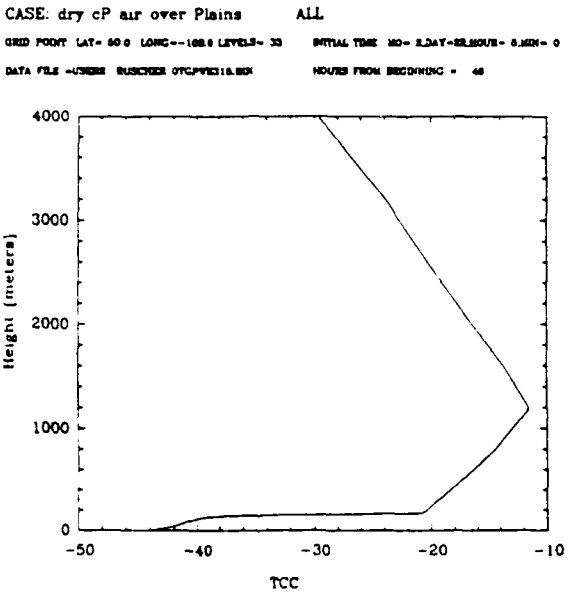

Figure 20. Temperature profile after 46 hr for the modified snow cover simulation.

5. Conclusions

Three changes have been made to the stable layer formulation of the model of TM86 which significantly improve the performance of the model. The critical Richardson number change involves strictly a "tunable" parameter, in that observations are not definitive. This is probably the hardest to justify based on observational evidence, but it seems necessary to provide for realistically deep stable boundary layers with moderate wind speeds. Strong support exists for the other two changes, however, enhancements to the surface exchange coefficients and boundary layer eddy diffusivity. In tests with an idealized atmosphere, the results indicate that the three proposed changes seem to work in a synergistic manner to improve the prediction of SBL physics, including PBL depth, surface skin temperature, and vertical temperature profile. Although improvements are noted for the changes tested individually, only the increased critical Richardson number change led by itself to a boundary layer significantly different from the control model.

The revised model was also tested for two very different conditions. One was a wintertime snow cover situation from February 1987 over the Canadian prairie, the other was for the Wangara field experiment. Although direct comparison with observations is not possible in either case because this simple model must neglect some large-scale processes, results of the revised SBL model are encouraging.

Once further tests of these formulations are made, which will be the subject of future research, other possible modifications to the stable layer formulation might be considered. For example, currently in TM86 and in the model calculations described in the present research, the ratio of the heat exchange coefficient (C_h) to the drag coefficient (C_m) is set to be 1.35 (this is also true for K_h/K_m), following Businger *et al.* (1971). This value (which corresponds to a Prandtl number $Pr = 1.35^{-1} = 0.74$) has been shown to be valid for near-neutral conditions, but its value in conditions far from neutral still seems to be somewhat controversial. For example, Kondo *et al.* (1978) suggest a ratio much smaller than one. One might expect the logic behind this is that pressure fluctuations due to gravity waves, ubiquitous in the SBL, transport momentum but not heat (Finnigan and Einaudi, 1981, Caughey, 1982, and Hunt *et al.*, 1985). It could be noted here also that the pressure

perturbations due to the turbulence itself may lead directly to momentum transport (Schols and Wartena, 1986). While these observations are valid for linear wave motions, the stably-stratified PBL is thought to contain highly nonlinear motions, as the analysis of Ruscher and Mahrt (1987) and others have shown; which would transport heat, as well. Parameterization of turbulence in the free atmosphere is another area which requires some research.

The results for the snow cover simulation in particular should be deemed very preliminary at this point. Comparison with observed data using a more realistic model (including vertical motion, advection, and clouds, for example) also needs to be performed. Still, the fact that these simple modifications are able to abate the nocturnal cooling is encouraging and they warrant further testing.

Appendix C: Modelling the Snow Cover

1. Introduction

In an effort to parameterize the boundary layer heat and moisture transport for the AFGL global forecast model (Brenner *et al.*, 1984), a combined model of the boundary layer and the soil has been developed (Mahrt and Pan, 1984; Troen and Mahrt, 1986; and Pan and Mahrt, 1987). In order to implement the boundary layer package into the global model, it is necessary to include the effects of snowcover, which can be an important part of the boundary layer-soil system (Tuccillo, 1987).

Snow cover serves as the upper boundary of the earth's surface, thereby affecting the boundary layer as well as the soil. Although snowcover reduces the available energy at the surface because of its high albedo for solar radiation and high emissivity in the spectral range of most terrestrial radiation, its insulative properties exert the greatest influence on the soil (Gray and Male, 1981). The thermal conductivity of new snow is roughly an order of magnitude less than that of most soils. As snow "ages" its thermal conductivity increases, but generally remains less than that of most soil, and its albedo decreases.

For the atmospheric boundary layer, the presence of snow means almost complete removal of the soil heat flux. The nocturnal cooling that is usually balanced by the soil heat flux (Oke, 1978) may lead to much cooler surface temperatures in the presence of snow. Siberia, northwestern North America and Antarctica are among the regions where intense radiative cooling occurs, resulting in the formation of air masses characterized by very low surface temperature and strong surface inversions up to 1 to 2 km thick.

In this report, we will outline the simple formulation that has been developed to model the snowcover.

2. Model

At the present stage, the global model does not distinguish precipitation as either snow or rain as the precipitation prediction is based on a simple parameterization method. We categorize fallen precipitation as snow when the temperature at 85 kPa is below the 0°C threshold. Snow is also assumed to cover the grid box area evenly. The first step in the model is to

make an estimate of the snow heat flux G when snow is present by using relationship

$$G = \kappa_s \frac{T_s - T_{soil}}{h_s} \qquad (C1)$$

where κ_s is the thermal diffusivity for snow, T_s is the "skin" temperature, T_{soil} is the top-layer soil temperature (in the present model, the top layer is 5 cm thick), and h_s is the depth of the snow layer (assumed to be ten times the water-equivalent snow depth).

The thermal diffusivity for snow depends on the porosity of snow and can vary from 0.063 W K^{-1} m^{-1} for new snow with a porosity of 0.95 to 0.71 W K^{-1} m^{-1} for packed snow with porosity of 0.5 (comparable to clay). Unless we try to resolve the snow surface into many layers and keep track of the "age" of each layer, we can not possibly know the porosity of the snow pack. In this model, we choose the value of 0.13 W K^{-1} m^{-1} for κ_s which corresponds to a porosity of 0.8. The soil surface temperature is assumed to be the same as the top-layer averaged soil temperature. This is supported by observations that the largest thermal gradient below the snow surface is near the top of the snow layer (Oke, 1978), due to weak thermal diffusion within the snow layer. When snow falls over warm soil, the snow heat flux may lead to snowmelt.

The calculation of the snow heat flux enables one to calculate the potential evaporation E_p using the surface energy balance:

$$(1-\alpha)S\downarrow + L\downarrow - \sigma T'^4 = G + \rho_o c_p C_h |V| (T' - T_o) + LE_p \qquad (C2)$$

where

$$E_p = \rho_o C_h |V| \left(q_s(T') - q_o \right) . \qquad (C3)$$

The terms on the left-hand side of (2) are the downward short- and long-wave radiative flux and the upward longwave radiative flux. The terms on the right-hand side are the snow heat flux, the sensible and the latent heat flux. The skin temperature T′ is the temperature of the surface if the snow surface is evaporating at the potential rate. While the unit of E_p in the surface energy balance are kg m^{-2} s^{-1}, typical soil hydrological applications use the units m s^{-1}. The conversion is accomplished via the density of water (ρ_w = 10^3 kg m^{-3}).

The snow evaporates/sublimates at the following rate:

$$E = \begin{cases} E_p & ; \quad h_s \geq E_p \Delta t \\ \dfrac{h_s}{\Delta t} & ; \quad h_s < E_p \Delta t \end{cases} . \qquad (C4)$$

When the depth of the snow layer is thick, it will evaporate at the potential rate for an entire time step. When the snow layer is thin so that it can not maintain the potential rate, we assume the snow to evaporate evenly and completely over the time interval Δt .

Once the evaporation rate E is determined, the skin temperature T_s is calculated by solving the surface energy balance (2) again:

$$(1-\alpha)S\downarrow + L\downarrow - \sigma T_s^4 = D_s \frac{T_s - T_{soil}}{h_s} + \rho_o c_p C_h |V| (T_s - T_o) + LE . \qquad (C5)$$

If the resulting skin temperature is above the melting point of snow (T_c = 273.16 K), the amount of snowmelt h_m is calculated as follows:

$$(1-\alpha)S\downarrow + L\downarrow - \sigma T_c^4 = D_s \frac{T_c - T_{soil}}{h_s} + \rho_o c_p C_h |V| (T_c - T_o) + LE + L_i h_m , \qquad (C6)$$

where L_i is the latent heat of fusion.

When precipitation falls through the air in the model, it is assumed to have the same temperature as that of the lowest atmospheric layer (this is arbitrarily assumed at the present stage). Conversion of warm rain to ice or snow may be an important process during warm front passages and is included in the model. Excess snow melt is allowed to drip into the top soil layer while direct evaporation from the soil surface is inhibited. Snowcover therefore helps soil to retain moisture. Soil temperature is updated by assuming zero heat flux across the snow-soil interface.

REFERENCES

Abarbanel, H. D. I., D. D. Holm, J. E. Marsden, and T. S. Ratiu, 1986: Nonlinear stability analysis of stratified fluid equilibria. *Phil. Trans. Roy. Soc., Lond.*, **A318**, 349-409.

André, J.-C., and L. Mahrt, 1982: The nocturnal surface inversion and influence of clear-air radiative cooling. *J. Atmos. Sci.*, **39**, 864-878.

Böttger, H., 1987: Changes to the operational forecasting system. *ECMWF Newsletter* No. 38 (June), 1-9.

Brenner, S., C.-H. Yang, and K. Mitchell, 1984: *The AFGL Global Spectral Model: Expanded Resolution Baseline Version.* Rept. No. AFGL-TR-84-0308, Air Force Geophysics Laboratory, Hanscom AFB, 72 pp. [ADA160370]

Brost, R. A., and J. C. Wyngaard, 1978: A model study of the stably stratified boundary layer. *J. Atmos. Sci.*, **35**, 1427-1440.

Brutsaert, W. H., 1982: *Evaporation into the Atmosphere.* Boston: D. Reidel, 299 pp.

Businger, J. A., J. C. Wyngaard, Y. Izumi, and E. F. Bradley, 1971: Flux-profile relationships in the atmospheric surface layer. *J. Atmos. Sci.*, **28**, 181-189.

Caughey, S. J., 1982: Observed characteristics of the atmospheric boundary layer. *Atmospheric Turbulence and Air Pollution Modelling* (F. T. M. Nieuwstadt and H. van Dop, eds.). D. Reidel, Dordrecht, 107-158.

Chu, C.-T., 1986: Parameterization of shallow convection in the boundary layer. Masters thesis. Oregon State University, Corvallis, Oregon.

Clarke, R. H., A. J. Dyer, R. R. Brook, D. G. Reid, and A. J. Troup, 1971: *The Wangara Experiment: Boundary Layer Data.* Div. Meteorol. Phys. Tech. Paper No. 19. CSIRO, Melbourne, 316+ pp.

Dalrymple, P. C., 1966: A physical climatology of the antarctic plateau. *Studies in Antarctic Meteorology* (M. J. Rubin, ed.). Vol. 9 of the Antarctic Research Series, American Geophysical Union, Washington, 195-231.

Finnigan, J. J. and F. Einaudi, 1981: The interaction between an internal gravity wave and the planetary boundary layer. Part II: Effect of the wave on the turbulence structure. *Quart. J. Roy. Meteorol. Soc.*, **107**, 807-832.

Gray, D. M. and D. H. Male, 1981: *Handbook of Snow.* Pergamon Press, Toronto, 776 pp.

Hunt, J. C. R., J. C. Kaimal, J. E. Gaynor, and A. Korrell, 1985: Some observations of turbulence structure in stable layers. *Quart. J. Roy. Meteorol Soc.*, **111**, 793-816.

Kondo, J., O. Kanechika, and N. Yasuda, 1978: Heat and momentum transfers under strong stability in the atmospheric surface layer. *J. Atmos. Sci.*, **35**, 1012-1021.

Kunkel, K. E. and D. L. Walters, 1982: Intermittent turbulence in measurements of the temperature and structure parameter under very stable conditions. *Bound.-Layer Meteorol.*, **22**, 49-60.

Lacser, A. and S. P. S. Arya, 1986: A comparative assessment of mixing-length parameterizations in the stably stratified nocturnal boundary layer. *Bound.-Layer Meteorol.*, **36**, 53-70.

Louis, J.-F., 1979: A parametric model of vertical eddy fluxes in the atmosphere. *Bound.-Layer Meteorol.*, **17**, 187-202.

Lyons, R., H. A. Panofsky, and S. Wollaston, 1964: The critical Richardson number and its implications for forecast problems. *J. Appl. Meteorol.*, **3**, 136-142.

Mahrt, L., R. C. Heald, D. H. Lenschow, B. B. Stankov, and I. Troen, 1979: An observational study of the structure of the nocturnal boundary layer. *Bound.-Layer Meteorol.*, **17**, 247-264.

Mahrt, L. and H.-L. Pan, 1984: A two-layer model of soil hydrology. *Bound.-Layer Meteor.*, **29**, 1-20.

Mahrt, L., 1987: Grid-averaged surface fluxes. *Mon. Wea. Rev.*, **115**, 1550-1560.

Miles, J. W., 1987: Richardson's number revisited. *Preprints, Third Int. Symp. on Stratified Flows*. Calif. Inst. Tech., Pasadena, General Session.

Nieuwstadt, F. T. M., 1984: The turbulent structure of the stable, nocturnal boundary layer. *J. Atmos. Sci.*, **41**, 2202-2216.

Oke, T.R., 1978: *Boundary layer climates*. Methuen, London, 372 pp.

Pan, H.-L. and L. Mahrt, 1987: Interaction between soil hydrology and boundary-layer development. *Bound.-Layer Meteor.*, **38**, 185-202.

Panofsky, H. A. and J. A. Dutton, 1984: *Atmospheric Turbulence*. Wiley, New York, 397 pp.

Ruscher P. H. and L. Mahrt, 1987: Coherent structures in the very stable atmospheric boundary layer. Conditionally accepted for publication in *Bound.-Layer Meteorol.*

Schols, J. L. J. and L. Wartena, 1986: A dynamical description of turbulent structures in the near neutral atmospheric surface layer: The role of static pressure fluctuations. *Bound.-Layer Meteorol.*, **34**, 1-15.

Sommeria, G., 1987: Parameterization of the planetary boundary layer in large-scale atmospheric models. *CO_2 and Climate Sensitivity* (M. E. Schlesinger, ed.). D. Reidel, Dordrecht, in press.

Sorbjan, Z., 1987: An examination of local similarity theory in the stably stratified boundary layer. *Bound.-Layer Meteorol.*, **38**, 63-71.

Troen, I. and L. Mahrt, 1986: A simple model of the atmospheric boundary layer: Sensitivity to surface evaporation. *Bound.-Layer Meteorol.*, **37**, 129-148.

Tuccillo, J. J., 1987: Impact of snow cover on NGM forecast temperature. *NWS West. Region Tech. Attach.*, **87**, No. 2, 7 pp.

Webb, E. K., 1970: Profile relationships: The log-linear range, and an extension to strong stability. *Quart. J. Roy. Meteorol.*, **96**, 67-90.

Yang, C.-H., K. Mitchell, D. Norquist, and S. Yee, 1988: Diagnostics for and evaluations of new physical parameterization schemes for global NWP models. In preparation. Air Force Geophysics Laboratory, Hanscom AFB.

VI. PARAMETERIZATION OF SHALLOW CONVECTION IN THE BOUNDARY LAYER

1. Introduction

Shallow convection is thought to be one of the crucial sub-grid scale mechanisms for transporting moisture and heat from the planetary boundary layer to the free atmosphere. It is also thought to be an important mechanism that provides a balance against large scale sinking motion and maintains a steady state well-mixed subcloud layer under undisturbed trade wind situations. By its vertical transfer of water vapor, it supports the growth of the deep, precipitating cumulus towers. Without this mechanism moisture will accumulate in the lower boundary layer and cut down the latent heat and sensible heat fluxes from the surface.

Yanai et al. (1973) introduced a budget approach to implicitly calculate the first order sub-grid scale turbulent flux from large scale observation data. They defined Q1 (apparent heat source) to be the heating due to radiation, the release of latent heat by net condensation, and the divergence of the vertical eddy transport of sensible heat, and Q2 (apparent moisture sink) to be the net condensation and the divergence of the vertical eddy transport of moisture. They found the Q2 profile in the tropical ocean to possess peaks in the upper troposphere as well as in the lower troposphere. The moisture sink in the upper troposphere is interpreted as due to convective precipitation. The moisture sink in the lower troposphere and relative minimum in Q2 between the two peaks are interpreted as due to transport of moisture upward from the lower troposphere and detrainment of liquid water and water vapor in mid-troposphere by the non-precipitating shallow clouds. They concluded that the relative minimum between the two peaks which counteracts the drying by environmental sinking motion is due to the water vapor and liquid water detrainment from the clouds, especially the shallow clouds in the lower troposphere.

Nitta and Esbensen (1974) used a similar approach to estimate the large-scale heat and moisture budgets over the tropical Atlantic Ocean during Phase 3 (22-30 June 1969) of the Barbados Oceanographic and Meteorological Experiment (BOMEX). For undisturbed period (22-26 June 1969) with weak cumulus convection, the sub-grid scale Q1 and Q2 profiles both show a minimum near

the bottom of the trade wind inversion layer. This phenomenon is interpreted as the effect of moistening and cooling due to moisture detrained and re-evaporated at the top of the shallow cumulus.

There are some other works that obtained similar results by using Air Mass Transformation Experiment (AMTEX) data (e.g. Esbensen, 1975; Nitta, 1976; Murty, 1976; Nitta and So, 1980). As an example we show Q1 and Q2 profiles derived from AMTEX 75 data in Fig. 1 which is taken from Nitta and So (1980).

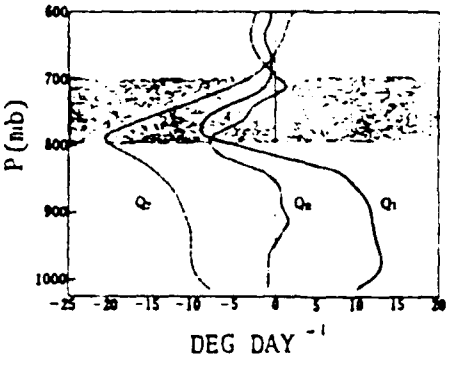

Figure 1 Q1, Q2 profile from AMTEX75 period average. Figure taken from Nitta and So (1980).

The importance of the shallow convection is not only demonstrated by the budget studies but also in numerical modeling studies. Tiedtke (1983) showed that it is necessary to parameterize such processes in the general circulation model. He found that with both the Arakawa-Schubert (1974) and the Kuo (1965) deep convection schemes, moisture accumulated in the lower boundary layer and there lacks another mechanism to transport the excess moisture up to the upper air environment. By employing a simple constant cloud diffusivity profile as a shallow convection scheme in the European Centre for Medium-Range Weather

Forecasts (ECMWF) operational model, Tiedtke was able to not only get rid of the excess moisture near the surface and significantly improve the model's forecast but also reproduce the BOMEX and ATEX (Atlantic Trade Wind Experiment, 1969) sounding data in one-dimensional model simulations.

Direct calculations of the turbulent heat and moisture flux (e.g. LeMone and Pennell, 1976; Nicholls, 1980) using data from the GATE (GARP (Global Atmospheric Research Program) Atlantic Tropical Experiment, 1980), however, have found little evidence of the effect of the shallow cumulus. The study of California stratus by Albrecht (1985) using aircraft data, on the other hand, does seem to show an enhancement of the moisture flux. It is possible that the cloud amount may play a role in the magnitude of the fluxes as the GATE studies are for days with little shallow convection.

One of the goals of this work is to derive a shallow convection scheme using BOMEX, AMTEX, GATE, and BLX83 (Boundary Layer Experiment 1983 in Oklahoma, Stull and Eloranta, 1984) data. To be consistent with the PBL model treatment, we seek to parameterize the effect of shallow clouds using a diffusivity formulation in which the cloud diffusivity profile depends on the cloud amount. The cloud amount forecast equation is derived from the BLX83 data and is only relative humidity dependent.

Troen and Mahrt (1986) developed a PBL column model to parameterize the turbulent mixing within the boundary layer for a global spectral model of the Air Force Geophysics Laboratory (AFGL) (Brenner et al., 1984). Extensive tests of the PBL model have been performed (Troen and Mahrt, 1986; Pan and Mahrt, 1987) and the results indicate that the model is capable of producing realistic simulations of the boundary layer under various atmospheric and lower surface conditions. The shallow convection scheme is developed for this model. Results of the sensitive tests are compared against the constant cloud diffusivity scheme of Tiedtke (1983).

2. Data

Data from BOMEX, AMTEX72 and GATE were chosen for this study. While the data covered different synoptic situations, we chose to use data during undisturbed periods with a trade wind inversion capping the unstable boundary layer when only shallow convective clouds are present. Following are some of the characteristics of each data set (see Table 1 for summary).

2.1. BOMEX

The Barbados Oceanographic and Meteorological Experiment (BOMEX) was conducted during May and June 1969 over the area east of the Barbados. The season was chosen to provide a wide range of convective activities in the absence of well-developed storms. The primary objective of this experiment was to determine the rate of transfer of water vapor, heat and momentum from the tropical ocean to the atmosphere. This experiment is divided into three phases. Only Phase 3 from June 22 to 26 is used in this study because of a particular shortage of data early on the 22nd and late on the 26th. This period was marked by relatively undisturbed trade-wind weather with light southerly wind near the sea surface turning into stronger northerly wind aloft. Strong easterly winds appeared in the lower boundary layer and decreased slowly below the inversion. Cloud cover was estimated from ATS-2 image-enhancement satellite pictures and is about 40% to 50% during the period. Sea surface temperature was 28°C, the period-averaged sensible heat flux was 15 W m^{-2} and the latent heat flux was 167 W m^{-2}.

2.2. AMTEX74

The Air-Mass Transformation Experiment in 1974 (AMTEX74) was conducted during 14 to 28 February 1974 over the Kuroshio region around the Nansei Island of Japan. During this season the cold air mass is strongly modified when it passes over the oceanic regions to the east of the Asian continent. Due to the large amount of heat and moisture supplied from the sea surface, cumulus activity is strongly enhanced as the air travels farther over the ocean. The primary objective of AMTEX was to clarify the role of the cumulus

clouds and the boundary layer eddies in the air mass transformation process and their relationship to the development of disturbances.

This experiment was divided into three periods. Only the first period (from 14 to 16 February) was used, during which a local high pressure center is located to the northeast of the AMTEX area and southerly wind prevailed in the lower layer below the inversion. During this period the average sea surface temperature was 16°C, cloud cover was 45%, the surface latent heat flux is 252 W m^{-2} and sensible heat flux was 42 W m^{-2}. Below the inversion southerly wind speed increased with height and turned into strong westerly wind above the inversion. Sinking motion was stronger than for the other cases used in this study.

2.3. GATE

The GARP Atlantic Tropical Experiment (GATE) was conducted during 1974). The experiment was divided into three phases but only data from Phase three is used due to shortage of data for undisturbed situations during the first two phases. During this period the boundary layer was capped by a weak trade wind inversion and boundary layer itself was nearly neutral and only slightly unstable. Average cloud cover was only 10% with little cumulus activity. The Boundary layer structure appeared well-mixed for most days so that the modeled counter-gradient effect becomes important for the heat and moisture flux profiles. According to observation the northerly wind component was stronger than the easterly or westerly wind component. Sea surface temperature was about 26°C, average latent heat flux was 90 W m^{-2} and sensible heat flux was 10 W m^{-2}.

Table 1. Summary of the surface sensible heat flux, latent heat flux, average cloud cover and sea surface temperature (SST) of the BOMEX, AMTEX, GATE and undisturbed period data.

Data	Sensible Heat Flux ($W\ m^{-2}$)	Latent Heat Flux ($W\ m^{-2}$)	Cloud Cover (%)	SST (°C)
BOMEX	15	167	45	28
AMTEX	42	252	45	16
GATE	10	90	10	26

3. The Model

3.1. The OSU PBL Model

In the Oregon State University Planetary Boundary Layer model (OSU PBL) the surface fluxes are computed according to the Louis (1979) formula and the layer below 50 m is considered to be the constant-flux layer. Above this layer, temperature (θ), moisture (q), and momentum (u,v) fluxes due to the boundary layer turbulent mixing with environment are parameterized as diffusive processes:

$$\frac{\partial X}{\partial t} = \frac{\partial}{\partial z} K \left(\frac{\partial X}{\partial z} - \gamma\right) \qquad (1)$$

where $X = [u,v,\theta,q]$, K is the parameterized coefficient of diffusivity and γ is the parameterized counter-gradient effect (see Troen and Mahrt, 1986 for detail).

Since this is a 1-D column model, there is no horizontal advection process affecting the model structure during the sensitivity tests. We prescribed the initial vertical profile of horizontal (u,v) and vertical (w) motion, temperature (T) and mixing ratio (q). Additional assumptions are made as follows:

1. The large scale vertical motion field is a constant profile throughout the sensitivity test period. The turbulent and convective process can only change the wind, temperature and mixing ratio fields within the boundary layer.
2. Super-saturation is removed by assuming that the excess moisture is carried away by the trade wind and advected downstream.
3. The sea surface temperature is assumed as a constant throughout the sensitivity test period.
4. Model's top is 4 km which constrains the boundary layer top below this level. Between 50 m and 1.05 km, the model resolution is 200 m. Above 1.05 km, the model resolution is 100 m.

3.2. The OSU Cloud Scheme

A formula for predicting the unstable boundary layer shallow cumulus amount is derived from the BLX83 aircraft and the AMTEX sounding data. The

best parameter was found to be the relative humidity at the Lifting Condensation Level (LCL) within the boundary layer. A least square fit of a quadratic polynomial is used to predict the cloud amount CC:

$$CC = A0 + A1 \cdot RH + A2 \cdot RH^2, \quad \text{for } RH \geq 57\% \tag{2}$$

and the coefficients calculated from the data are: A0 = -0.7417, A1 = -1.25665 and A2 = 2.264E-2. In Figure 2 we present the observed relationship between cloud cover and relative humidity at the cloud base. The solid line in Figure 2 represents the function in Eq. (2).

Slingo (1980) also developed a cloud parameterization scheme derived using GATE data for use in the British Meteorological Office's tropical model. Slingo's formulae for low cloud cover (Fig. 2) with and without inversion are:

(a) For $(d\theta/dp)_{min} \leq -0.07(K/mb)$, we assume the existence of inversion and use the formula

$$CC = -16.67(d\theta/dp)_{min} + \delta(RH-80)^2/400 - 1.167 \quad , \tag{3}$$

where

$$\delta = \begin{cases} 1 & RH \geq 80\% \\ 0 & RH < 80\% \end{cases}$$

to estimate the cloud amount.

(b) For $(d\theta/dp)_{min} > -0.07(K/mb)$, we calculate the cloud amount as

$$CC = \begin{cases} (RH-80)^2/400, & \text{for } RH \leq 80\% \\ 0, & \text{for } RH \leq 80\%. \end{cases} \tag{4}$$

For the case with inversion we use $d\theta/dp = -0.1(K/mb)$. For comparison, we take the BOMEX undisturbed period when $d\theta/dp$ is $-0.11(K/mb)$ and cloud cover is about 50%. The relative humidity just below the inversion is at 91% and at the LCL it is 84%. In this case the Slingo formula predicts a cloud cover of 70% while our formula predicts 55% cloud cover. It can be seen that the

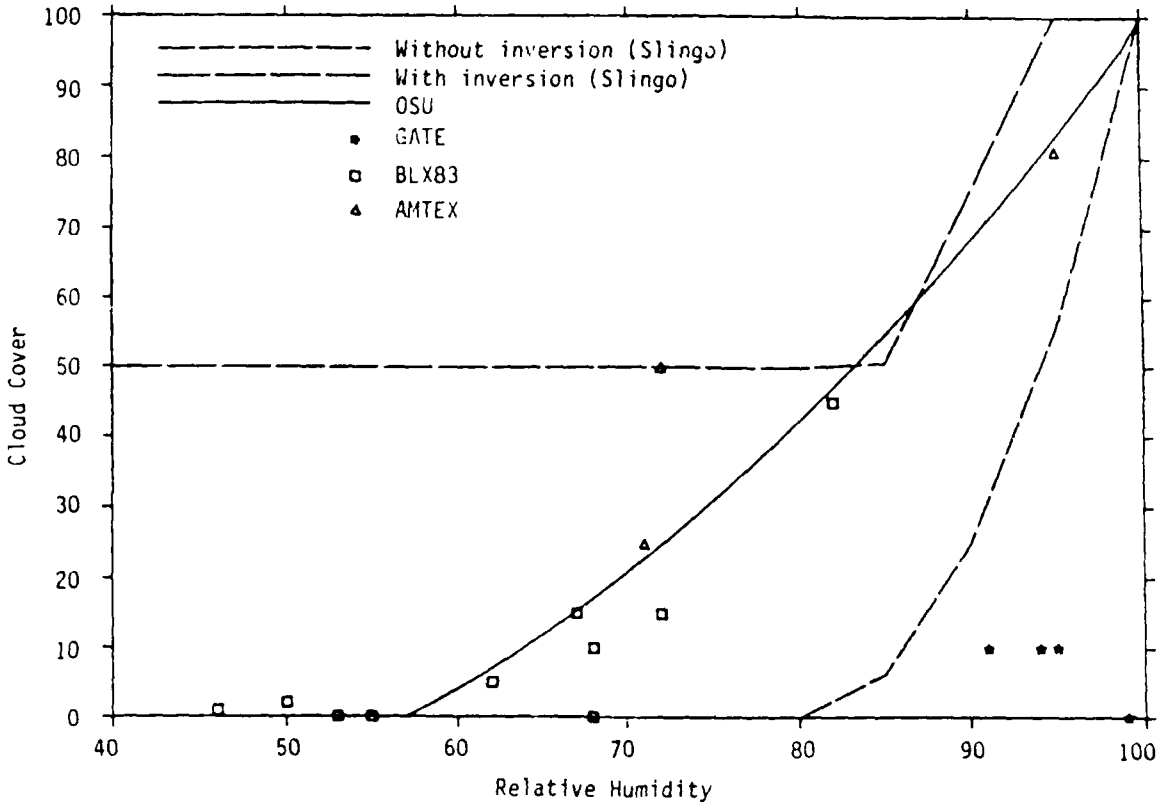

Figure 2. Comparison of the cloud cover prediction equations (Eqs. (2), (3) and (4)). For the Slingo scheme with inversion, we use $-d\theta/dp = 0.1$ (K/mb).

Slingo formula will overestimate the cloud amount in the presence of an inversion when the relative humidity falls below 80%.

Because the observed moisture fluxes from either budget studies (AMTEX and BOMEX) or aircraft measurements (California stratocumulus experiment reported in Albrecht, 1985) represent the combined fluxes from both the boundary layer turbulence and the shallow convection, we need to consider both mechanisms to model the observed fluxes. Within the framework of the PBL parameterization scheme, it is decided that a diffusion type parameterization scheme will be used to model the moisture flux due to shallow convection. We therefore seek to model the moisture flux $\overline{w'q'}$ as

$$\overline{w'q'} = -(K_h + K_c)\left(\frac{\partial \bar{q}}{\partial z} - \gamma\right) \tag{5}$$

where K_h is the coefficient of diffusivity due to boundary layer turbulence and K_c is the coefficient of diffusivity due to the shallow cumulus within the boundary layer. Furthermore, the boundary layer turbulent flux is calculated using the Troen and Mahrt (1986) method. The combined diffusivity $(K_h + K_c)$ (Fig. 3) is first calculated for each data set from profiles of $\overline{w'q'}$ and $\bar{q}$. We observe a peak in the lower boundary layer diffusivity profile. Troen and Mahrt (1986) demonstrated that the profile of K with a maximum at $z/h = 1/3$ fits the profile derived from large-eddy simulation experiments (Wyngaard and Brost, 1983). By assuming that the diffusivity coefficient for shallow convection (K_c) to be small near ground, we estimate the diffusivity coefficient for the boundary layer (K_h) using the profile of calculated K ($= K_h + K_c$) below .5 z/h. When a maximum K value is observed near the level $z/h = 1/3$, it is used to obtain a vertical profile of the K_h. We can further derive a diffusivity profile for the cloud (K_c) after subtracting K_h from K (see Fig. 4). We found that this profile can be approximately fitted by a Gaussian Distribution function (see Fig. 5a, b) if we know the peak value of this function and the standard deviation. Based on the observation that the ratio of the height of the Lifting Condensation Level (LCL) and the boundary layer height (h) is about 0.3 and that K_c approximately vanishes above $z/h = 1.2$, we thus parameterize the profile of cloud diffusivity as

$$K_c = K_{max} \exp[-(ZH - Center)^2/\delta^2], \quad 0.3 \leq ZH \leq 1.2 \tag{6}$$

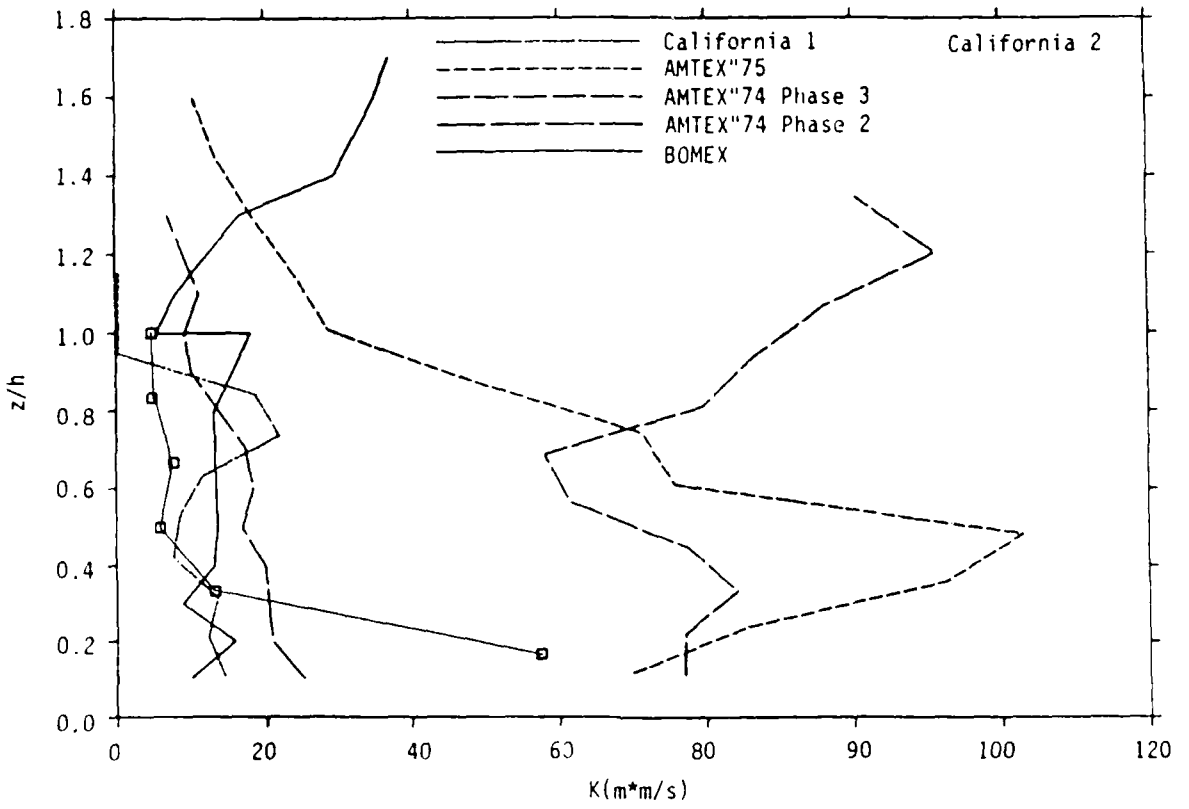

Figure 3. Vertical distribution of (K_c + K_h) calculated from the BOMEX, AMTEX and California coast stratocumulus experiment data.

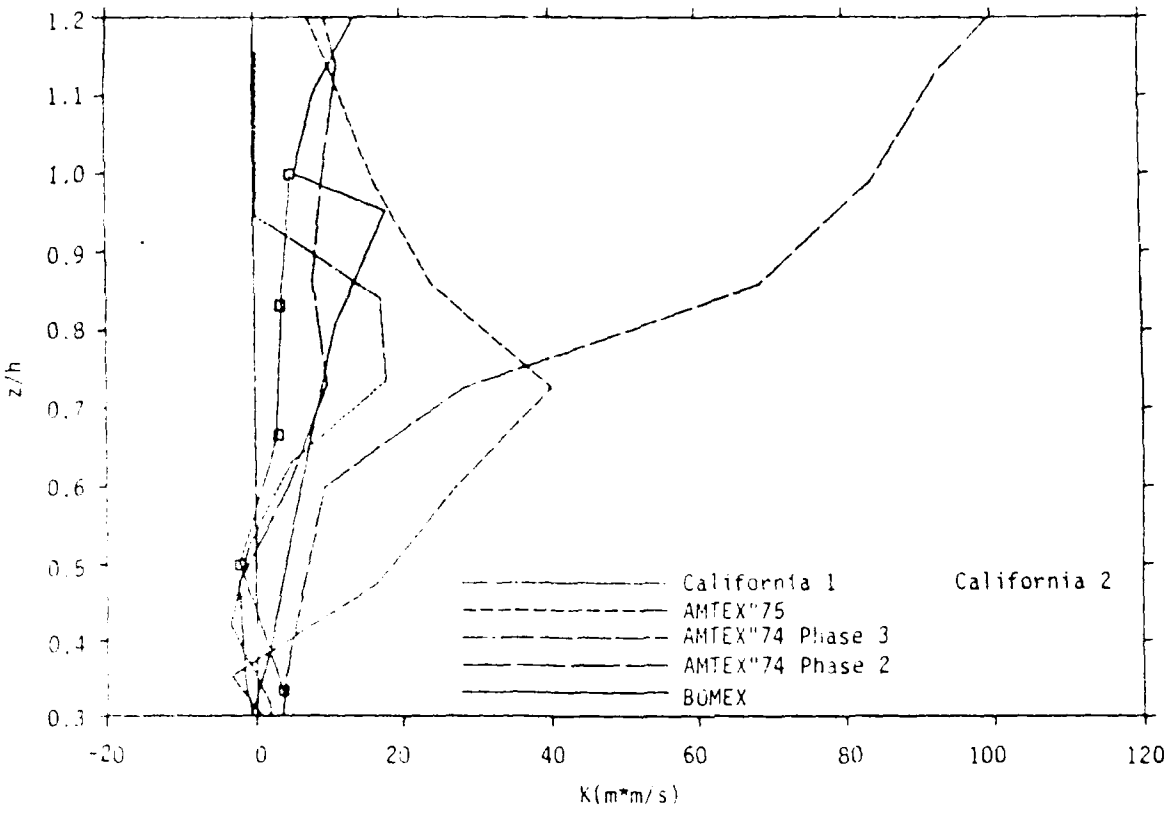

Figure 4. Vertical distribution of K_c deduced from the BOMEX, AMTEX and California coast stratocumulus experiment data.

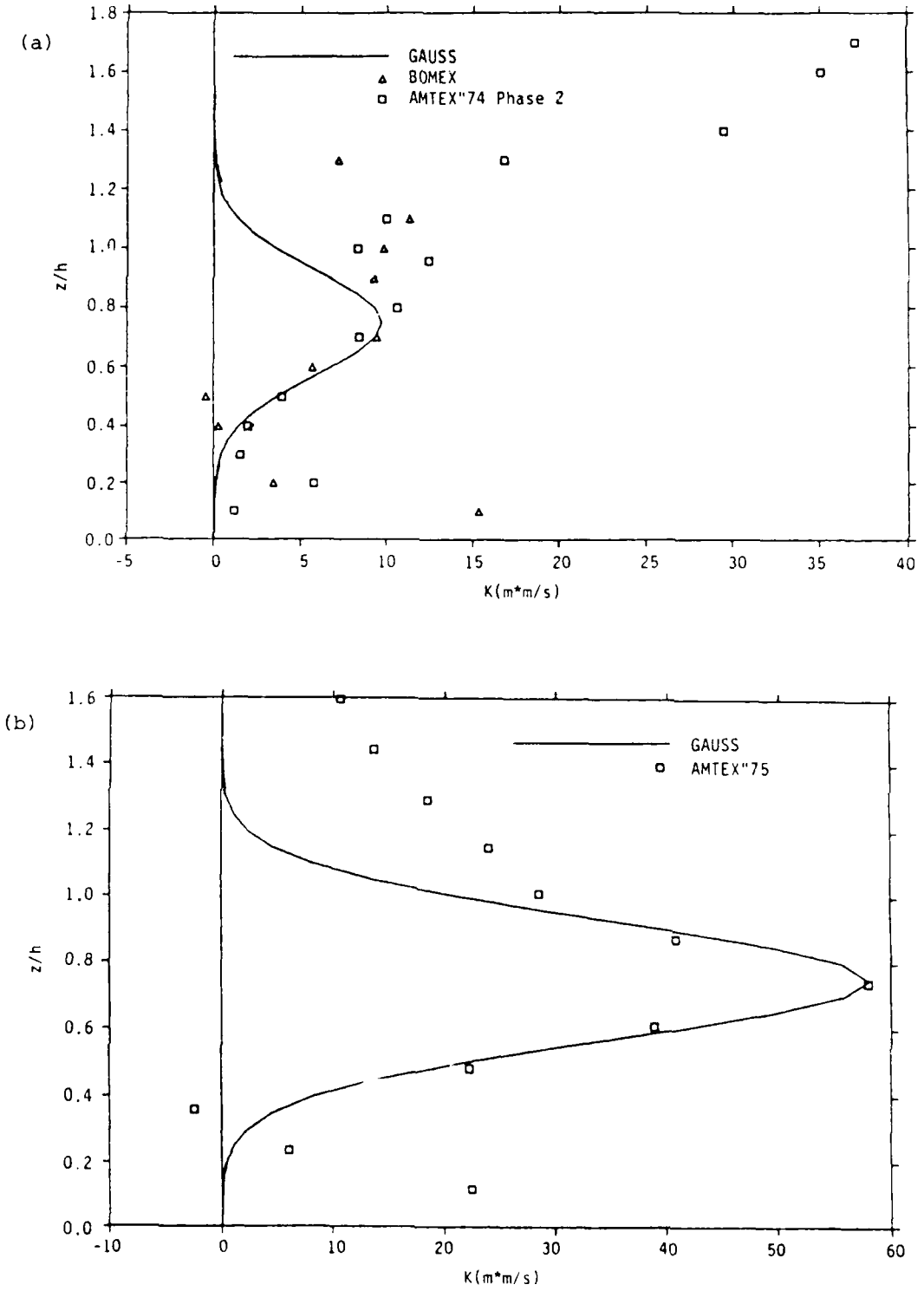

Figure 5. Examples of the best fit K profile calculated from observational data. (a) For the BOMEX, AMTEX74, (b) for the AMTEX75.

where

$$\delta^2 = (1.0 - \text{Center})^2 \quad ,$$

$$\text{Center} = Z_{max}/h \quad ,$$

K_{max} is the peak value, ZH is z/h, Z_{max} is the height where the maximum value took place, and Center is about 0.75 for the data we used here.

There are several parameters (stability, Richardson number, humidity, etc.) that have been tested to predict the magnitude of the variable K_{max}, but only the cloud cover is significantly related to K_{max}. The relationship between them can be fitted by a least-square linear equation (Fig. 6) as below:

$$K_{max} = A1 \cdot CC + A2, \text{ for } CC \geq 40\% \quad , \tag{7}$$

where A1 = 1.872 and A2 = -63.59. We further assume a linear relation for cloud cover less than 40% as follows:

$$K'_{max} = A3 \cdot CC \quad . \tag{8}$$

where A3 = 0.3555. Sensitivity experiments reveal that simulation results are insensitive to whether the K'_{max} term is included or not. It is probably because the term is usually quite small.

In order to apply the shallow convection parameterization in real data situations it is necessary that Eq. (6) can represent a variety situations when K_{max} may exist at different levels within the boundary layer. Since we are only interested in the physical process within the boundary layer, we assume that cloud diffusivity vanished when ZH is greater than 1.2 or smaller than 0.3. The ratio between the LCL height and the boundary layer height is close to the 0.3 in all cases we examined and the cloud top is usually about the same height as the boundary layer. Thus, we can rewrite δ^2 as a function of the LCL height by assuming that the distance between Z_{max} and LCL versus the distance between the boundary top and LCL is a constant ratio. We then arrive at the equation:

$$\text{Center} = z_{max}/h = 9/14 + 5/14 \cdot z_{lcl} \quad , \tag{9}$$

where Z_{lcl} is height of the LCL.

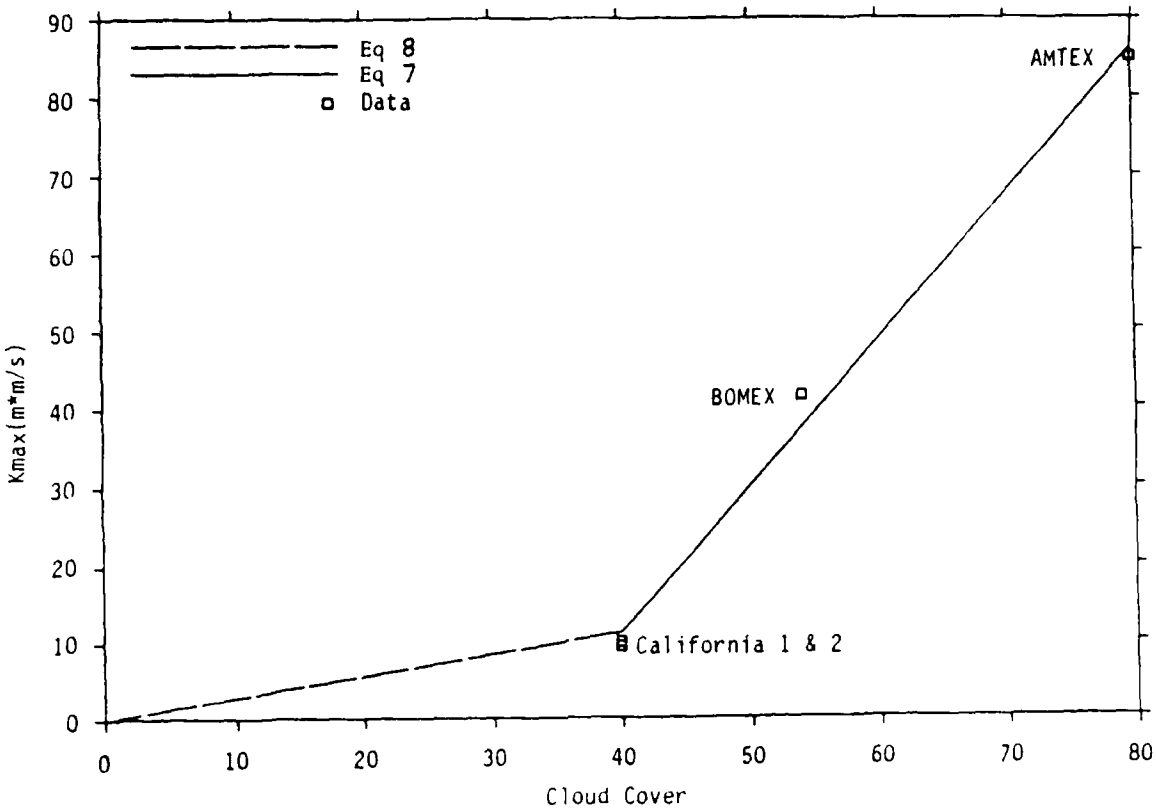

Figure 6. K_{max} vs. Cloud Cover plot of observational data and the least-square fit lines.

There are no similar treatments to the heat and momentum fluxes partly because it is not clear at the present how the cloud redistributes heat and momentum. Observational evidence seems to indicate that the effect of shallow cumulus on heat and momentum budget is weak. We are therefore neglecting them for the time being. Preliminary results show that if heat and momentum are similarly treated as moisture, boundary layer will grow and the inversion will be wiped out within a very short time period. Further studies are necessary to examine the effect of the shallow cumulus in the heat and momentum budget.

3.3. The ECMWF PBL and Shallow Convection Parameterization Scheme

The European Centre for Medium Range Weather Forecast (ECMWF) planetary boundary layer parameterization scheme (Louis, 1979) does not have an explicit treatment for unstable, stable or neutral boundary layer. It uses a Richardson number to determine each grid level's instability:

$$Ri = \frac{g \cdot dz \cdot d\theta}{\theta (dv)^2} \quad . \tag{10}$$

One then applies the following formula to compute the diffusion coefficient K_m and K_h

$$K_m = \ell^2 \left|dv/dz\right| F(Ri) \tag{11}$$

where

$$F(Ri) = \begin{cases} 1 - \dfrac{b \cdot Ri}{1 + c \left|Ri\right|^{1/2}}, & \text{unstable } (Ri < 0) \\ \dfrac{1}{(1 + b' \cdot Ri)^2}, & \text{stable and neutral } (Ri \geq 0), \end{cases}$$

$$\ell = \frac{k \cdot z}{1 + \dfrac{k \cdot z}{\lambda}}$$

and

$$c = C^* \frac{\ell^2 \cdot b \cdot \left[(z + dz)/z^{1/3} - 1\right]^{3/2}}{z^{1/2} \cdot dz^{3/2}} \quad .$$

The parameter F(Ri) is a stability function, k is the Von Karman constant (0.4 in this study), ℓ is the mixing length, λ is the asymptotic mixing length and is adjustable (currently being chosen as 100 m), b = 9.4, b' = 4.7 and C* is 7.4 for momentum and 5.3 for heat and moisture.

The shallow convection scheme used in Teidtke (1983) is quite simple. A constant diffusivity coefficient (25 m^2 s^{-1}) is assumed throughout the entire cloud deck for momentum, heat and moisture. The cloud base is assumed to be the condensation level for surface air and the cloud top is the level of non-buoyancy, but not higher than 750 mb. In the OSU PBL model the cloud top is determined where the relative humidity falls below 57% (Eq. 2).

4. Results

4.1. Real Data Simulations with the OSU Scheme

In this section we will present the results of a 1-D model simulation of the undisturbed trade wind situations and compare the simulated atmospheric profiles with and without the proposed shallow cumulus parameterization scheme to study the impact of the new scheme. The maintenance of the trade wind inversion is generally thought to be due to a balance between the large-scale sinking motion of the subtropical high-pressure system and the turbulent mixing within the boundary layer. To simulate this balance, it was necessary to include the observed vertical motion in the simple 1-D model. Without large-scale advection, however, the model predicted temperature field near the surface will in time approach the temperature at the sea-surface. The virtual heat flux from the ocean and the boundary layer turbulence will both be reduced. These results will eventually lead to the collapse of the boundary layer. Given this inherent limitation of the 1-D model, we will only present short-range (1-2 days) mode simulations.

For a given initial profile of wind, temperature and moisture, we keep the model top level wind field and the entire vertical motion field fixed with time and allow boundary layer mixing to modify the rest of the parameters. Because the observed atmospheric profiles are usually stably stratified, the simulated boundary layer will grow vertically as turbulent mixing starts. We will refer to the initial state as the time 0 state and the predicted state by the number of hours from the initial time. In addition to the temperature and dew-point profiles, we will also display the saturation point (SP) profile (Betts and Miller, 1984). When the SP profile is close to a straight line, as is often observed, the atmosphere is well-mixed. In the 1-D model, turbulent and shallow cumulus mixing are the only mechanisms that can modify the SP profile. We have found the SP profile to be a good tool to examine the effect of the parameterization schemes.

Figures 7 and 8 show the model predicted atmospheric profiles using BOMEX June 22 to June 26 average sounding as the initial state after one 12-hour run with and without the shallow convection. By comparing these figures we find that, after 12 hours, both cases maintain a well-defined inversion at the top of the boundary layer. This is because sinking motion is warming the top of

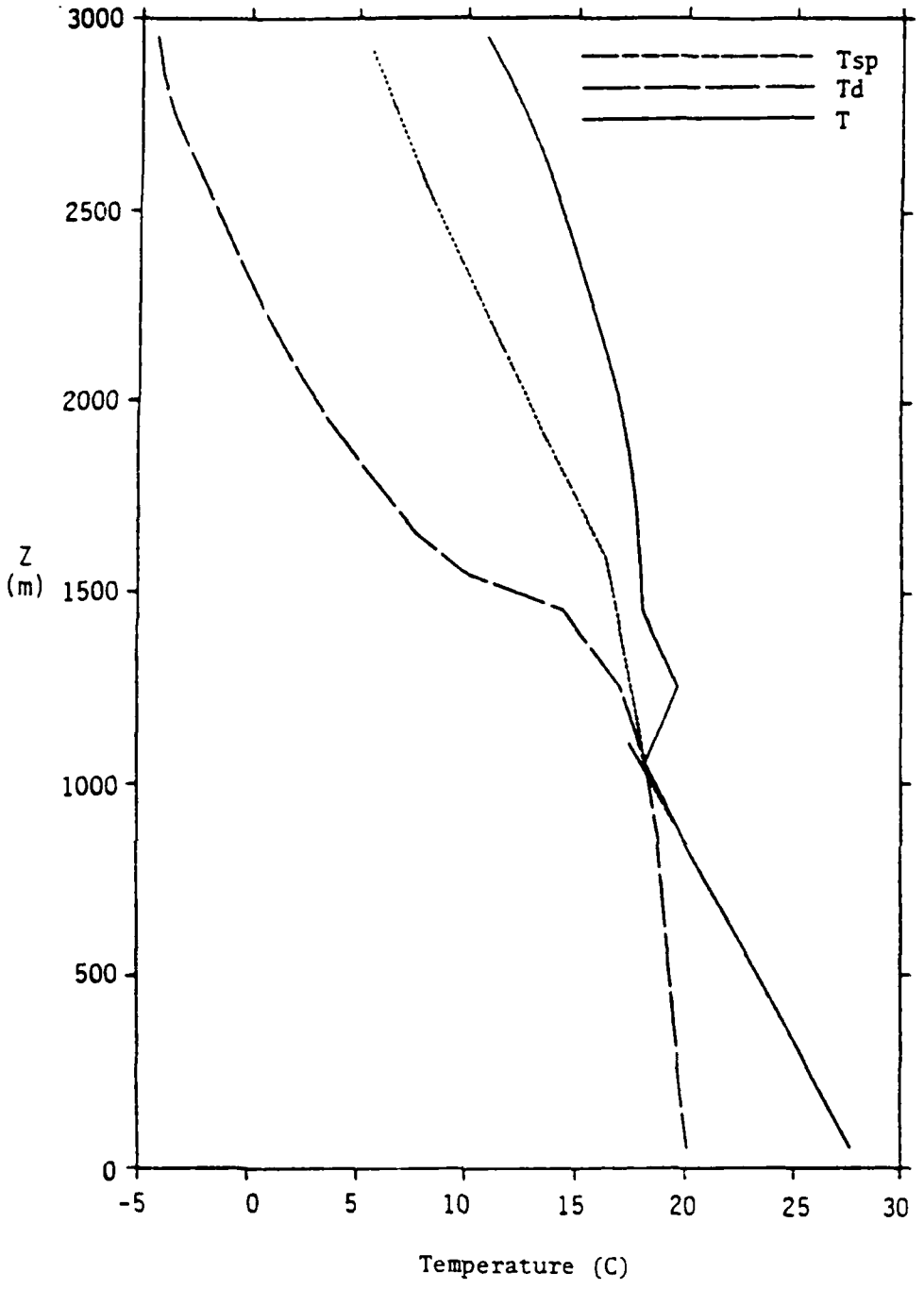

Figure 7. Temperature, dew point and saturation point profile for the BOMEX case with the OSU shallow convection scheme at hour 12.

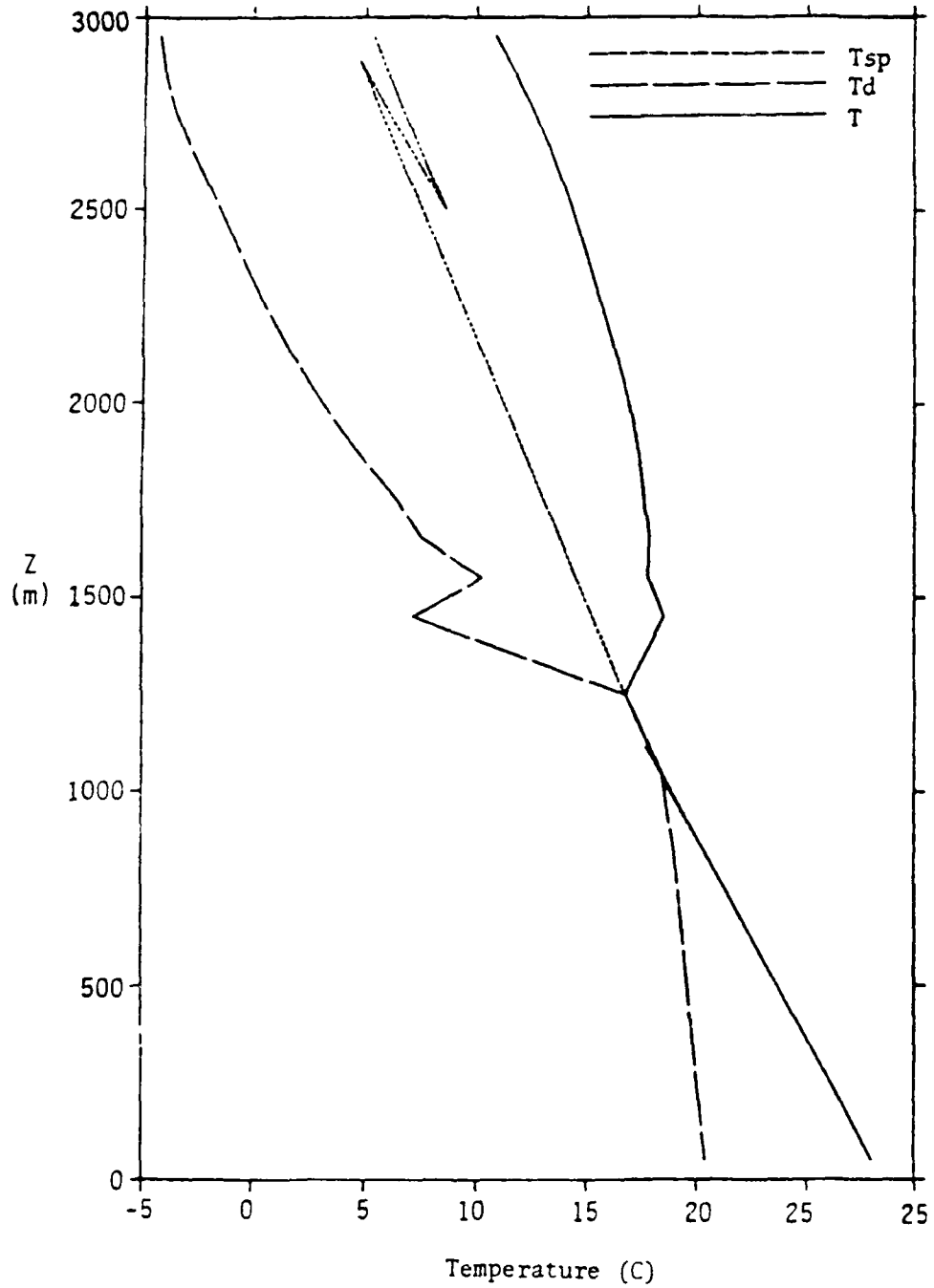

Figure 8. Temperature, dew point and saturation point profile for the BOMEX case without the OSU shallow convection scheme at hour 12.

the inversion and cooling the upper part of the boundary layer (discussion about the cooling will be given in section 4.2).

The temperature profiles in both Figs. 7 and 8 are very close to dry-adiabatic. The dew-point profiles fall closely on a constant mixing-ratio line. The boundary layer coefficient of diffusivity formulation slightly overestimates the mixing near the top of the boundary layer and results in a mixing ratio profile that increases slightly with height above 500 m. Above the boundary layer, the large scale sinking motion is adiabatic and does not alter the SP character so that the environmental SP profiles are maintained. The effect of the shallow cumulus parameterization is quite small at this time. When shallow cumulus is parameterized, the enhanced diffusion will transport more moisture into the upper boundary layer and, in fact, will transport some moisture above the inversion. This is designed to simulate the penetrating tops of some of the cumulus that can exist above the inversion.

Above 1.5 km, the model structures are identical as they should be. The boundary layer is significantly deeper for the case without shallow cumulus (1.3 km) than with cumulus (1.0 km). This is because the cloud moisture diffusivity above the boundary layer top (h) mixes the dry stable air into the boundary layer and creates a deeper transition layer below the inversion top. Between the inversion base and 1.5 km, the model with shallow cumulus (Fig. 7) is actually moistened while the model without shallow cumulus (Fig. 8) actually dries out because of imperfect vertical advection (an upstream scheme is applied and the constant sinking motion has a maximum below 1.5 km).

The boundary layer in the 1.0 - 1.3 km interval is saturated for the run without shallow cumulus (Fig. 8). This result demonstrates that the parameterized boundary layer mixing alone is capable of transporting significant amounts of moisture into the upper boundary layer. This also can be see from the model diagnostic Q2 profiles shown in Fig. 9 where the moisture flux convergence beyond one hour near the top of the boundary layer is greater in the case without shallow convection than with shallow convection. This is because in the latter case the dryer air is mixed down from above the top of the boundary layer and moisture is transported out of the boundary layer; this can prevent moisture from accumulating in the upper boundary layer. For this

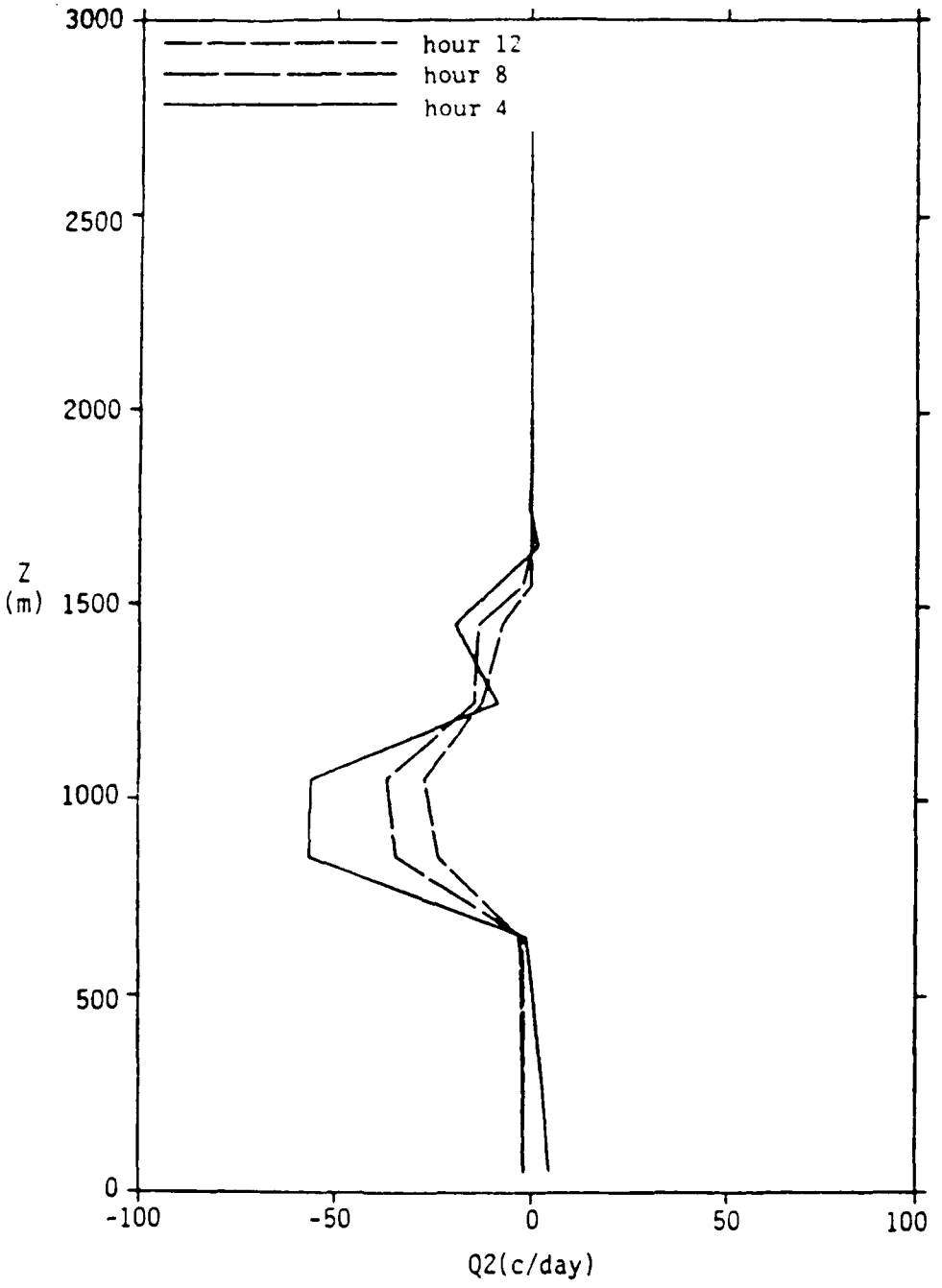

Figure 9. Model diagnostic Q2 profiles for the BOMEX case at hours 4, 8, 12. (a) With the OSU shallow convection scheme, and (b) without the OSU shallow convection scheme.

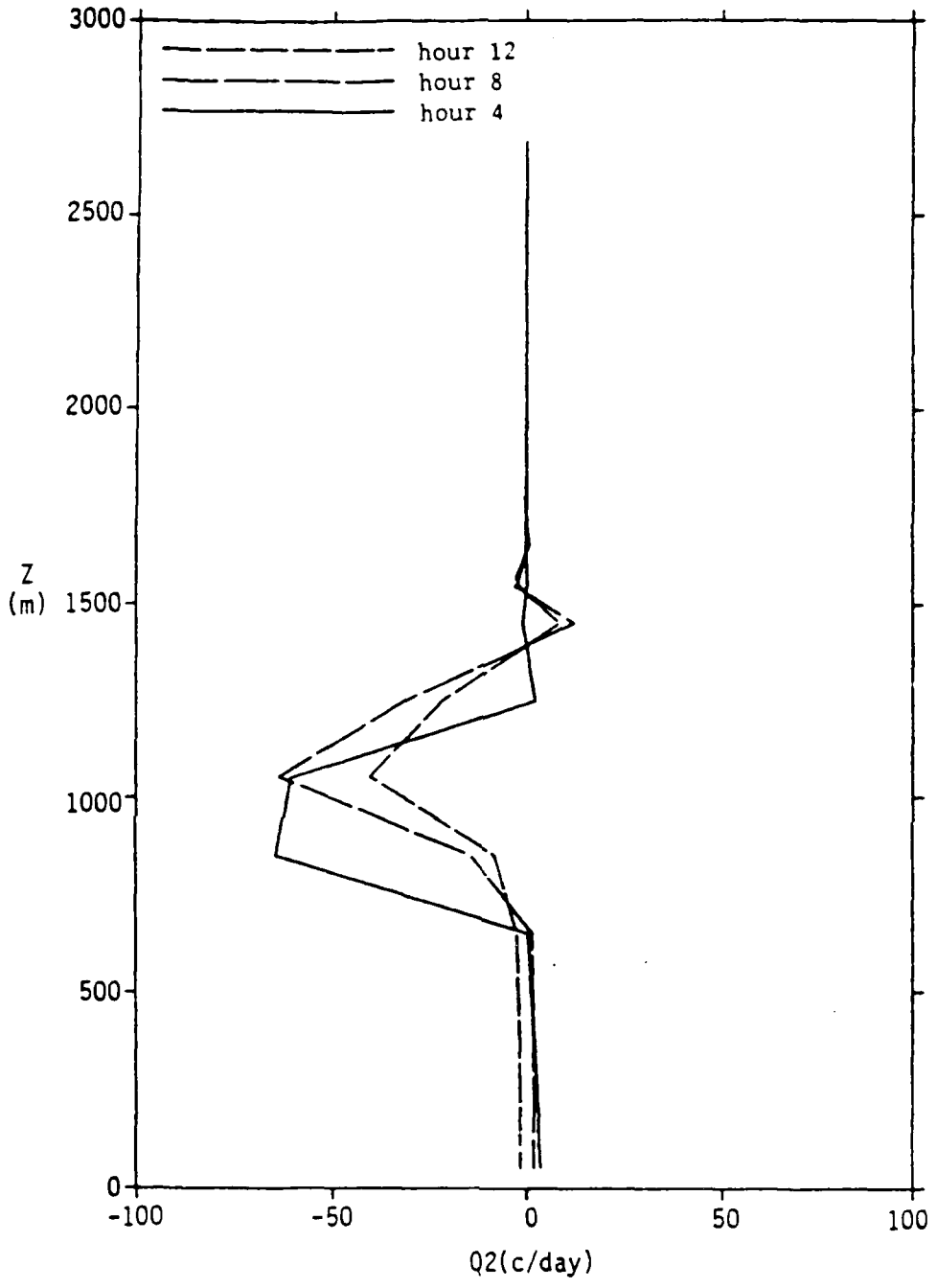

Figure 9. (Continued)

run the predicted cloud cover for both cases is reasonable (the averaged amount is about 50% compared to 45% for the observation).

4.2. Comparison with Observations

Judging by the moisture flux profiles deduced from the observed Q2 profiles, shallow convection indeed has had an influence on the environment. In the 1-D model, we also notice differences in the SP profiles when shallow cumulus is parameterized indicating changes in the environment. The model results further demonstrate that the often observed minimum in the Q2 profiles (Fig. 10) near the base of the inversion is due to the convergence of boundary layer turbulent flux as well as due to shallow convection. In cases when the cloud amount is small, boundary layer turbulent mixing can explain all or most of the observed Q2 profile. When shallow cumulus is included in the 1-D model, the predicted minimum in Q2 is nearly twice the observed minimum in magnitude. This result can be explained by the fact that the model-predicted moisture profiles become saturated after a few hours. As the moisture gradient across the inversion increases, the parameterized turbulent moisture flux also increases. In a recent effort to include the OSU boundary layer model in a global spectral primitive-equation model (to be reported elsewhere), the boundary layer structure over the ocean is closely monitored and is rarely found to be saturated. It is obvious that mechanisms such as horizontal advection, convective heating and large-scale precipitation are also important in determining the boundary layer moisture profiles.

In Table 2 we list the surface latent heat flux and virtual heat flux at hour 12 from the model calculation for the three data sets (unit is W m^{-2}).

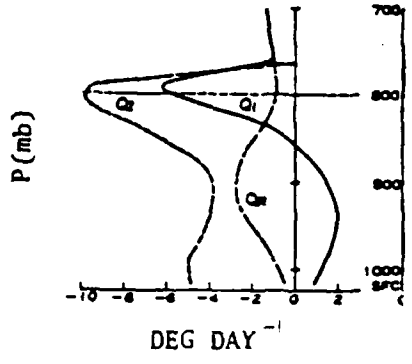

Figure 10a Vertical profiles of large-scale apparent heat source Q1, apparent moisture sink Q2, radiation heating QR for AMTEX during 14-16 Feb. 1974. Thin dashed line denotes the inversion base.

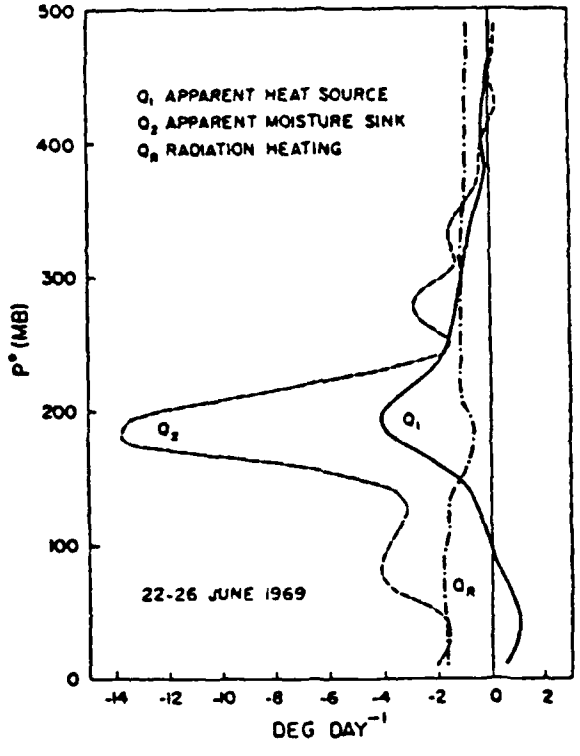

Figure 10b Vertical profiles of apparent heat source Q1, apparent moisture sink Q2, and radiation heating for the BOMEX undisturbed period.

Table 2. Summary of the surface latent heat and virtual heat flux simulated with the OSU scheme. (Note: * represents without shallow convection.)

	Virtual heat flux ($W\ m^{-2}$)	Latent heat flux ($W\ m^{-2}$)
BOMEX	13 (9)*	194 (188)*
AMTEX	155 (153)*	675 (648)*
GATE	3*	55*

Comparing the model results with the observations (Table 1), we find that in general the model generates higher latent heat flux and lower sensible heat flux. This is because saturated sounding results in an overestimation of the cloud cover and enhancement of the cloud diffusivity as well as the surface moisture flux. The virtual heat flux is slightly underestimated. Because the potential temperature increases with height, enhancing the heat transport due to shallow cumulus would lead to a warmer temperature in the lower boundary layer. This would further reduce the sensible heat transport lending further support for not parameterizing the heat transport. The increase in the virtual heat flux with shallow cumulus (Table 2) is due to an increase in the turbulent moisture transport which results in a slightly drier lower boundary layer and a higher evaporation rate from the ocean.

In the AMTEX simulation both fluxes are overestimated at hour 12 and in the GATE case both fluxes are underestimated. However, as discussed in the previous section, for the AMTEX data set, the model takes 12 hours to adjust itself toward a steady state. After that the surface moisture flux became 302 $W\ m^{-2}$ and sensible heat flux became 37 $W\ m^{-2}$. For the GATE data set, the model does not include the cumulus effect because the LCL is above the boundary layer.

4.3. Comparison with the ECMWF Scheme

Here we would like to compare the boundary layer parameterization scheme and the shallow convection scheme with the ECMWF schemes. Unlike our boundary

layer parameterization scheme, the Louis formula used in the ECMWF model depends only on the Richardson number [Eq. (10)]. It is not necessary for the diffusivity coefficients K_m or K_h [Eq. (11)] to go to zero near h (top of the boundary layer), although the normal stability of the atmosphere is such that the K_m and K_h become very small above the boundary layer.

A recent ECMWF report (Louis et al., 1981) shows two modifications of the Louis formula which may increase the boundary layer turbulent mixing because, in day-to-day diagnostic of the global operational model, it became apparent that the model suffers from a lack of boundary layer mixing. The first modification includes a larger asymptotic mixing length (λ) of 300 m to increase the K_m and K_h. The second modification not only slightly changes the formulation but also increases the asymptotic mixing length to 400 m for heat and moisture. The modification is in response to artificial cooling of the stratosphere generated by the model and strong weakening of the jet stream in the model integrations. Essentially, the increased asymptotic mixing length for the heat and moisture will enhance the turbulent mixing processes and redistribute the heat and moisture into higher region. Furthermore, Tiedtke (1983) developed a simple shallow convection scheme for ECMWF in response to deficiencies found in global integrations which is attributed to a lack of shallow convection.

In order to illustrate the difference between the OSU and the ECMWF boundary layer parameterization scheme, the coefficients of diffusivity using both models are presented in Fig. 11 (first modification of the Louis scheme is used for ECMWF). The initial state is the BOMEX case and the ECMWF scheme is used to predict for 24 hours. At hour 24 the coefficient of diffusivity based on our scheme is also calculated. It can be seen that the OSU parameterization scheme produces a profile of K_h that is about an order of magnitude greater than that from the ECMWF scheme. In addition, the K_h from the ECMWF scheme vanishes above .7h (the boundary layer height determination is based on the OSU scheme). This is a result of the chosen asymptotic mixing length that produces a maximum for K_h around 300 m. Stronger mixing in the OSU scheme leads to warmer and drier surface air. This induces larger surface latent heat and sensible heat fluxes.

Here we implement both Louis' and Tiedtke's schemes in our boundary layer routine. Figures 12 and 13 are the result from BOMEX initial state. Each

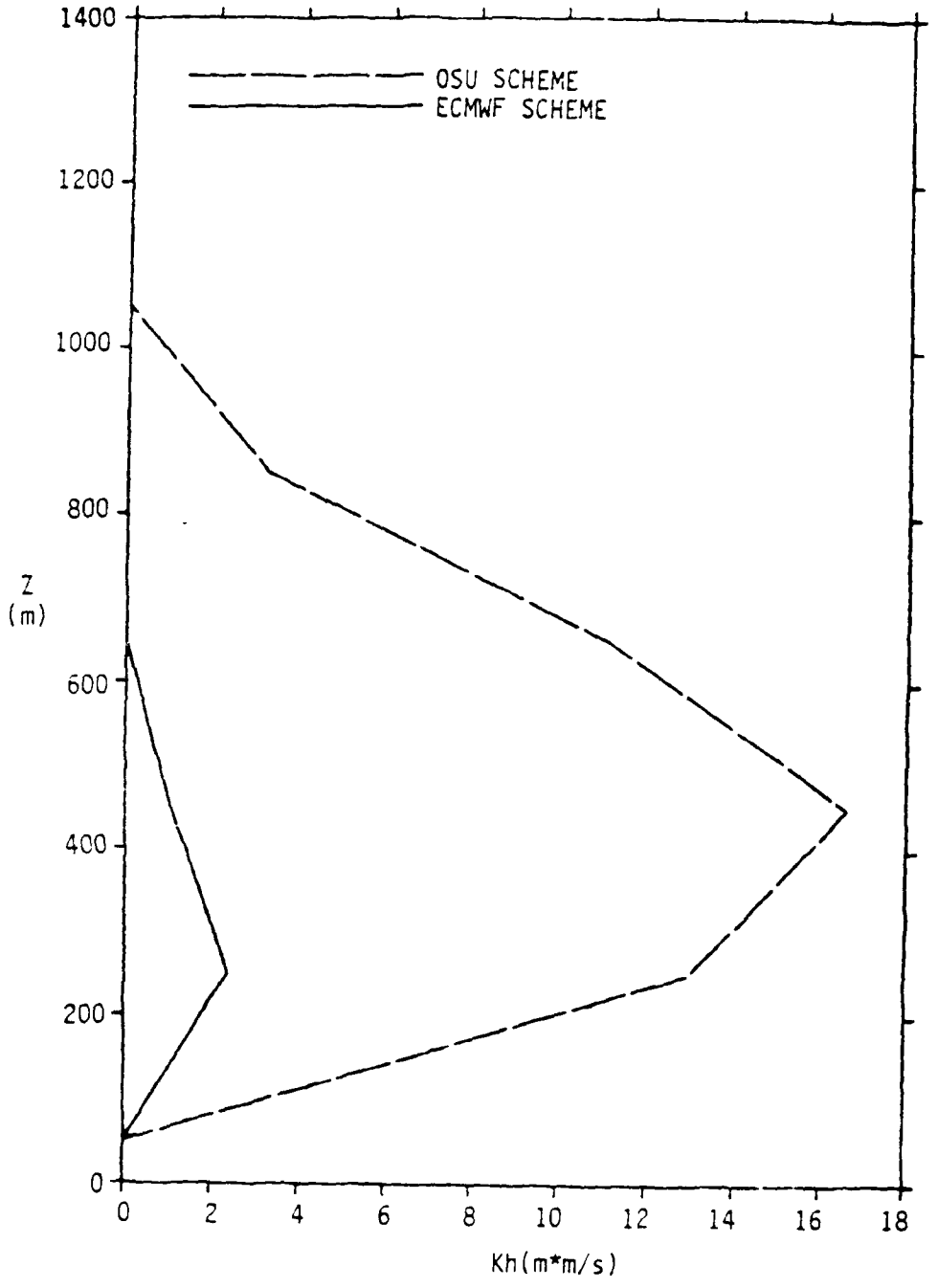

Figure 11. Vertical profile of the moisture diffusion coefficient for the OSU (dash line) and the ECMWF (solid line) schemes.

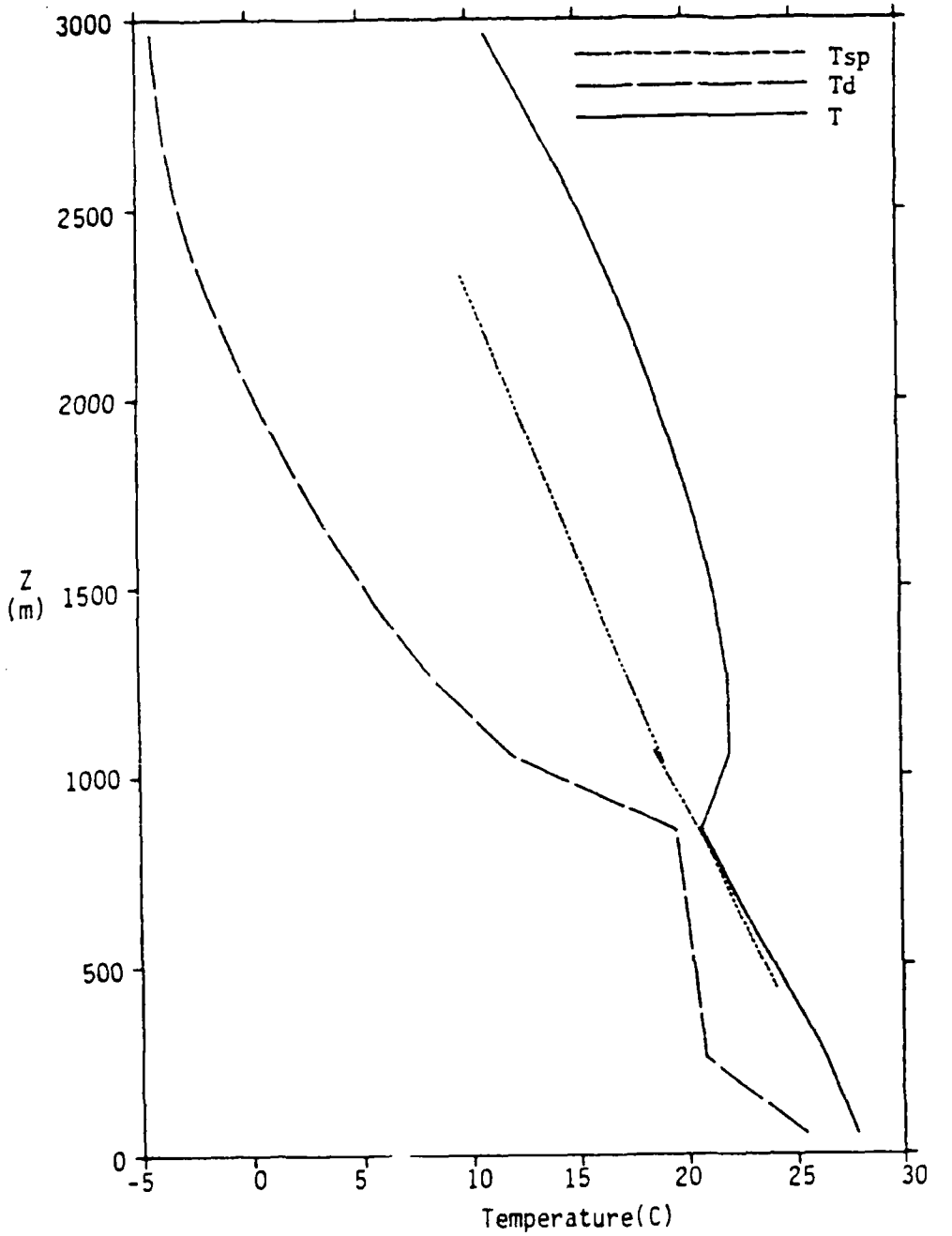

Figure 12. Temperature, dew point and saturation point profile for the BOMEX case with the ECMWF shallow convection scheme at hour 12.

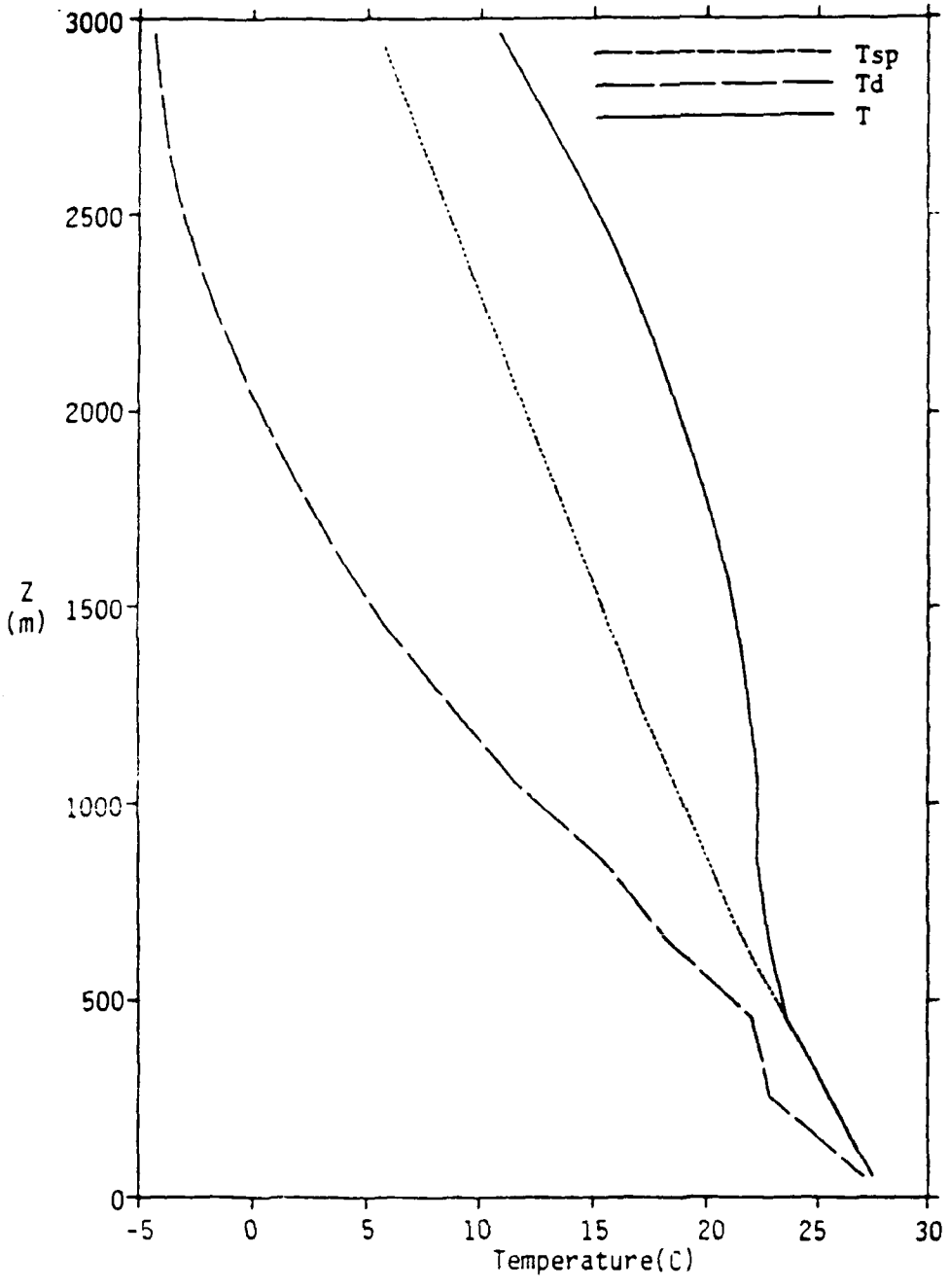

Figure 13. Temperature, dew point and saturation point profile for the BOMEX case without the ECMWF shallow convection scheme at hour 12.

of these runs uses asymptotic mixing length of 300 m. Due to the weak turbulent mixing process as was shown above, it takes more than 24 hours for both ECMWF schemes to adjust the boundary layer structure from the initial state to well-mixed. Compared to our result (less than one hour can result in a well-mixed lower boundary layer) the turbulent mixing for ECMWF scheme is relatively weak and slow. Hence we display model structures at hour 36. Table 3 lists the results at hour 36 from the ECMWF scheme.

Table 3. Summary of the surface latent heat and virtual heat flux simulated with the ECMWF scheme. (Note: * represents without shallow convection.)

Data	Virtual heat flux ($W\ m^{-2}$)	Latent heat flux ($W\ m^{-2}$)
BOMEX	1.5 (0.9)*	32 (18)*
GATE	0.45 (0.42)*	17 (13)*

The characteristics of the simulated BOMEX model structure are: 1) the predicted boundary layer height is lower, 2) a steady state structure can not be maintained for very long, and, 3) the upper boundary layer is not saturated with or without the shallow convection. With the shallow convection a well-defined inversion layer is obtained. Folding of the SP's profile above the inversion indicates the transition from the moist surface layer to the dryer mixed layer, but this is not very clear for the cases without the shallow convection due to the weaker turbulent mixing.

Closer examination of the potential temperature (θ) and mixing ratio (q) profile can reveal more detail of the boundary layer model structure. For example, for the BOMEX case at hour 36 a deep mixed layer with a top at 800 m is created with shallow convection; this is roughly twice the depth simulated without the shallow convection. Unlike our deeper and totally well-mixed boundary layer model structure at hour 12 (see Fig. 8), the ECMWF result within the boundary layer shows a thick moist surface layer below 250 m which explains their smaller simulated surface virtual heat flux and latent heat flux (Table 3).

Down-wind of the trade wind cumuli is the typical area where we can see the deep cumulus. It is very important to the development of the down-wind deep convection to transport moisture from the surface to the upper boundary layer. With the ECMWF scheme, however, moisture is trapped in the lower boundary layer and cannot be transported to the higher region without the shallow convection. A comparison of Fig. 13 to Fig. 8 shows that the dew point decreases rapidly above 500 m for the ECMWF scheme, while our scheme simulates a 1.1 km depth well-mixed layer with a nearly constant dew point. This may be the reason why the ECMWF global model needs the shallow convection to set up a deeper mixed-layer and enhance the surface turbulent fluxes. In Fig. 8 our result indicates that the shallow convection only slightly increases the moisture above 1.3 km and the profile below that level is not changed. But from the potential temperature point of view, the shallow convection creates a deeper transition layer above the boundary layer and the top of the boundary layer becomes lower.

The primary difference between the schemes can be seen in the model diagnostic Q2 profiles at hour 36. For the BOMEX case (Fig. 14), the Q2 profile without shallow convection shows a large moisture flux convergence near the surface and a weaker one at the top of the mixed layer (400 m). When shallow convection is included the Q2 profile shows only one minimum at the mixed layer top (800 m). This means the modeled shallow cumulus is working to prevent moisture from accumulating near the surface and to transport it from the lower boundary layer to the mixed layer top. This also enhances the surface sensible and latent heat transport. Comparing the case with shallow convection to our result (which essentially is without shallow cumulus), we find that both have a minimum point at 250 m and the magnitude is slightly larger for the OSU model.

For the BOMEX case with shallow convection, the ECMWF scheme has a reasonable Q2 minimum compared to the observation. The boundary layer top (h) is much lower and the minimum point of the Q2 profile is found at the top of the mixed layer instead of the boundary layer top. However, the simulated thick moist surface layer is not observed in the real data. In contrast, our simulation has a deeper and well-mixed boundary layer (which is close to the observation) and a slightly overestimated moisture flux at the top of the boundary layer.

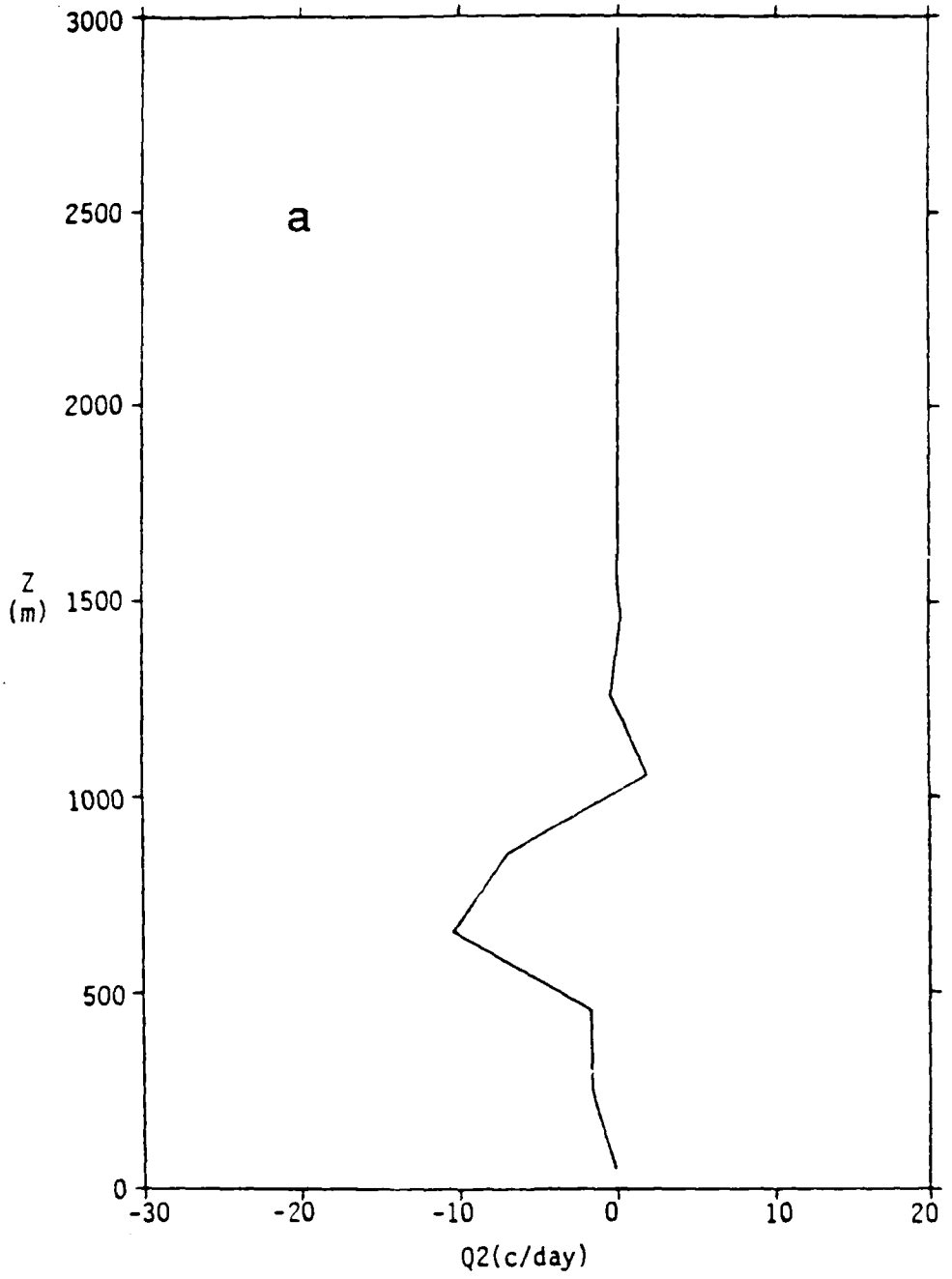

Figure 14. Predicted model diagnostic Q2 profiles for the BOMEX case at hours 4, 8, 12. (a) With the ECMWF shallow convection scheme, and (b) without the ECMWF shallow convection scheme.

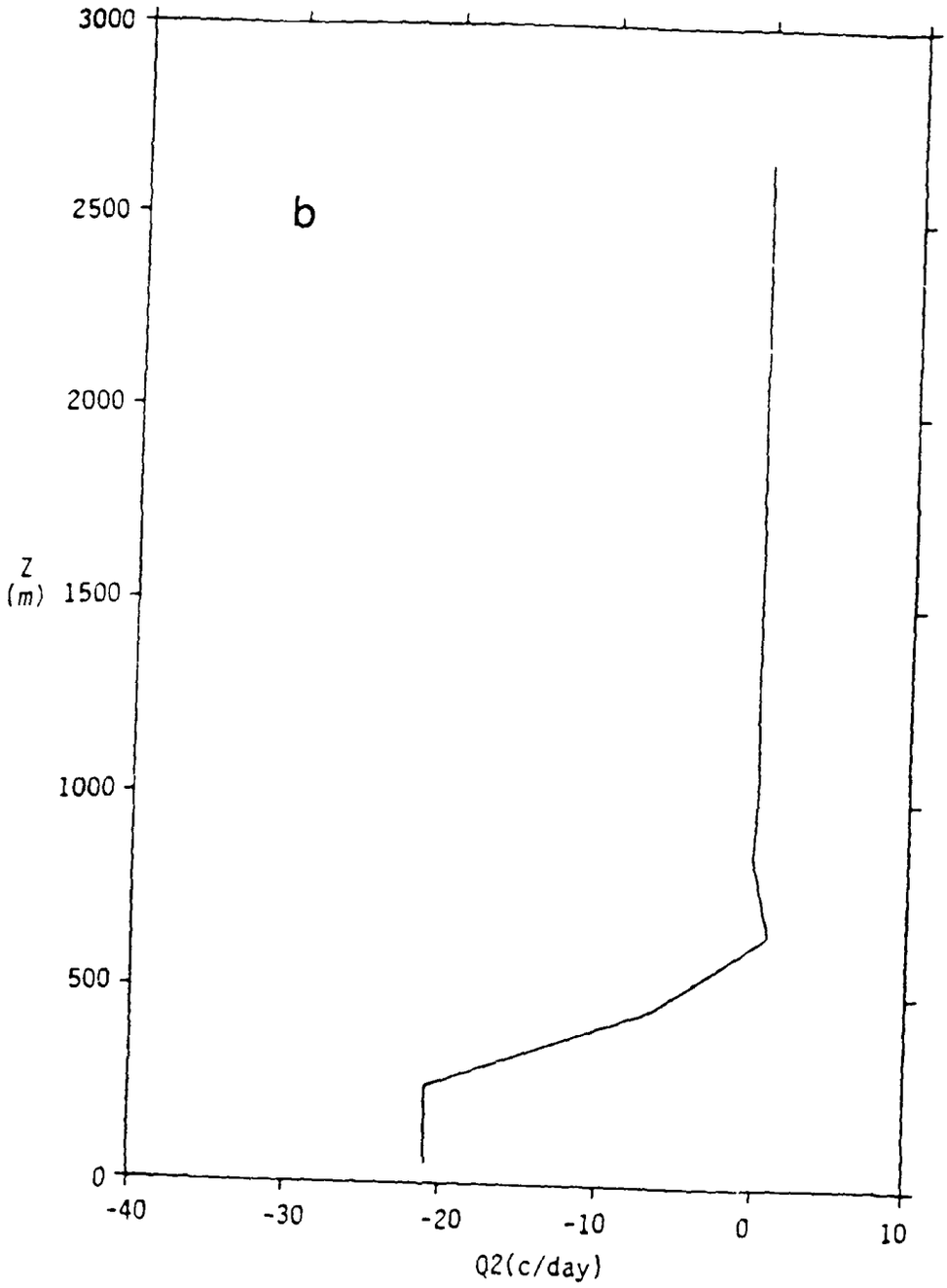

Figure 14. (Continued)

From the above discussion one can see that the role of the shallow convection is crucial to the ECMWF model because the boundary layer mixing is too weak. By including the shallow convection in the model, the turbulent mixing is still not capable of reproducing the state that is close to the real data. These are due to the constraint of the asymptotic mixing length that prevents moisture and heat from being mixed higher into the atmosphere.

5. Conclusion and Discussion

The ECMWF global prediction model is considered by many the state-of-the-art weather prediction model at the present. It is the result of recent model diagnosis from the ECMWF that led to our interest in modeling the shallow cumulus. However, results based on our boundary layer parameterization scheme are quite different from the ECMWF experience. We find that our boundary layer parameterization can mix moisture into the upper troposphere and create the observed Q2 profile while the ECMWF scheme cannot. The results indicate that the primary mechanism that transports moisture away from the lower atmosphere is the boundary layer turbulent flux. The boundary layer turbulent mixing alone is capable of maintaining an apparent moisture source near the inversion. While the sensible heat flux over the ocean becomes quite small after a few hours, the virtual heat flux remains positive and the boundary layer remains in the unstable regime.

Due to the constraint of the asymptotic mixing length, we have found the ECMWF boundary layer mixing is restricted to the lowest 500 m of the boundary layer. Even with recent modifications, the boundary mixing is still extremely small above 500 m. It is possible that the use of the diffusivity coefficient formula derived for a neutral boundary (Blackadar, 1962) in unstable situations may be inappropriate.

The effect of the shallow convection scheme in our 1-D model is to enhance the boundary layer turbulent mixing and the surface turbulent fluxes and to reduce moisture flux convergence near the top of the boundary layer by mixing the air within the boundary layer with the free atmosphere. For the ECMWF model, the shallow convection scheme significantly improves the model results by enhancing the surface turbulent fluxes as well as the moisture flux convergence.

It is necessary to derive a proper boundary layer parameterization scheme before one tries to study the importance of the trade wind shallow cumulus. Without doing so one can be very easily misled by the results and would have a wrong picture of the problem.

This study is primarily focused on the trade wind shallow cumulus. In the future we would like to see the effect of the boundary layer and shallow convection scheme over other areas (e.g., over land situation) and would also like to focus on its impact on the 3-D model.

REFERENCES

Albrecht, B. A., R. S. Penc and W. H. Schubert, 1985: An observation study of cloud-topped mixed layers. J. Atmos. Sci., 42, 800-822.

Arakawa, A., and W. H. Schubert, 1974: Interaction of a cumulus cloud ensemble with the large-scale environment: Part I. J. Atmos. Sci., 31, 674-701.

Betts, A. K., 1978: Saturation point analysis of moist convection overturning. J. Atmos. Sci., 39, 1484-1505.

Betts, A. K., 1982: Cloud thermodynamic models in saturation coordinates. J. Atmos. Sci., 39, 2182-2191.

Betts, A. K., and M. J. Miller, 1984: A new convective adjustment scheme. ECMWF Technical Report No. 43.

Blackadar, A. K., and H. Tennekes, 1962: Asymptotic similarity in neutral barotropic planetary boundary layers. J. Atmos. Sci., 25(6), 1015-1020.

Brenner, S., C.-H. Yang and K. Mitchell, 1984: The AFGL global spectral model: Expanded resolution baseline version. Report No. AFGL-TR-84-0308, 72 pp. [Air Force Geophysics Laboratory/LYP, Hanscom AFB, MA 01731, USA.] ADA160370

Esbensen, S., 1975: An analysis of subcloud layer heat and moisture budgets in the western Atlantic trades. J. Atmos. Sci., 32, 1921-1933.

Kuo, H.-L., 1965: On formation and intensification of tropical cyclones through latent heat release by cumulus convection. J. Atmos. Sci., 22, 40-63.

LeMone, M. A., and W. T. Pennell, 1976: The relationship of trade wind cumulus distribution to subcloud layer fluxes and structure. Mon. Wea. Rev., 104, 524-539.

Louis, J. F., 1979: A parametric model of vertical eddy fluxes in the atmosphere. Bound.-layer Meteor., 17, 187-202.

Louis, J. F., M. Tiedtke and J. F. Geleyn, 1981: A short history of the operational PBL-parameterization at ECMWF. (Lecture given by J. F. Geleyn.) ECMWF Worksh on Planetary Boundary Layer Parameterization, 25-27 Nov. 1981, 59 pp.

Murty, L. K., 1976: Heat and moisture budgets over AMTEX area during AMTEX'75. J. Meteor. Soc. Japan, 54, 370-381.

Nicholls, S., and M. A. LeMone, 1980: The fair weather boundary layer in GATE: The relationship of subcloud fluxes and structure to the distribution and enhancement of cumulus clouds. J. Atmos. Sci., 37, 2051-2067.

Nitta, T. S., 1976: Large-scale heat and moisture budges during the air mass transformation experiment. J. Meteor. Soc. Japan, 54, 1-14.

Nitta, T. S., and S. S. So, 1980: Structure and heat, moisture and momentum budgets of a convective mixed layer during AMTEX'75. J. Meteor. Soc. Japan, 58, 378-393.

Pan, H.-L., and L. Mahrt, 1987: Interaction between soil hydrology and boundary-layer development. Bound. Layer Meteor., 38, 185-202.

Slingo, J. M., 1980: A cloud parameterization scheme derived from GATE data for use with a numerical model. Quart. J. Met. Soc., 106, 747-770.

Stull, R. G., and E. W. Eloranta, 1984: Boundary Layer Experiment 1983. Bull. Amer. Meteor. Soc., 65, 450-456.

Tiedtke, M., 1983: The sensitivity studies of the time-mean large-scale flow to cumulus convection in the ECMWF model. ECMWF Workshop on Convection in Large-Scale Models, 28 Nov. - 1 Dec. 1983, 297 pp.

Troen, I., and L. Mahrt, 1986: A simple model of the atmospheric boundary layer: Sensitivity to surface evaporation. Bound. Layer Meteor., 37, 129-148.

Wyngaard, J. C., and R. A. Brost, 1983: Top-down and bottom-up diffusion in the convection boundary layer. J. Atmos. Sci., 41, 102-112.

Yanai, M., S. Esbensen and J.-H. Chu, 1973: Determination of bulk properties of tropical cloud clusters from large-scale heat and moisture budgets. J. Atmos. Sci., 30, 611-627.

CHAPTER VII: CONCLUSIONS

The work under the present contract has concentrated on improvements of generic problems in boundary-layer modelling such as transport induced by shallow cumulus, subgrid variations of surface fluxes, the unique behavior of transport within the very stable boundary layer and interaction between soil hydrology, evapotranspiration and boundary-layer development. This work is described in some detail in the current report and, except for the shallow cumulus effort (see discusion below), is either already published or soon will be submitted for publication in major journals.

The present work has attempted to develop physically-motivated formulations which avoid practical, but *ad hoc*, corrections. We therefore anticipate, without proof, that our new formulations for shallow cumulus transport, the surface exchange coefficient, and transport within the very stable boundary-layer are not as model sensitive as *ad hoc* corrections and would therefore be more robust with respect to any future major changes in the rest of the model.

Considering our emphasis on somewhat independent improvements of various aspects of the boundary-layer package, the overall package seems to be surprisingly compatible. However conclusive statements cannot be made. In fact, incompatibility problems are almost sure to arise as the total boundary-layer package is further studied within the Air Force Global Spectral Model under a variety of different meteorlogical conditions. Some possible problem areas might include the interaction between the snow physics and the boundary-layer model during long periods of strong surface radiative cooling, or, the interaction between the representation of boundary-layer cloud transport, surface evaporation and boundary-layer growth with a variety of cloud situations. The "real" improvement of the present developments within the global model must be further re-evaluated when more realistic respresentations of the global distribution of surface properties are adopted.

More specifically, the impact of the boundary layer on the global circulation must be studied in detail for different geographic regions and different synoptic situations. This extensive homework is necessary because the interaction between the boundary layer and the free atmosphere involves complex nonlinear coupling. As a result the impact of the boundary layer model is not always what it seems; the intuitive zero order effects are often exceeded by secondary effects not previously anticipated. The analysis of boundary layer-free flow interactions must also address the appropriateness of the soil and vegetation specification and the initialization of soil water. Considerable future effort will be devoted to four-dimensional data assimulation which includes updated soil moisture and temperature.

A major shortcoming of the present model is the absence of turbulent or subgrid scale transport above the boundary layer. In the real atmosphere, the turbulence is sometimes stronger above the boundary layer. This is particularly frequent in the case of the very stable nocturnal boundary layer where turbulence is sometimes maintained in the weakly stratified layer corresponding to the mixed layer of the previous daytime period. Other examples include the formation of clear air turbulence and strong turbulence in certain flows over complex terrain.

Therefore a formulation is required which allows for local shear-generation of turbulence and topographically induced transport of momentum and other quantities associated with nonlinear gravity waves. An important aspect of this problem is the effective Prandtl number of the formulated transport. Nonlinear gravity waves and turbulence in stratified flow usually lead to larger values of the momentum diffusivity as compared to the diffusivity for heat and other quantities. This difference is due to the generation of momentum transport by pressure effects. Obviously this problem is also important in the very stable boundary layer.

The boundary layer cloud formulation requires futher examination. This formulation plays a crucial role in the surface energy balance,

the overall boundary-layer development and the influence of the boundary layer on the general circulation. The problem is difficult because acceptably simple approaches necessarily emphasize either cumulus or stratus type boundary layer clouds, and the behavior of radiative and evaporative cooling at the cloud top occur on scales that cannot be resolved in the present model. Future work will concentrate on modification of the enhancement of the diffusivity due to shallow cloud convection. The present formulation overestimates transport as the total cloud cover (including inactive clouds) approaches 100 percent.

The most challenging stage of the future research will be evaluation of boundary layer-general circulation interactions with the improved shallow cloud formulation and the inclusion of free tropospheric transport by turbulence, gravity waves and other subgrid scale processes. This work must be carried out jointly with the Atmospheric Prediction Branch of the Air Force Geophysics Laboratory. We have recently been granted a new contract from AFGL to continue our research in these directions.

Other reports and articles prepared under this contract.

1. Interaction between soil hydrology and boundary-layer development (H.-L. Pan and L. Mahrt). *Bound.-Layer Meteorol.*, **38**, 185-202.

2. Grid-averaged surface fluxes (L. Mahrt). *Mon. Wea. Rev.*, **115**, 1550-1560.

3. An examination of structure and parameterization of turbulence in the stably-stratified atmospheric boundary layer (P. Ruscher). Doctoral dissertation, Department of Atmospheric Sciences, Oregon State University, Corvallis, Oregon, 97331, 170 pp.

4. Parameterization of shallow convection in the boundary layer (C.-T. Chu). Master of Science thesis, Department of Atmospheric Sciences, Oregon State University, Corvallis, Oregon, 97331, 83 pp.

Interaction Between Soil Hydrology and Boundary-Layer Development

H.-L. Pan

and

L. Mahrt

Department of Atmospheric Sciences

Oregon State University

Corvallis, OR 97331

U.S.A.

14 October 1986

ABSTRACT

A two-layer model of soil hydrology and thermodynamics is combined with a one-dimensional model of the planetary boundary layer to study various interactions between evolution of the boundary layer and soil moisture transport. Boundary layer moistening through surface evaporation reduces the potential and actual surface evaporation as well as the boundary-layer growth. With more advanced stages of soil drying, the restricted surface evaporation allows greater sensible heat flux which enhances boundary-layer growth and entrainment drying.

Special individual cases are studied where the wind speed is strong, solar radiation is reduced, transpiration is important, the soil is thin, or the soil is covered with organic debris.

Grid-Averaged Surface Fluxes

L. Mahrt

Department of Atmospheric Sciences
Oregon State University
Corvallis, OR 97331
U.S.A.

22 December 1986

ABSTRACT

This study examines the inadequacies of formulations for surface fluxes for use in numerical models of atmospheric flow. The difficulty is that numerical models imply spatial averaging over each grid area. Existing formulations are based on the relationship between local fluxes and local gradients and appear to poorly describe the relationship between the grid-averaged flux and the grid-averaged gradient. For example, area-averaging the bulk aerodynamic relationship reveals additional spatial correlation terms and a complex relationship between the grid-averaged exchange coefficient and the stability based on "model available" grid-averaged variables.

This problem is studied by assuming idealized spatial distributions of the Richardson number over a grid area. Some perspective is provided by consulting observed spatial distributions of the layer Richardson number at the surface. Various contributions to the area-averaged surface flux are studied by employing a small-scale numerical model as a grid box of a larger-scale numerical model. Based on these analyses, a new formulation is proposed for relating the area-averaged flux to the area-averaged gradient. However, this expression cannot be seriously tested with existing observations.

An Examination of Structure and Parameterization of Turbulence in the Stably-Stratified Atmospheric Boundary Layer

by

Paul H. Ruscher

A THESIS
submitted to
Oregon State University

in partial fulfillment of
the requirements for the
degree of

Doctor of Philosophy

Completed October 2, 1987
Commencement June 1988

ABSTRACT

The very stable boundary layer is a region of the atmosphere typified by large vertical gradients of temperature and momentum. Analysis of very stable atmospheric flows is complicated by the presence of nonlinear interactions among gravity waves, shear-driven overturning circulation, two-dimensional vortical modes and intermittent turbulence in various stages of development. This study examines the horizontal structure of a very stable atmospheric boundary layer, using data obtained primarily from terrain-following aircraft flights over central Oklahoma.

Several diagnostic procedures are applied to the aircraft data, including classical and rotary spectral analysis, principal component analysis, and structure functions. Coherent structures with sharp boundaries are examined with a new conditional sampling technique which requires little *a priori* specification of sampling criteria. Because the flows involve sharp boundaries, spectral techniques do not provide as much useful information as other more localized procedures. The edges of the coherent structures are regions of significant vertical heat transport, a feature not often emphasized in studies of gravity waves and vortical modes in the stable boundary layer.

The presence of significant turbulence even for large stability has implications for modelling of the very stable boundary layer. Forecasts of minimum temperature, boundary layer height, inversion characteristics, and pollutant dispersal are all significantly affected by turbulent mixing. Many models of the stable boundary layer artificially arrest the mixing under stable conditions, resulting in, for example, overestimates of nocturnal cooling. A new parameterization of the stable boundary layer is studied here by incorporating it into an existing model of the planetary boundary layer. The model is then run with one-dimensional sensitivity tests for an idealized atmosphere and with data from Wangara day 33. A simulation over snow cover is also examined. The tests substantiate the role of vertical mixing in ameliorating nocturnal cooling, validating the parameterization changes.

Parameterization of Shallow Convection in the Boundary Layer

by Cheng-Tsong Chu

A THESIS

submitted to

Oregon State University

in partial fulfillment of

the requirements for the

degree of

Master of Science

Completed 23 September 1986

Commencement June 1987

ABSTRACT

A shallow convection scheme is derived from several data sets (BOMEX, GATE, AMTEX, BLX83) AND DEVELOPED FOR THE OSU 1-D boundary layer model. Results of the model structure and characteristics of the saturation point (SP) profile are compared against the constant cloud diffusivity scheme of Tiedtke (1983) and the ECMWF boundary layer parameterization scheme.

The results indicate that the primary mechanism that transports moisture away from the lower boundary layer is the boundary layer turbulent flux and that the boundary turbulent mixing alone is capable of maintaining an apparent moisture source near the inversion. While the sensible heat flux over the ocean becomes quite small after a few hours of model simulation, the virtual heat flux remains positive and the boundary layer remains in the unstable regime.